

2005

Understanding and control of multifunctional graphitic foam properties

Gregory James Rosebrock
University of Dayton

Follow this and additional works at: https://ecommons.udayton.edu/graduate_theses

Recommended Citation

Rosebrock, Gregory James, "Understanding and control of multifunctional graphitic foam properties" (2005). *Graduate Theses and Dissertations*. 5259.
https://ecommons.udayton.edu/graduate_theses/5259

This Thesis is brought to you for free and open access by the Theses and Dissertations at eCommons. It has been accepted for inclusion in Graduate Theses and Dissertations by an authorized administrator of eCommons. For more information, please contact mschlangen1@udayton.edu, ecommons@udayton.edu.

UNDERSTANDING AND CONTROL OF MULTIFUNCTIONAL
GRAPHITIC FOAM PROPERTIES

Thesis

Submitted to

The School of Engineering of the
UNIVERSITY OF DAYTON

in Partial Fulfillment of the Requirements for

The Degree

Master of Science in Chemical Engineering

by

Gregory James Rosebrock

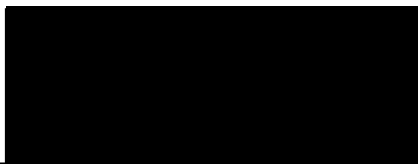
UNIVERSITY OF DAYTON

Dayton, Ohio

May, 2005

UNDERSTANDING AND CONTROL OF MULTIFUNCTIONAL GRAPHITIC FOAM PROPERTIES

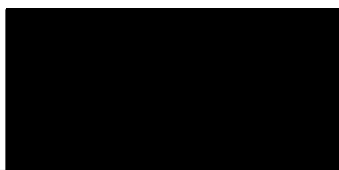
APPROVED BY:



Khalid Lafdi, D.Sc., Ph.D.
Research Advisor
Advisory Committee Chairman
Professor, Chemical and Materials
Engineering



Kevin Myers, D.Sc., P.E.
Academic Advisor
Committee Member
Professor, Chemical and Materials
Engineering



C. William Lee, Ph.D.
Committee Member
Professor, Chemical and Materials
Engineering



Donald L. Moon, Ph.D.
Associate Dean
Graduate Engineering Programs &
Research, School of Engineering



Joseph E. Saliba, Ph.D., P.E.
Dean, School of Engineering

Abstract

UNDERSTANDING AND CONTROL OF MULTIFUNCTIONAL GRAPHITIC FOAM PROPERTIES

Rosebrock, Gregory James
University of Dayton

Advisor: Dr. Khalid Lafdi

Properties of carbon foam are directly related to the foam's microstructure, the matrix material and its molecular orientation. Therefore, factors which alter any of these entities, factors such as bubble size, bubble size distribution, and additives to the pitch matrix, will have a distinct effect on carbon foam performance. Improvements in the ligament and node properties will lead to higher bulk foam performance.

During bubble growth, simultaneous mass, energy and momentum transfer occurs between the fluid melt and the surroundings. Controlling the bubble growth is one key to improving performance. This was studied in a numerical model, through varying initial bubble size, initial pressure and changes in viscosity. An increase of initial bubble radius or a decrease in melt viscosity causes an increase in both the bubble growth rate and movement. Furthermore, lowering the initial bubble pressure slows the growth and in turn reduces the bubble movement.

Once the microstructure was controlled, modifications on precursor material were implemented. This is accomplished by using specialized fractions of pitch, such as the beta fraction, or through the use of additives mixed in with the base mesophase pitch material prior to processing. The beta fraction inherently produces the desired zigzag structure, whereas the constituents alter the molecular structure of the host material by increasing this zigzag structure of the graphene planes in the foam's ligaments. This effect was seen to be cumulative as increased additives directly related to a higher presence of the zigzag structure and improved properties.

Additives are available in a variety of shapes and sizes which directly affect the strength and stiffness of the doped ligament and in turn, the carbon foam. All additives in this study affect the crystalline structure differently but generalizations were constructed. Decreasing the particulate size causes an increase in both strength and stiffness through a higher concentration of zigzag structure. It was also found that increasing the surface energy and decreasing surface impurities of the additive is beneficial to foam strength and stiffness. Therefore present and future studies of carbon foam should seek to simultaneously improve both the microstructure and the foam material itself.

Acknowledgements

My special thanks are in order to Dr. Khalid Lafdi, my advisor, for providing the time and means necessary for the work contained herein. His inspiration and constant challenges have allowed me to flourish and grow in my engineering endeavors. His vision and direction were an integral part to the completion of this work.

I would also like to thank Dr. Kevin Myers, for his guidance throughout my time at The University of Dayton and all those who have assisted me in my graduate work. This includes Dr. Ahmed Egalfy who offered guidance in numerical modeling and my friends and co-workers Tom Beechem and Bill Fox who have been working along side of me throughout. In addition, a special thanks is extended to Wright Patterson Air Force Base and MLBC for providing equipment and training. I would like to thank DAGSI (Dayton Area Graduate Studies Institute) for their financial support for my tuition as well as the Air Force Research Laboratory who assisted in funding my computer modeling under contract number F33615-D-00-5006.

Lastly, I would like to thank my family and friends for their love and support on this journey for higher education.

Table of Contents

Approval	ii
Abstract	iii
Acknowledgements	v
List of Figures	x
List of Tables	xiv
List of Symbols	xv
I Literature Review	1
1.0 Introduction	1
2.0 Processing of Pitch Based Carbon Foams.....	3
2.1 Precursor Material.....	3
2.1.1 Coal Derived Precursors	4
2.1.2 Petroleum Derived Precursors	5
2.1.3 Synthetic Based Precursors	6
2.2 Microstructure Development Methods.....	7
2.2.1 Thermodynamic Flash Processing	8
2.2.2 Non-thermodynamic Flash Processing	9
2.3 Post Foaming Heat Treatments	10
2.3.1 Stabilization.....	10
2.3.2 Carbonization.....	11
2.3.3 Graphitization.....	11
3.0 Numerical Simulation of Foaming Phenomena.....	12
3.1 Prediction of Microstructural Arrangement.....	12

2.2 Numerical Technique	45
2.2.1 Momentum Equation	46
2.2.2 Differential Mass Balance	47
2.2.3 Conservation of Mass at the Interface.....	47
2.3 Level Set Function	47
2.4 Discretized Equations	48
2.4.1 Level Set Functions.....	48
2.4.2 Mass Balance.....	48
2.4.3 Momentum Equation	49
2.5 Numerical Solution.....	49
3.0 Results.....	53
4.0 Parametric Study	58
4.1 Initial Bubble Pressure Effect.....	58
4.2 Initial Bubble Radius Effect	60
4.3 Viscous Effect	62
4.3.1 Viscosity Rate Effect	63
4.3.2 Initial Viscosity Effect	65
5.0 Conclusions	67
IV Fractionation of Mesophase Pitch.....	69
V Carbon Foam and Additive Properties	71
1.0 Microstructure of Carbon Foams.....	71
2.0 Carbon Fibers	81
3.0 HHT PS Nanofibers and Silver Coated Nanofibers.....	81
4.0 Single Wall Nanotubes.....	82
5.0 Carbon Black	83
VI Experimental Preparation and Mechanical Testing Procedure.....	84
1.0 Initial Processing and Foaming Procedure.....	84

2.0 Optical Testing Procedures.....	87
3.0 Mechanical Testing Procedures.....	88
3.1 Bulk Compression Tests	88
3.2 Ligament Tensile Tests	89
VII Results and Discussion	91
1.0 Areas of Study	91
2.0 Effect of Additive Size on Foam Properties.....	91
2.1 Size Effect on Bulk Compression Tests	92
2.2 Size Effect on Ligament Tests	96
3.0 Effect of Additive Shape on Foam Properties	98
3.1 Shape Effect on Bulk Compression Tests.....	99
3.2 Size Effect on Ligament Tests	99
4.0 Effect of Silver Coated Nanofibers on Foam Properties.....	101
5.0 Effect of Additive Weight Percent in Foam.....	109
6.0 Additional Ligament Analysis	109
7.0 Bubble Distribution of Doped Carbon Foam.....	113
VIII Conclusions	116
Bibliography	120

List of Figures

1-1	(a) Reticulated vs. (b) Pitch-based foams	4
1-2	Difference in molecular architecture of (a) synthetically derived pitch and (b) petroleum derived pitch	6
1-3	Graphitic Arrangement of Carbon Foam	24
3-1	Schematic of System	45
3-2	Diagram of nodal grid (overhead view)	50
3-3	Flowchart of numerical procedure inside the housing	51
3-4	Experimental viscosity profile used in simulation	53
3-5	Bubble growth and location using original processing conditions	54
3-6	Comparison of the current simulation to $t^{1/2}$	55
3-7	Change in bubble pressure using original processing conditions	56
3-8	(a) Reynolds, (b) Weber, and Peclet numbers during the process	57
3-9	(a) Radial growth and (b) bubble location with varying initial gas pressures	59
3-10	(a) Reynolds and (b) Weber numbers changing with time through differing initial bubble pressure	60
3-11	(a) Radial growth and (b) bubble location with time through differing initial bubble radius	61

3-12	(a) Reynolds and (b) Weber numbers changing with time through differing initial bubble radius	62
3-13	(a) Differing viscosity rate of change with time and (b) bubble growth through differing viscosity rate	63
3-14	Bubble location with differing viscosity rate	64
3-15	(a) Reynolds and (b) Weber numbers through differing viscosity rate	65
3-16	(a) Viscosity profiles and (b) bubble growth with differing initial viscosity	66
3-17	Bubble location with time through differing initial viscosity	66
3-18	(a) Reynolds and (b) Weber numbers through differing initial viscosity	67
4-1	Strength of beta fraction foams and carbon foams.....	70
5-1	Structural changes as function of heat-treatment temperature.....	72
5-2	Disclinations in carbonaceous mesophase. In this figure, the layers represent the general preferred orientation of the platelike molecules of the discotic nematic liquid crystal	73
5-3	(a) low magnification optical micrograph of stabilized carbon foam and (b) optical micrograph of stabilized carbon foam showing both ligament and node.....	74
5-4	Ligaments with disclination.....	74
5-5	Nodes with disclination.....	74
5-6	Bright field image of graphitized foam. TEM sample preparation was performed using an atomic milling technique.....	76
5-7	(a) and (b) 002 Dark field and bright field images of ligament relatively free of disclinations; (c) selected area diffraction of centered area of ligament free	77
5-8	High resolution image of areas on the ligament showing preferential orientation and $-\pi$ wedge disclination	78

5-9	(a) Cross section of pitch based carbon fibers. (b) High resolution imaging of areas of folding and ziga-zag textures (circled area in Fig. 9a)	80
6-1	(a) Mesophase pitch in powder form, (b) as a preform and (c) as a carbon foam with the similar masses	86
6-2	Typical processing of mesophase pitch	87
6-3	Instron and adjustable compression stage	89
6-4	(a) Computerized and (b) actual image of ligament tester	90
7-1	(a) Specific stiffness and (b) specific strength of foams with various size additives	93
7-2	Micrographs of (a) pitch, (b) milled and (c) HHT nanofiber foams	94
7-3	(a) Micrograph and (b) SEM of carbon foam containing carbon fibers	95
7-4	(a) Stiffness and (b) strength of ligaments with various size additives	97
7-5	SEM picture of a SWNT foam	97
7-6	The maximum (a) stiffnesses and (b) strengths of ligaments with various size additives	98
7-7	(a) Specific stiffness and (b) specific strength of foams with various shaped additives	99
7-8	(a) Stiffness and (b) strength of ligaments with various shaped additives	100
7-9	The maximum (a) stiffnesses and (b) strengths of ligaments with various shaped additives	101
7-10	(a) Specific stiffness and (b) specific strength	102
7-11	(a) Stiffness and (b) strength of ligaments	102
7-12	The maximum (a) stiffnesses and (b) strengths of ligaments with various additives	103

7-13	Specific stiffness and strength for silver coated HHT nanofibers	104
7-14	Bubble distribution in terms of size percents of various foams containing silver coated nanofibers	105
7-15	Carbon foam with (a) no additives, (b) 5% Silver nanofiber, (c) 10% silver nanofiber and (d) 20 % silver nanofiber	106
7-16	A magnified micrograph of a ligament containing silver coated nanofibers (single arrows on silver particles).....	107
7-17	SEM image of silver coated nanofiber foam.....	108
7-18	SEM image of a silver coated nanofiber foam displaying the zigzag structure	108
7-19	(a) Specific stiffness and (b) strength with weight percent additive.....	109
7-20	(a) Stiffness and (b) strength on ligaments relative to aspect ratio.....	110
7-21	Figure 7-20 broken down into individual additive types	111
7-22	Sequential images of ligament failure	112
7-23	Image of a brittle ligament failure	112
7-24	Skewness number with (a) temperature and (b) pressure	115

List of Tables

1-1	Comparison of Graphitic Crystal Structures	24
1-2	Comparison of thermal conductivity	29
1-3	Compressive properties of different carbon foams	31
1-4	Tensile Properties of different carbon foams	31
1-5	Proposed applications for carbon foams	37
3-1	Definitions of Parameters used	52
5-1	Properties of Nanofibers	82

List of Symbols

c	Dissolved gas concentration
c_i	Initial concentration
D	Diffusivity
g	Gravitational force
p	Pressure
\mathbf{g}	gravity vector
h	grid spacing
H	Step function
K_h	Henry's constant
Pe	Peclet number
R	Bubble radius
r	Radial coordinate
R_c	Critical bubble radius
Re	Reynolds number
t	Time
Δt	Time step
\mathbf{u}	Velocity vector
\mathbf{u}_{int}	Interfacial velocity vector
\mathbf{u}_{rel}	Relative velocity vector
U	Bubble rise velocity
V	Bubble volume
V_o	Bubble volume when satisfying mass conservation
We	Weber number
z	Vertical coordinate
κ	Interfacial curvature
μ	Viscosity
μ_i	Initial viscosity
ρ	Density
σ	Surface tension
τ	Artificial time
Φ	Level set function

Subscripts

l, v	Liquid, Vapor
--------	---------------

Chapter I

Literature Review

1.0 Introduction

Due to its many forms and wide range of physical characteristics, carbon is utilized in an innumerable amount of applications throughout the world. Running the gamut from structural material and absorbent material to thermal insulator or electrical conduit, carbon has found use in virtually every major industry [1]. This versatility of carbon, when coupled with the weight and surface advantages inherent in a cellular material, has made the study of a novel form of carbon, carbon foam, quite popular.

Carbon foams began to be investigated in earnest in the latter part of the 1960's with the innovation of vitreous carbon foams chiefly by the Union Carbide Company [2]. These foams, with their high thermal stability and low bulk density, were a material of high promise as insulators and construction materials for the aerospace industry in addition to being considered for biological application as internal prostheses [3, 4]. This new material was made by coating a rigid urethane foam with a furfuryl alcohol, and after initial room temperature curing; the system would be carbonized to create the glassy foam structure [2, 5]. This processing technique, however, proved to be both complex and time consuming and when coupled with the inability of these foams to be transformed into a

wholly graphitic form, innovation soon plateaued [6, 7].

Interest in carbon foams was soon revived, however, in the early 1990's due to the discovery that a carbon fiber precursor, mesophase pitch, could easily be transformed into a new kind of carbon foam capable of being nearly completely graphitized. This precursor, the main precursor in the making of many graphitic carbon fibers, has the unique ability to form highly aligned graphitic planes during processing, an aspect that aids both the strength and thermal properties of the subsequent product [1, 8, 9]. In conventional composites, this preferred alignment is exploited through the implementation of a network of graphite planes, the carbon fibers, connected by a matrix binder to form a material with attractive properties. This network results in a material whose characteristics are very attractive in the direction of the fibers but poor normal to these fibers. When foamed, this same alignment is achieved but in addition the graphitic network is now connected producing attractive properties in any direction [10, 11].

As a result of the connected graphitic network, pitch-based carbon foam has emerged as a material of great promise in a variety of applications. Rocket nozzles, advanced tooling, engine components, and as a core material in sandwich structures have all employed carbon foams due to its attractive thermal and mechanical properties [12, 13]. Furthermore, with a specific modulus rivaling that of a Kevlar honeycomb, carbon foam has even been suggested as a replacement for a vast array of materials ranging from balsa wood and polymer matrices to metallic honeycombs and titanium for use in biological applications

[13]. Due to this wide range of applications, research in pitch-based carbon foam has accelerated in the past fifteen years. Yet at the present time there has been no work summarizing the accomplishments thus far in carbon foam research. Consequently, this work aims to produce a review of the progress made by those studying carbon foams in an effort to clearly delineate the efforts completed thus far and the labor soon to be undertaken.

This work will focus only on pitch based carbon foams, hereafter referred to as graphitic carbon foams, since the vast majority of work being done in the subject is concentrated on this type of foam. The processing of these types of foam will first be examined, followed by a summary of the numerical modeling done in the subject. This work will then proffer a synthesis of all properties currently published in the literature followed by a listing of all applications which carbon foam has both been utilized in and suggested for.

2.0 Processing of Pitch Based Carbon Foams

2.1 Precursor Material

Glassy carbons are characterized by their "paracrystalline" structure which is much less ordered than that of graphite as indicated by their density differences of 2.66 g/cm^3 to 1.5 g/cm^3 , respectively [4]. Vitreous carbon foams adopt this glassy form as a result of minimal alignment occurring in the precursor resins during formation of the foam. Contrarily, in any mesophase pitch-based foam the precursor resin has the ability to become highly aligned during processing due to liquid crystal transformation [9, 14]. The degree to which this

alignment occurs will be the key constituent in determining pitch-based carbon foam's physical attributes [9]. Currently, coal, petroleum, and synthetic precursors dominate the manufacturing of carbon foams and as such their differences are delineated below. The differences in morphologies between reticulated and pitch based foams can clearly be seen in figure 1-1.

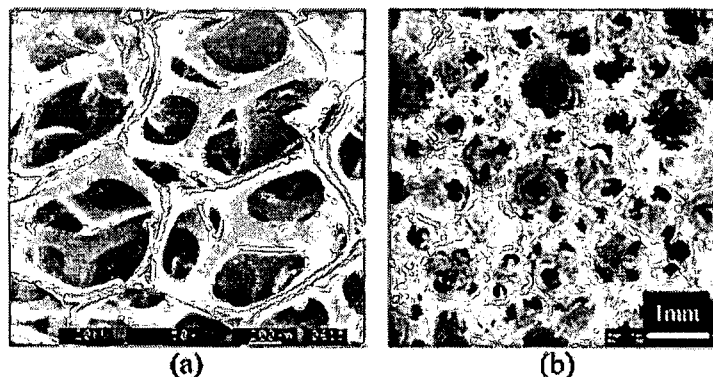


Figure 1-1 (a) Reticulated vs. (b) Pitch-based foams [15]

2.1.1 Coal Derived Precursors

Stiller, Stansberry, and Zondlo working from West Virginia University pioneered the use of coal as a precursor for carbon foams in the late 1990's. Taking a bituminous coal and transforming it into a mesophase pitch, the coal is first hydrogenated using tetralin, where it is then extracted in a manner to remove inorganic species through the use of tetrahydrofuran (THF). The hydrogenated coal is then de-ashed and extracted using a toluene mixture. The extracted species is an asphaltene or coal derived pitch precursor [16, 17, 18]. The resulting precursor has the ability to achieve high alignment of the liquid crystals resulting in a partly graphitizable carbon foam. Stiller et al. then assert that this technique allows for the tailoring of alignment by mixing the hydrogenated and

unhydrogenated coals before foaming. Using this technique yields of up to 50% have been reported [16, 17, 18, 19].

The level of graphitization produced using this type of precursor is not published to the best of the author's knowledge. It is stipulated that using this type of precursor will result in a carbon foam that can be used as a thermal conductor through its significant amount of graphitization, however, there are no papers published in which a coal precursor has been examined to quantify its graphitic crystal structure [17, 19]. Mechanically, foams being produced through use of a coal precursor have been reported to have specific strengths up to almost 95 MPa [13, 20].

2.1.2 Petroleum Derived Precursors

A petroleum residue is transformed into a mesophase pitch via catalytic modification, hydrogenation, thermal, or solvent modification [1]. Petroleum derived pitches are typically more "disc-like" than their rod-like synthetic counterparts [7] as can be seen in figure 1-2. This morphology along with factors such as aromaticity and molecular weight can significantly affect the viscosity of the pitch during foam processing and result in substantial changes in both the cell size and cell morphology of the subsequent foam [7, 21]. This effect is seen with reported cell sizes being as small as 50 microns using petroleum derived pitches, a size nearly $1/6^{\text{th}}$ of what is seen using synthetic pitches at identical processing conditions [22].

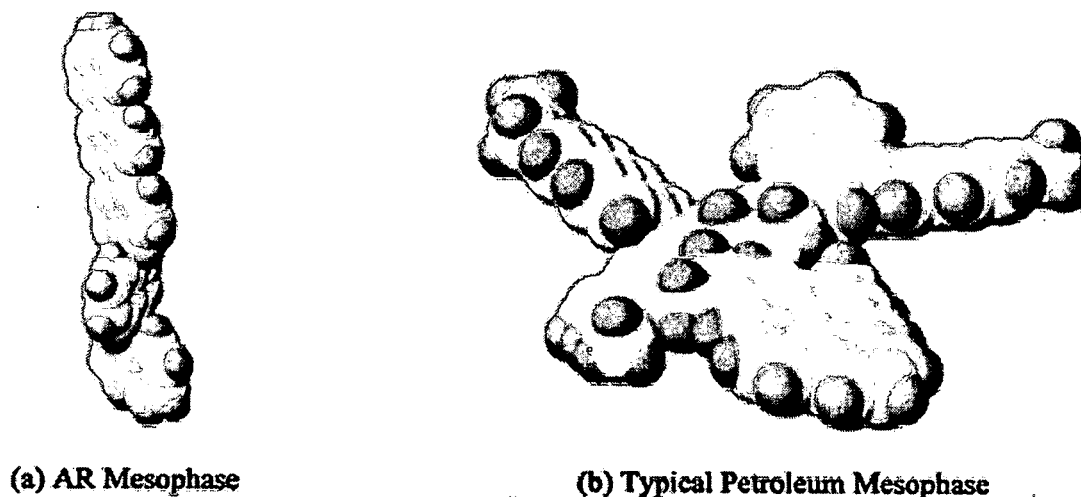


Figure 1-2 Difference in molecular architecture of (a) synthetically derived pitch and (b) petroleum derived pitch [7]

The disc-like nature of the precursor molecule, while affecting cell size, does not inhibit the foam from attaining a highly aligned graphitic state. Examination of petroleum derived foams has found that the degree of graphitization and size of graphitic crystals are comparable even to high thermal conductivity carbon fibers [7, 23]. Even with these large graphitic regions, reports on the thermal properties of petroleum-derived foams have indicated lower thermal conductivities than similarly processed synthetic pitches [7]. The reported 15% reduction in diffusivity is believed to be a result of the higher level of initial impurities in petroleum pitches which lead to lattice imperfections. However, this effect has only been theorized and has not been substantiated experimentally [7].

2.1.3 Synthetic Based Precursors

Using a catalytic modification technique, pitches can be produced synthetically, a process most successfully utilized by the Mitsubishi gas company

which produces over 1000 tons a year of synthetic mesophase pitch [1]. This synthetic pitch has a more rod like mesophase molecule which confers this type of pitch with its low viscosity and softening point [24]. Due to these attractive properties and the ability for these types of molecules to transform into large graphitic sheets, the vast majority of pitch-based carbon foam research from the early 1990's until the present day has utilized synthetic mesophase pitches [7, 8, 22, 23, 24, 25, 26, 27, 28, 29, 30, 31].

Synthetic pitches have proven to be the most versatile of the carbon foam precursors as they have been utilized in a host of different carbon foam processing techniques [28, 32]. In each case, they have been easily graphitizable, resulting in thermal conductivities of up to 476 W/mK [33, 34]. Secondly, mechanical properties of synthetic based precursors have been examined with specific strengths reaching up to 281 MPa [33]. It should be noted however that physical properties of foams are as dependent upon the processing as on the precursor.

2.2 Microstructure Development Methods

During foam processing the precursor is subjected to heat beyond its softening point. After softening, vapor is expelled from the melt through various methods. As this vapor coalesces into bubbles, the liquid surrounding the bubbles flows in a manner aligning the mesophase molecules in the ligaments separating the bubbles similar to that which occurs during melt spinning of carbon fibers [35, 36]. The manner and extent to which these bubbles grow determines the microstructure of the foam and to a large extent the thermal,

electrical, and mechanical properties of the subsequent foam. Two major bubble growth techniques have dominated research, thermodynamic flash and non-thermodynamic flash, and are elucidated below.

2.2.1 Thermodynamic Flash Processing

The thermodynamic flash technique is also known as the Wright Patterson technique, by the location of its first implementation. The making of a foam begins by first grinding a mesophase pitch into a powder of particle size ranging from 0.5 to 10 microns [28]. The powder is then pressed to an extent that voids are present while the powder is transformed into pellet form. The now pressed pellet is then placed into a pressure vessel where it is pressurized to about 500 psi by an inert gas, usually nitrogen, in order to fill the voids [28]. The pellet is then heated under this pressure to about 10 to 40°C above its softening temperature at which point pressure is often additionally applied to obtain a final pressure somewhere between 1000 to 1500 psi [28]. Above its softening temperature, the pitch flows to seal around the inert gas, at which point the pressure is rapidly released causing a thermodynamic flash in the system.

This thermodynamic flash causes the gas trapped by the pitch to rapidly expand forming bubbles and eventually, due to the bursting of these bubbles, the foam takes on an open cell orientation. This rapid growth causes the mesophase molecules to align along the ligaments separating these bubbles, a fact which gives foams their attractive properties. This growth is truncated as the viscosity increases quickly due to the decrease in temperature accompanied by the pressure release.

Variations on this process have been studied substantially. In 1999 Anderson et al. reported that through modifications in the final temperature and pressure in the reactor the density of final foam could be tailored to a specific application [26, 37, 38]. Similarly, it has been found that changes in the type of inert gas pressurizing the vessel will result in significant changes in foam microstructure [27]. Finally, viscosity is known to have a significant role in the formation and growth of bubbles in the system [24].

2.2.2 Non-Thermodynamic Flash Techniques

This technique, a natural derivative of reticulated foams, was first pioneered using a pitch precursor in the late 1990's by a group using a coal precursor [16]. In this process the precursor is heated until the coking stage whereupon volatiles evolve off of the pitch material and form bubbles thus determining the structure of the foam. Based on this type of method, a higher level of control and tailorability of the microstructure was then developed at Oak Ridge National Laboratory in the late 1990's.

The ORNL technique is at the leading edge of non-flash techniques and as a result its details are proffered here. First, a mold filled with pressed pitch granules are placed in a reactor which is evacuated to less than 1 torr [32]. The pitch is then heated to a temperature 50 to 100° C above the pitch's softening point where the vessel's evacuation is released to a nitrogen bath. The system is then pressurized to a level of 1000 psi while the temperature is raised to a point sufficient to coke the pitch [32]. At this point, the pressure and temperature of the system are reduced at a controlled rate to affect the evolution of the volatiles

off the system. This evolution of volatiles along with the rate of temperature and pressure decrease will determine the size and shape of the bubbles and hence determine the structure of the subsequent foam. Variations in the final temperature as well as pressure release have been reported to have a significant effect on the microstructures of the foam [15].

2.3 Post Foaming Heat Treatments

2.3.1 Stabilization

In the pressure flash technique, the initial foam, which has not been rid of its non-carbonaceous constituents, can be considered as a thermoplastic like material [1]. Consequently, if directly heated to a sufficiently high temperature to coke, the material will soften and lose its foamed structure. It is therefore necessary in the flash type of processed foam to perform a stabilization step before carbonization of the foam can occur. This stabilization, which effectively crosslinks the material with oxygen, occurs by heating the foam in an air or oxygen atmosphere for several hours at a temperature of around 200°C until the foam accrues a weight gain of between 5 and 8% [39].

Contrarily in non-flash techniques, there is no need for the stabilization step due to the simultaneous foam formation with coking [32]. Finally, it should also be noted that there have been no published studies regarding the effect which the extent of stabilization has on final foam properties.

2.3.2 Carbonization

Foams are carbonized in order to remove all heteroatoms from the system to achieve a carbon content of over 95%. A turbostratic like structure is formed during this step giving the material a significant increase in mechanical strength [1]. This is achieved by heating the foam to a temperature of about 1000°C where it is held for approximately an hour under in an inert atmosphere [32, 39]. Kearns stipulates that the heating rate must carefully be controlled to be within 1 to 3°C per minute. There is, however, no published works that compare final foam properties to the heating rate of the carbonization stage.

2.3.3 Graphitization

After being carbonized, the foams are then subsequently heated to a temperature between 2000 and 3000°C in order to completely graphitize the system. In this step, mechanical properties increase and the behavior of the material transforms from a thermal and electrical insulator to a conductor [1]. Specifically, foams are typically heated to a temperature between 2400 and 2800°C and held at this temperature for 1 to 10 minutes under an inert blanket [32, 39].

Klett reports that the heating rate during graphitization distinctly affects the crystal structure of the foam [40]. This is expected since the elimination of defects in the crystal structure is both time and temperature dependent. Properties are, therefore, optimized with a reduction in heating rate during the graphitization steps.

3.0 Numerical Simulation of Foaming Phenomena

3.1 Prediction of Microstructural Arrangement

Cellular material is composed of a series of struts connected together to form a three-dimensional truss structure [11]. The behavior of the foam when subjected to either thermal or mechanical loads is dependent upon the features of the truss architecture. Significant work has thus been undertaken in an effort to elucidate the features of carbon foam's truss structure and then relate this structure to processing variables. Accomplishing this task allows prediction of thermal or mechanical performance as they relate to processing conditions.

Significant progress was made in the late 1980's in the prediction of a cellular material's mechanical properties based upon an analysis of the truss geometry composing a unit cell. First among these notable studies was the work of Christensen who proposed that the structure of cellular material is composed of a random orientation of struts connected in a manner assuring isotropic behavior [41]. Warren and Kraynik differed with Christensen's random strut orientation by proffering a series of identical tetrahedral unit cells oriented randomly thus assuring isotropic behavior in their analysis [42]. Ashby and Gibson then used a simpler scheme by assuming a cubic arrangement of square struts with adjacent cells connected at their midpoints with similar results to Warren and Kraynik [43].

During the Material Research Society Symposium Proceedings of 1992, a group from Wright Patterson Air Force Base led by Joe Hager offered the first substantial effort at predicting the truss architecture of carbon foams [10, 44]. In

this body of work, the group first performed a micrographic examination using an SEM of carbon foams in order to delineate the preferred structure of the foams experimentally [44]. The study statistically confirmed and described the basic structure of carbon foams, a structure composed of trigonal ligaments meeting in groups of four at the junctions. Previous studies had either ignored the trigonal nature of the ligaments or placed the unit cells in a non space-filling manner rendering the predictions divergent from actual carbon foams.

As a consequence of these limitations in previous models, Hager reported a structure accounting for these two conditions while predicting a ligament structure based on processing parameters [11]. In this model, these conditions were met by assuming that bubbles nucleate on the lattice points of a body centered cube resulting in a unit cells composed of tetrakaidecahedron [11]. Tetrakaidecahedron is composed, however, of predominately four and six sided polygons. The parallel micrographic study indicated in contrast to this ascertainment that unit cells in carbon foams were composed chiefly of five sided polygons making a series of dodecahedrons [44]. The dodecahedral arrangement when stacked together in a manner to most efficiently take up space was then shown to closely mimic the structure measured micrographically [44]. A year later Hager and Anderson related this structure to highly idealized processing conditions [14]. This structure is currently still being employed, most recently being the starting point for a finite element analysis of carbon foams undertaken by Sihn and Roy in 2004 [45].

3.2 Prediction of Bubble Growth

In predicting the microstructural arrangement of carbon foams, several assumptions are made regarding the formation and growth of bubbles during processing. These studies presume a simultaneous commencement of growth at all bubble locations along with equivalent growth rates of all bubbles [11, 45]. Secondly, minimal correlations are made between the magnitudes of these growth rates with the conditions of processing. Consequently, these microstructural relationships offer only a tenuous relationship between processing conditions and the microstructure of the foams. As a result, several works have attempted to establish a stronger link between processing and microstructure formation by predicting bubble nucleation and growth through a simulation of the foaming process.

3.2.1 Nucleation Predictions

The extent to which bubbles nucleate during foam processing directly determines both the cell size and the cell size distribution in all foams [46]. Thus relating the extent of nucleation to processing conditions serves as a link between cell morphology and processing techniques. This link was first examined in a study performed by Colton and Suh in the late 1980's [47, 48]. In this work, a polymeric foam's nucleation rate and density were predicted theoretically and then verified experimentally. Colton and Suh assert that bubble nucleation density along with nucleation rate occur at its greatest value when both heterogeneous and homogenous nucleation occur simultaneously.

Using the developed model, a connection between processing and nucleation phenomena could be obtained. The work demonstrated the method in which nucleation varied with differing processing conditions. The maximum nucleation density and rate occurs when an additive is placed in a material close to its solubility limit and the material is saturated with high pressure gas [47, 48]. In 1992, Sandhu and Hager then used the relations of this model to predict the nucleation density of carbon foams during processing [8].

3.2.2 Growth Predictions

Regardless of the foaming method employed, in all phenomena bubble growth occurs as a result of exchanges in mass, momentum, and energy between the vapor and liquid phases. In order to predict growth, these exchanges must be accurately quantified in relation to the specific processing conditions. This prediction is tedious however as it links the coupled non-linear differential equations describing the transfer of momentum, mass, and energy from the liquid to the bubble. Consequently, there have been several different approaches employed to accurately predict bubble growth. It should be noted that due to their longer and more extensive use, polymeric foams have been the chief topic of these predictions. Yet the phenomenon is qualitatively the same regardless of material and as such the qualitative trends can be applied to carbon foams.

Plesset and Zwick [49], building on the original work in the subject of Rayleigh [50], offer the first substantial attempt for solving bubble growth in an infinite medium by employing an asymptotic solution to boiling phenomena. In

boiling phenomena, thermal energy effects are quite substantial. As such, the authors are able to solve the equation of motion only by directly computing the vapor pressure of the bubble from the temperature of the melt and then solving for growth. This temperature is only computable, however, by limiting the energy equation to the assumption of a thin thermal boundary layer bordering the bubble. Scriven [51] then took the solution a step further by including radial convection in his correlation of bubble pressure from liquid melt temperature but the solution still rested on the assumption of a thin thermal boundary layer. This connection of bubble pressure to system conditions serves as the critical assumption of bubble growth models. It has a great effect on the outcome and accuracy of the model and hence has continually been modified. Using this method, growth was accurately predicted at the earliest times and found to be proportional to the square root of time with errors becoming significant at longer times.

The correlation of bubble pressure to system conditions continued to be critical as growth studies evolved from non-viscous boiling phenomenon to growth studies incorporating growth in viscous media where temperature effects were no longer the only driving force. This type of phenomenon, the kind prevalent in processing of carbon foams, was first examined in the work of Barlow and Langlois [52]. They examined spherical bubble growth in an infinite medium of viscous liquid. Even with the differing conditions concerning the growth media, they used the assumptions employed previously concerning a thin boundary layer in their correlation of bubble pressure to the system. However, instead of using this layer to correlate temperature to pressure, the authors

employed a thin layer technique to link the concentration of the vapor phase to the pressure of the bubble via Henry's Law. This association then allowed for an analytical solution to the integro-differential equations of growth. Rosner and Epstein [53] then extended this technique by assuming that concentration of the vapor phase follows a specific polynomial profile in the boundary layer and that this polynomial accurately predicted growth. This technique proved to be quite popular and was applied by several researchers. Subsequently, changes in the polynomial allow different conditions of growth could be modeled [54, 55]. Again, however, due to the assumption of growth taking place in an infinite pool of liquid, melt growth was only accurately predicted at early times with errors growing significantly as simulation time lengthened.

Yet in each of these analytical solutions the major assumption of thin boundary layer serves as a crutch for prediction of growth. In this thin boundary layer, assumptions are needed to associate the bubble pressure to the conditions of growth and consequently the solutions are highly dependent upon these assumptions. These inferences create a mushy zone of calculation in the boundary layer which reduces the accuracy and usefulness of each one of the models.

Finite difference models attempt to alleviate the problem of the mushy zone through a numerical approach to growth. Street et al. [56] used the same boundary layer approach as Plesset and Zwick [49] but employed a finite difference solution instead of the analytical solution employed by the latter. This results in a solution that is only directly dependent upon the thin film assumption

at the point of interface between the surface and the melt rather than throughout the entire boundary layer as is the case in previous solutions. Arefmanesh et al. [57] then examined the use of the thin boundary layer approach and found that even in finite difference schemes the method still only produces accurate results at the earliest times of growth with disparities becoming more apparent as growth continues. These errors are irretrievable even with the use of higher order polynomials and consequently the authors proposed a method of solving the spherical growth of bubbles without this polynomial through the use of numerically solved potential functions.

Arefmanesh et al. [57] departed from this thin boundary layer technique and obtained very accurate results where growth was assumed to take place in only a finite volume of liquid. Thus, the polynomials are not needed in the solution, as defined by the thin liquid shell technique of Amon and Denson [58]. Venerus [59] then compared the two techniques of growth in finite and infinite extents of media to summarize and illustrate the advantages of each approach. Ye et al. [60] solved the problem of the boundary assumption by using a novel sharp interface method where all the pertinent information was calculated from a finite difference scheme thus giving the most accurate model to date.

In each of these models, it was shown that several different processing conditions directly affected the bubble growth and as such the microstructure of the foam. Parameters such as bubble pressure, solubility, surface tension, viscosity, and temperature all had distinct effects on bubble growth. Consequently, these studies have served to identify the factors determining the

formation of the microstructure in carbon foam. Yet in each of these studies, a material other than a carbon foam precursor was used to simulate growth. Therefore, only qualitative assumptions can be made with respect to the weight of individual parameters on the final structure of the foams. Work still must be done to directly simulate bubble growth in carbon foams and thus weigh the effect of each one of these processing parameters. This type of study was begun in 1992 by Sandhu and Hager who derived a mathematical model of a carbon foam process that accounted for both nucleation and growth without proposing a solution to the governing equations [8]. To the best of the author's knowledge no solution to these equations has yet been proffered to the research community, though recently, Beechem et al. modeled carbon foam growth processes asserting viscosity to be the major parameter determining both growth rate and bubble shape [61].

3.2.3 Predictions of Mechanical Behavior

In order to develop a processing property relationship, several studies have examined the ideal behavior of a cellular material under a mechanical load. These studies are accomplished by first defining a unit cell of the material as described in Section 3.2.1. Once defined, the unit cell is examined under load to determine how deformation occurs. The deformation is then related to the overall mechanical properties as well as to the cellular matrix material that makes up the trusses.

Lo performed one of the first types of these studies in the mid-sixties [62]. In this study, Lo relates the unit cell and hence the truss structure of the foam to

the packing characteristics of spheres. Then the author solves for the deformation using beam theory. The alignment of struts in the truss structure of the foam determines the manner in which the foam deforms. Lo asserts that a bending mode of deformation dominates when the struts are not aligned while stretching is chief mode of deformation when struts are aligned [62]. Equivalent modulus and Poisson ratio is then reported to be related to the void content in an inverse linear relationship. Christensen further supports this claim through a similar relationship obtained by assuming random strut orientation and allowing deformation to only occur axially [41].

Contrarily, in the work of Gibson and Ashby, deformation is believed to occur in a bending manner due to shear stresses [43]. Through these studies it was determined that foams do indeed deform according to a bending mechanism and that the effective Young's modulus is related to the porosity of the material squared. In Gibson and Ashby's work, however, the truss structure was assumed to be trigonal rather than the observed tetrahedral unit that was discussed in 3.2.1. This difference in truss structure was shown to be of diminutive importance as Warren and Kraynik came up with very similar relationships of effective modulus and Poisson ratio using a tetrahedral unit structure under realistic assumptions of microstructural arrangement [42, 63]. Recognizing this fact, Hall and Hager then asserted that the bulk modulus of the foam is insensitive to local cell geometry and related the bulk modulus to both the Young's modulus and the porosity of the carbon foam [36].

In all of these models, however, the struts were assumed to be uniform and isotropic. Yet under polarized light microscopy, it is obvious that these assumptions are not valid, as pitch derived carbon foams show variances across the ligaments. Sihn and Roy tackled these problems in a study performed in 2004 [45]. Using a tetrahedral unit cell similar to the one developed by Hager in 1992, Sihn and Roy varied the properties across the ligament and modeled deformation using a finite element analysis. Through this study it was reported again that bending dominates deformation mechanism and furthermore that effective modulus is most dependent upon the transverse properties of the struts. Consequently, processing schemes improving this property would most effectively improve carbon foam performance.

4.0 Carbon Foam Properties

4.1 Physical Properties

The physical properties of carbon foams are dependent on the precursor material as well as the processing of that precursor. It has been shown that the degree of porosity in a foam directly determines the physical properties of that foam [41, 42, 43, 45, 64]. Consequently, due to the porosity dependence of the foam, it is erroneous to simply compare the magnitudes of physical properties of two differently processed foams in order judge their effectiveness. Rather, to truly judge a precursor or processing technique, the properties of the separate foams must be compared on a unit weight or specific basis. Therefore, in the proceeding sections, the absolute property values are transformed to a specific

nature by using the listed density range in order to offer an accurate comparison of different foaming techniques and precursors.

4.2 X-ray Diffraction

Pitch based carbon foams are of extreme interest because of their ability to be transformed into a highly ordered graphitic structure. As stated previously, thermal and mechanical properties are highly dependent upon the degree of perfection in this graphitic lattice [1, 15]. Consequently, several studies have attempted to quantify the degree of graphitic perfection possible during the processing of carbon foams.

X-ray powder diffraction analysis is commonly used to probe the graphitic structure of the foam resulting in three key quantifiable properties. These three quantifiable parameters measure the degree of graphitic perfection by measuring the interlayer spacing (d_{002}), the stacking height (l_c), and finally the coherence length (l_a) of the basal planes in a foam. In pure crystalline form, graphite has been reported to have an interlayer spacing of 0.3354 nm [7, 15]. To optimize the properties of foam, ligaments should conform to this interlayer spacing while maximizing coherence and stacking height thus insuring a large crystalline graphitic region. In obtaining large crystalline regions, energy flow will be maximized and hence so too will the thermal conductivity and diffusivity [7, 15, 65].

The first comprehensive study on the graphitic arrangement of carbon foams occurred in 2000 in a work by Klett et al. where both synthetically and petroleum derived foams were examined after being processed using ORNL's

non-thermodynamic flash technique. Both petroleum and synthetically derived foams were reported to have interlayer separations similar to that of a crystal of graphite, 0.3360 and 0.3355 nm, respectively, values that were supported a year later in a thesis by Morgan and again in 2004 by Klett et al. [7, 15, 65]. Secondly, Klett reports that the spacing and density are inversely related although further experimentation is needed to verify this ascertainment [7]. These values were supported once again in 2003 when the interlayer spacing was reported to be 0.3363 nm using a synthetically derived foam processed using the flash technique [30]. The larger value in this case is not explained in the literature as flash technique foams have rarely been examined from an x-ray perspective. Nonetheless, in all of these studies, carbon foam's interlayer spacing has been reported to be similar to that of even the highest performance carbon fibers, a fact that can be seen in table 1-1.

Coherence length and stacking height have also been reported to be comparable to that of high performance fibers. This is seen as both synthetically and petroleum derived pitches using both flash and non-flash processing schemes have reported coherence lengths of up to 20 nm. Stacking heights have been reported to be as great as 80 nm and increase with density, a fact that is due to the ligaments thickening in denser foams [7, 30, 40]. This degree of crystallinity provides up to 98.8% graphitic structure which can be seen micrographically in figure 1-3. It is believed that the thermal performance of ligaments in carbon foams is equal or greater to that of even the highest performing carbon fibers [7, 66].

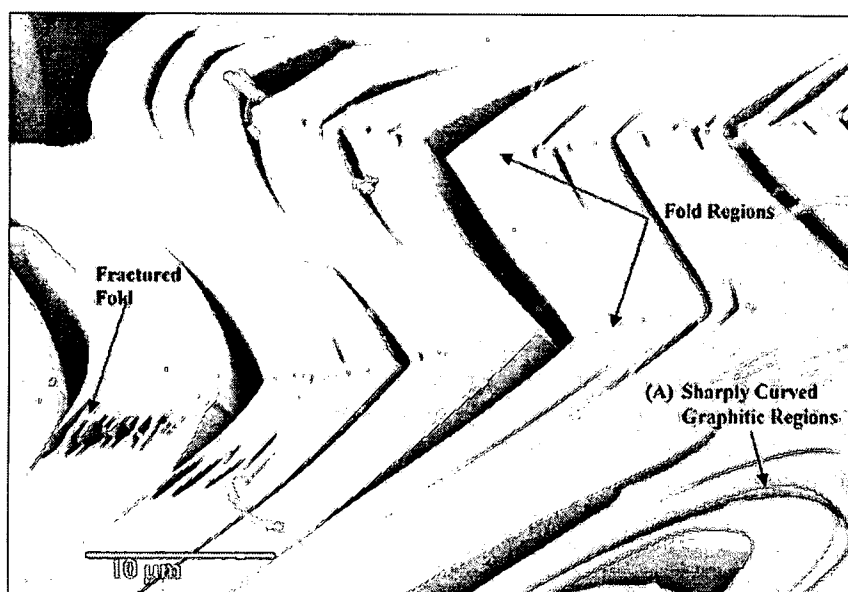


Figure 1-3 Graphitic arrangement of carbon foam [15]

Table 1-1 Comparison of graphitic crystal structures

Graphitic Foam	Type	Density (g/cm ³)	Interlayer Spacing d002 (nm)	Stacking Height Lc (nm)	Crystalline Size La (nm)	Sources
ORNL	Regular Processing		0.3358 - 0.3368	44.6 - 442	29	[7, 15, 23, 40, 66, 71]
Thermodynamic Flash	Regular Processing	0.14 - 0.25	0.3361		20	[15]
West Virginia	Regular Processing	0.048 - 0.8				[20]
Fibers	E35 (64)	2.2	0.3464	3.2	7.2	[15]
	E75 (64)	2.2	0.3421	10.7	22.4	[15]
	E120 (64)	2.2	0.3409	18.9	53.4	[15]
	E130 (64)	2.2	0.338	24	180	[15]
	K1100 fiber (49)	2.2	0.3366	51	85	[15]

4.3 Thermal Properties

A wide range of thermal property values have been reported for carbon foams due to a broad spectrum of precursor, processing, and heat treatment techniques. These differing techniques allow carbon foams to be utilized in applications ranging from thermally insulative to thermally conductive in nature [20]. Post foaming heat treatment greatly determines in what sense carbon foams will be utilized. Foams which are only processed through the carbonization heat treatment, hereafter referred to in this section as carbonized foams in contrast to just carbon foams, do not have high crystalline order and hence act as insulators. This fact when coupled with a large heat capacity of 0.718 J/gK makes carbonized foams ideal for many applications [65]. Yet there has been little study to the effect of processing conditions, precursors, and heat treatments on carbonized foams.

In contrast to their carbonized counterparts, foams develop high order during the graphitization heat treatment thus giving them a highly conductive structure suitable for many demanding applications [1]. The majority of studies in carbon foam have centered on this structure.

4.3.1 Graphitic Foams

During foam processing, liquid crystal regions of mesophase pitch become aligned due to the forces present during bubble expansion [14]. This alignment attained during processing allows for the formation of highly pristine graphitic crystal regions as reported in Section 4.2. No better arrangement of graphitic regions is found than in the ligaments of the foam where the most severe

alignment occurs during foaming. Consequently, the ligaments of graphitized foams have been reported to have thermal conductivities in the range of 700 to 1200 W/mK with just the ligament walls attaining a theoretical conductivity as high as 1500 W/mK [67, 73]. These values compare extremely well with metals, as copper's thermal conductivity is only 400 W/mK, however, improvement is still possible and needed as the theoretical conductivity of graphite is over 2000 W/mK at room temperature [15, 71]. It should be noted that thermal performance of graphite and hence foam can be reduced by up to 40% at high temperatures [64].

In contrast to the high alignment of ligaments in carbon foams, the junctions of the foams are composed of folded graphite layers which reduces the thermal conductivity in this region when compared against the foam's ligaments. [7, 15]. The lower conductivity in the junctions, a fact which is accepted although not quantified in literature, along with the cellular nature, results in the bulk foam's typical thermal conductivity being in the range of 150 W/mK as can be seen in table 1-2. This value is extremely attractive when examined on a unit weight basis, as the specific thermal conductivities of foams are 5 times that of aluminum and 6 times that of copper [7, 64, 67, 72, 73, 74]. Due to these high specific properties, several studies have been performed to further elucidate the heat transfer mechanisms in carbon foams in order that foaming precursors, processes, and heat treatments might be optimized.

4.3.1.1 Effect of Precursor on Thermal Conductivity

In thermodynamic flash as well as non-flash techniques, specific conductivities have been reported to reach up to $460 \text{ Wmm}^2/\text{gK}$ for synthetically derived foams, while in comparison petroleum derived pitches have been reported to reach only $240 \text{ Wmm}^2/\text{gK}$ [7, 22, 33, 34, 72]. Moreover, coal derived pitches have reported even lower specific conductivities in the range of 2.5 to $97 \text{ Wmm}^2/\text{gK}$ [13, 20, 75]. It should be noted however that under the same processing conditions petroleum derived precursors typically perform only 15% less than their synthetic counterparts, a fact that has been reported to be due to a higher impurity content in the petroleum derived pitches [7]. As a consequence of its attractive results and its easier availability, most studies have focused on synthetically derived pitches [7, 8, 22, 23, 24, 25, 26, 27, 28, 29, 30, 31].

4.3.1.2 Effect of Foaming Technique on Thermal Conductivity

There are three major foaming techniques which are described in Section 2.2. In each case, the method of foaming employed has a distinct effect on the thermal properties of the subsequent foam. In 2000 Oak Ridge National Laboratories reported over a 70% increase in thermal performance of their foams when their optimized pressure and temperature controlled method was used instead of a straight coking non-flash thermodynamic process [7]. However, the highest performing MER produced foams, a type of foam produced using a flash technique, have outperformed POCO foams, a non-flash foam, by nearly 30% [75].

To the best of the author's knowledge, there has been no reported explanation for this gross property divergence in differing foaming schemes although it has been reported that foaming rate has a distinct effect on final thermal properties [40]. It should be noted as well that while both types of processing schemes report to have foams that are completely isotropic, in 2004 Klett contrasted these assertions by reporting that in non-flash techniques the direction of foaming is three times more conductive than the other directions [33, 40, 72].

4.3.1.3 Effect of Post-Foaming Heat Treatment on Thermal Conductivity

The degree of ordering in the graphite planes during heat treatment is both time and temperature dependent. As time at high temperature is increased, so too is the amount of order in the foam. As a result, crystallite sizes grow and with their growth comes increased thermal conductivity. This effect has been clearly demonstrated as it has been reported that lowering the heating rate from 10°C/min to 4°C/min results in nearly a 25% increase in the thermal performance of the carbon foam [40].

4.3.2 Coefficient of Thermal Expansion

The coefficient of thermal expansion (CTE) is critical in applications where two dissimilar materials must be fixed to one another. Carbon foam has the attractive property of an extremely small CTE, 2 to 3 ppm/°C, whereas most other thermal management metals typically have a CTE between 17 and 23 ppm/°C [64, 66, 76]. This factor makes carbon foam extremely attractive for use

with silicon in electronics. No significant changes in the CTE have been reported due to changes in processing schemes or precursor material.

Table 1-2 Comparison of thermal conductivity

Graphitic Foam	Type	Density (g/cm ³)	Thermal Conductivity (W/mK)	Specific Thermal Conductivity (W/mK)/(g/cm ³)	Sources
ORNL	Isotropic	0.2 - 0.65	40 - 190	148 - 300	[7, 15, 22, 23, 66, 71, 74, 75]
	Anisotropic	0.45 - 0.61	z125 - 182 xy41 - 65	z277.8 - 331.1 xy91.1 - 106.6	[70]
Thermodynamic Flash	Regular Processing	0.016 - 0.62	0.05 - 210	0.63 - 476.2	[75, 95]
West Virginia	Regular Processing	0.16 - 0.5	0.4 - 17.5	2.5 - 97	[20, 75]
Fibers	E35 (64)	2.2	37	16.8	[70]
	E75 (64)	2.2	110	50.0	[70]
	E120 (64)	2.2	265	120.5	[70]
	E130 (64)	2.2	525	238.6	[70]
	K1100 fiber (49)	2.2	1100	500.0	[70]

4.4 Mechanical Properties

Mechanically, foams have predominantly been examined from a numeric standpoint as is delineated in Section 3.2.3. Chiefly through the work of Gibson and Ashby, along with the contributions of Sih and Roy, it has been clearly stated that carbon foam fails in a bending mode with the magnitude of its strength and modulus directly related to density [43, 45]. Experimentally little work has been done to understand the failure mechanisms in carbon foams. The

effect of precursor, processing, and heat treatment on the strengths of carbon foams can be seen in table 1-3. It should also be noted that the vast majority of studies have centered on compression properties of foams rather than tensile properties.

The work that has been done to address the mechanical properties of carbon foams has centered on methods to densify the foam in order to increase strength. Infiltration with a polymer or other structural material increases strength at the expense of added weight. In one study, carbon foam was infiltrated with polyurethane with a fourfold increase in specific compressive strength of the foam. The ability to use the polyurethane at a higher operating temperature due to the superb thermal conductive properties of the foams is also found attractive [68, 78].

Foam properties have also been reported to increase when densified using carbon through a chemical vapor infiltration. Using this method, the specific strength of the carbon foam after densification was shown to increase in a similar fashion as seen with the polyurethane infiltrated foam [23]. Strength is believed to increase due to the mending of cracks and layer separations which are present in the foam due to thermal stress effects of the foaming process [7, 64]. No study has been undertaken to discover the optimal amount of chemical vapor infiltration to maximize the specific properties of the foam.

Table 1-3 Compressive properties of different carbon foams

Graphitic Foam	Type	Density (g/cm ³)	Compressive Strength (MPa)	Specific Compressive Strength (MPa / (g/cm ³))
ORNL	Regular processing [49, 66, 75]	0.2 - 0.65	1-3.5	3.6 - 6.0
	Densification CVD [23]	0.77	31.6	17.7
	Infiltrate with Epoxy [23]	1.3	34.6	26.4
	Poco Foam [66]	0.55	3.0	5.5
Thermodynamic Flash	Regular processing [34, 76, 78]	0.016 - 0.62	0.08 - 25	1.56 - 59.52
	Infiltrate with Polyurethane [78]	1.14 - 1.21	39-41	33.9 - 34.2
	MER Foam [33]	0.016 - 0.62	1.7-7.0	up to 281
West Virginia	Regular processing [13, 20, 75]	0.048 - 0.8	1.4-41	12.5 - 95
	Touchstone Cfoam [13]	0.16 - 0.50	15.2-20.7	Up to 95

Table 1-4 Tensile properties of different carbon foams

Graphitic Foam	Density (g/cm ³)	Tensile Strength (MPa)	Specific Tensile Strength (MPa / (g/cm ³))
ORNL [66, 75]	0.2 - 0.65	0.7 - 1.6	2.8 - 2.46
Flash Technique [37]	0.12 - 0.8	0.863 - 65.3	7.2 - 81.6
MER [33]	0.016 - 0.62	0.5 - 0.7	2.0 - 2.06
Touchstone Cfoam [13]	0.16 - 0.5	1.14 - 7.0	5.0 - 14.0

5.0 Applications

5.1 Current Applications

Utilizing the advantages inherent in both cellular and carbonaceous materials, carbon foam is a material of great promise due to a litany of attractive properties. Among these attractive properties are the tailorability of its density and porosity in addition to its intrinsic high specific surface area [28, 32, 76, 81]. Furthermore, foams are attractive due to their ease of manufacturing into complex shapes [13, 29, 69, 76].

Moreover, the chemical nature of carbon lends carbon foams to a host of attractive properties: moisture insensitivity, low coefficient of thermal expansion, chemical inertness, high resistance to combustion, and thermal stability up to 3000°C in vacuum or 540°C in air, values which can be increased with oxidation protection [13, 20, 70, 78]. Due to these reasons carbon foam is currently being utilized in several different demanding applications.

5.1.1 Thermal Management Applications

With their high thermal conductivity as delineated in Section 4.3, carbon foams have been utilized in many thermally demanding environments, the most popular of which have been in the form of heat exchangers and heat sinks [71, 82, 83]. Capitalizing on the cellular nature of the foam, one such heat sink design has obviated the need for an active cooling system in electronics due to the system's effective heat transfer coefficient increasing over 40 times that of traditional materials [71, 84]. This same capability has been capitalized upon in a

separate project which has utilized carbon foam as the evaporator in a thermosyphon [85]. Yet in both cases the foam has allowed for a design that was drastically smaller than that which was made using traditional materials.

In more demanding environments an active cooling system has been used in conjunction with carbon foam with both promising thermal and weight saving results. In one such case, a graphitic foam heat sink with forced air flowing through it was used to cool a high performance Pentium 133 microprocessor. In this study the foam outperformed the standard aluminum material typically employed while weighing 5.5 times less. Furthermore, the foam design was modified to further decrease weight by machining off the fins with performance dropping slightly but with a weight decrease to 11 times less than that of aluminum while functioning well for over a year since implementation [76]. Finally, active systems with foam and water as the cooling agent have been able to cool chips at power densities of up to 120 W/cm^2 although a significant pressure difference occurs when circulating the water through the foam [76, 86].

5.1.2 Structural Applications

A specific modulus rivaling that of a Kevlar honeycomb along with its attractive thermal characteristics [13] have allowed carbon foam to be suggested for a variety of structural applications. Sandwich structures are composed of a thermally resistant material coupled with a structural material. Typically the thermally resistant material has little structural value, however, this is not the case with carbon foam which has mechanical attributes and as such has found use in this venue with beneficial results [87]. This structural value is seen more

clearly as carbon foam has been attached to panels and has been used with successful results as a replacement for many metallic honeycombs [7, 66, 87]. Finally, when a fully graphitized foam is placed in between panels a variety of applications have been shown to be completely plausible ranging from heat pipes to radiators in automobiles, saving weight and increasing performance in each case [77, 87, 88].

5.1.3 Internal Combustion Engines

Weight, durability, and creep resistance are the critical design parameters for the pistons of internal combustion engines. Aluminum has long been used as it whisks away the heat of the engine chamber, yet these metallic pistons are heavy thus reducing the efficiency of the engine. Consequently, many designs have sought to decrease the weight by combining an aluminum foam with a polymer of high temperature resistance. This has proven problematic, however, as the low thermal conductivity of the piston has led to premature thermal degradation of the engine. Contrarily, using a thermally conductive carbon foam filled with aluminum has solved both problems with a 40% weight reduction providing an engine with higher efficiency and power output [23, 34].

5.1.4 Supercapacitors

High pulse power delivery is needed for many processes in the electronics industry, yet with traditional materials battery sizes must increase substantially with this increased performance. Supercapacitors, however, can produce these high pulses resulting in a package which is smaller in size with the advantages of

extended battery life and non-degrading stable charge and discharge cycles. Currently, Cooper Electronic Technologies is constructing supercapacitors from carbon foam calling their product the PowerStor Areogel capacitor. This capacitor uses an electrochemical double layer arrangement which utilizes carbon foam electrodes with ultrafine pore size in an electrolyte fill environment. The maximum operating voltage is 2.75 volts with a 5.5 volt version currently being developed [89].

5.1.5 Solid State Reactor

Small nuclear reactors have been proposed as the ideal power source for energy generation in the most remote of environments. In a project funded by the DOE's Demand-Driven Nuclear Energizer Module Project, a solid-state nuclear reactor was designed and fabricated with carbon foam as an integral component. Utilizing the strength, heat conduction, and high operating temperature much of the core was composed of carbon foam with promising results [90].

5.2 Proposed Applications

Due to its attractive properties carbon foam has been suggested for a myriad of different applications. In this section, many of these proposed applications that are looming on the horizon will be proffered in order to expose where the next generation of carbon foams will be utilized.

Due to its high specific properties, carbon foam is ideal for utilization in the field of aeronautics where all designs are constrained by volume and weight considerations. Consequently, carbonized foam has been suggested for use in

leading edges of high performance aircraft, rocket nozzles, and as aircraft brakes [13, 79, 81].

Structurally, due to its isotropic properties, carbon foam has been suggested as a replacement for metallic honeycombs and as a core material for interior panels, sandwich structures, non structural bulkheads, sound absorption panels, as well as a shield for electromagnetic radiation [15, 20, 67, 78, 81, 91, 92, 93, 94]. Using foam as a core material has even been suggested for the support of spaceborne mirrors due to a variety of reasons including its ability to cushion large amounts of kinetic energy [20, 78, 95].

Similarly, from a thermal absorption standpoint, carbon foam infiltrated with a phase change material is believed to find application in the space program in the near future [96]. Additional proposed applications can be found in the following table, table 1-5.

Table 1-5 Proposed applications for carbon foam

Aerospace & Defense	Commercial		
Optical benches and lightweight mirrors ^[13]	Composite tooling ^[13,55]	Heat exchangers ^[13,80,91]	Truck brake ^[80,91]
Thruster nozzles ^[13,66]	Abrasive tools ^[13,55]	High temp tooling ^[80,91]	High speed train brake ^[80,102]
Thermal protection systems ^[13]	Battery & fuel cell electrodes ^[13,55,80]	Acoustic Insulation ^[80,91]	Piston ^[80,104]
Heat transfer systems ^[13]	Brake disks ^[13]	Acoustic & thermal panel ⁸⁰	High temperature insulation ^[13]
Light weight antennas ^[13]	Automobile crush zone capsules ^[13]	Engine components ^[13,80]	Multi-layer PWBS ^[80]
Joiner bulkheads ^[13]	Fuel cell anode/cathode gas diffusion & catalyst support ^[87]	Ballistic ^[80] containment cases	Multi-chip modules ^[80]
Jet blast deflectors ^[13,66]	Catalytic converters ^[13]	Electronic heat sinks ^[80]	Chip carriers and chip on board ^[80]
Stealthy materials ^[13,66]	Core attachment ^[80]	Friction/brake ^[80]	Recreational equipment like canoes ^[80]
Lightweight armor ^[13,66]	Energy absorbing crash barriers ^[13]	EMI shielding ^[80]	Brakes ^[78]
Ship bulkheads ^[66]	Structural insulated panels ^[13]	Leadings edges ^[80]	Clutches ^[78]

Chapter II

Work Statement

Carbon foam has come to the forefront of desirable new age materials because of its ultra lightweight coupled with its exceptional properties. Due to the nature of this material and its complexities, heavy research has been performed in an attempt to link foam processing and carbon foam properties. This material shows much promise but the complexities inherently involved with simultaneous energy, mass and momentum transfer during processing have ultimately reduced the foams performance. This relationship needs further investigation to bridge the gap between the current and theoretically capable properties of carbon foam, thus this study acts as one such link.

Improving carbon foam properties is attained by improving the foams microstructure along with improving the matrix material itself. The microstructure of carbon foam consists of interconnecting ligaments and nodes created from the expansion of multiple gas bubbles. Thus, the first step in adding to the understanding of carbon foams is through modeling the bubble growth and movement phenomena where idealized conditions can be simulated. Through a numerical model, the simultaneous transfer of energy, mass and momentum between the molten fluid and the surrounding is constructed giving insight to the foam microstructure. Using a parametric study then allows various foaming

conditions to be easily analyzed. This deeper understanding provides logical processing parameters to be used in experimental runs where resulting foams then can be characterized by evaluating the foams structure and composition. This is preformed through micrographs and an analysis on bubble size and bubble distribution, consequently linking the microstructure to the foam performance.

Though the microstructure is important, the material used in foam processing also has a drastic effect of the final properties. Most of the current research involves exploiting the exceptional thermal properties of carbon foam, concurrently neglecting the mechanical properties. This work aims to qualitatively examine the carbon foam mechanical properties while quantifying the effect of additives on foam performance. This will be attained through both bulk and localized mechanical analysis of the carbon foams.

These various points of view bestow an all inclusive picture of carbon foam, linking modeling, processing and foam performance. This insight is crucial in the development and pursuit of improved foam properties.

Chapter III

Numerical Study of the Growth and Motion of Graphitic Foam Bubbles

1.0 Introduction

Incorporating the advantages inherent in both cellular and carbonaceous materials, carbon foam is a material of great promise due to its attractive specific properties. With a specific modulus rivaling that of a Kevlar honeycomb and a specific conductivity over five times that of copper, the material has naturally been suggested for an eclectic variety of applications [7, 36, 73, 97]. Such applications include heat sinks for electronic chips, heat exchangers, heat pipes and radiators in motor vehicles [76] as well as sandwich structures, aircraft brakes, rocket nozzles and leading edges of aircrafts [79].

The thermodynamic flash processing of carbon foam starts with a solid preform of pressed mesophase pitch [11, 14, 28, 30, 36, 44, 97, 98, 99]. Then, the preform is placed into a reactor under high pressure and temperature causing the pitch to transform into a viscoelastic fluid. With this transformation, the gas in the reactor diffuses into and saturates the pitch whereupon with the release of pressure, the dissolved gas expands into bubbles creating the carbon foam [28]. The subsequent microstructure determines the thermal, mechanical, and electrical properties. Thus, tailoring of the foam is dependent on the ability of

controlling the vapor phase bubble growth, a feat possible only with a thorough understanding of the forces at work during the foam formation.

Due to this importance, there has been extensive work on the modeling of bubble growth in liquids [49, 52, 53, 99, 100, 101]. Modeling this phenomenon is imperative as it links the equations describing the transfer of momentum, mass, and energy from the liquid to the bubble. Pioneering work in this field was performed by Barlow and Langlois [52] who modeled spherical bubble growth in an infinite extent of liquid. In their model, the transfer of mass and momentum is solved by assuming that concentration gradients are only present in a thin boundary layer of liquid close to the bubbles surface. With this assumption, Barlow and Langlois [52] then used Laplace transformations to obtain an analytical solution to the problem of bubble growth as a function of time.

A similar boundary layer approach has been used by several researchers solving thermally controlled growth and diffusion-controlled growth [49, 53, 100, 101]. The approach assumes that the concentration gradient follows a polynomial profile throughout the boundary layer simplifying the diffusion equation and allowing for easier manipulation for numerical solutions. The results of these models differ from experimental data due to a microconvection phenomenon known as Marangoni convection [101]. Furthermore, the extent of accuracy of these models is unclear, however, as in each model, the magnitude of the initial perturbation that is used to initiate growth out of metastable equilibrium greatly affects the results. Shafi et al. [99] circumvents this problem

through the use of nucleation theory in conjunction with a perturbation solution to solve bubble growth.

As it is clear from previous literature, the bubble growth phenomenon plays an important role during carbon foam processing. Yet, this growth will not occur at a fixed position in the bulk liquid. During the expansion process, and due to buoyancy forces, the bubble will not expand in a fixed position, but instead it will experience a movement simultaneously with the growth. Perhaps this movement is very slight, but we can not consider the growth without considering the movement to reach a comprehensive model for carbon foam processing.

Liger-Belair et al. [102] studied the growth and movement of bubbles from a pressure release of a closed chamber with super saturated fluid by modeling the phenomenon in champagne bottles. This similar bubble growth and movement that occurs upon the opening of carbonated fluids demonstrates a phenomenon that lends insight to foam bubble growth as well as bubble movement. In such a model, the fluid is assumed Newtonian and the bubbles propagate at nucleation sites along the surface of the bottle instead of throughout the core of the fluid as found in foams. Yet, even with these differences the methodology of a parallel solution to growth and movement is portrayed.

The work of Snabre et al. [103] mitigates these differences by shedding light on how to handle bubble movement in a viscous fluid from a continuous source of vapor. This analysis predicts both growth and movement through the entirety of the bubble's presence as well as examining interaction effects in the stream of bubbles in a viscous liquid. From the analysis at high fluid viscosity,

the inertial and surface tension forces can be neglected and the bubble's movement results solely from the drag and buoyancy forces. Further on, at high pressure conditions the gas momentum force has a large effect on the bubble formation [101], nevertheless this method too has its limitations.

Though these models are useful, there are often issues involving occurrences at a bubbles interface. An accepted approach to tackle such a problem as well as incorporating bubble growth and movement is presented by Sussman et al. [104] in a solution referred to as level set method. The level set approach was developed to prevent instabilities in numerical calculations due to steep gradients at a bubbles surface but in some instances the conservation of mass is not satisfied. As a bubble moves and grows, the discretization in numerical solution continued to reduce the size and the mass of the bubble, however in a following paper, Sussman et al. [105] implemented an improvement for better mass conservation by the use of an iterative process.

Later, Son [106] applied this level set method for the computation of growing bubbles and their movement in a stationary fluid due to the phase change phenomenon. The simulation allows deformation to occur when considering multiple bubbles. Therefore, this provides a suitable solution for the merging and breaking of bubbles. With this interfacial procedure, the conservation of mass is maintained and the solution compares well to reported data and analytical calculations.

Building on these perspectives, a model combining bubble growth and movement during the processing of carbon foam is presented. Son's work [106]

applied concepts suitable for bubble growth and motion due to phase change, however, for the carbon foaming process the mechanism is slightly different, though the concepts are similar, as foam's growth is diffusional rather than phase change dominated. In making the necessary modifications, the current simulation predicts the size and location of a single spherical bubble throughout the entire time of carbon foam formation through the use of the level set method.

2.0 Mathematical Definition

In the present work, a numerical simulation, which is based on the level set method [104, 106], is introduced for spherical bubble growth and movement in that these are major contributors to carbon foam processing. Sussman et al.'s [104] level set approach with manipulations to Son's work [106] allows for an inclusive simulation of bubble growth and movement during carbon foam processing. The influences of surface tension, viscosity, pressure and diffusion through the system are monitored and related through simultaneous transfer of energy and mass between the liquid and vapor regions. Consequently, in order to predict growth and motion these terms must be quantified at each instant. This study quantifies the energy through the solution of several simultaneous non-linear differential equations, which are described below.

2.1 Assumptions

Figure 3-1 illustrates the physical domain of the problem and the model is further explained under the following assumptions. The bubble begins as a spherical nucleus and continues to grow as a sphere in the Newtonian

incompressible fluid. The fluid is assumed to be infinite and the system is isothermal in nature.

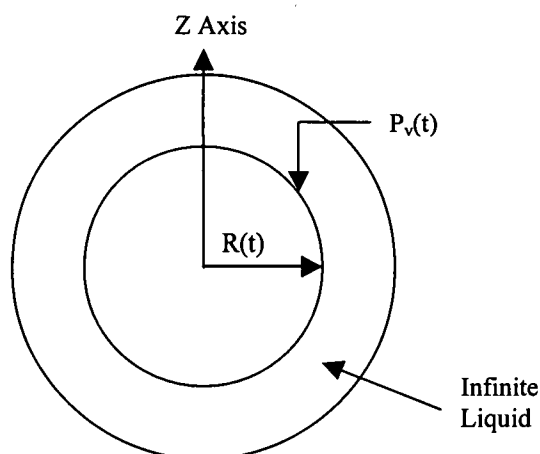


Figure 3-1 Schematic of system

A description of the validity of such an assumption is described exceptionally by Beechem et al. [61]. Thus the results are qualitative rather than quantitative in nature [57]. Across the time of growth, the bubble moves in the z direction. The gas within the bubble is assumed to follow the ideal gas law with the pressure and concentration at the bubble interface being related by Henry's Law.

In conjunction with these assumptions, the simulation begins with the release of pressure which is the onset of growth. This pressure release initiates the growth by alleviating the thermodynamic equilibrium that is previously present inside.

2.2 Numerical Technique

For the growth and movement of the bubble, a level set method [104] is implemented. It involves a level set function Φ which is defined as the interface

between the liquid and vapor. This type of mushy interface prevents numerical instabilities that can occur from steep gradients by smoothing over several grid points, h , as derived by Son [106]. A step function, H , is used in calculating the changes that occur at the interface for properties such as density and viscosity [104, 106]. The relations between h and H are as follows:

$$\begin{aligned} H &= 1 & \text{if } \phi \geq 1.5h \\ H &= 0 & \text{if } \phi \leq -1.5h \\ H &= 0.5 + \phi/(3h) + \sin[2\pi\phi/(3h)]/(2\pi) & \text{if } |\phi| \leq 1.5h \end{aligned} \quad (1)$$

Density is calculated using arithmetic interpolation where as viscosity is considered using harmonic interpolation as suggested by Patankar [107]. The symbols ρ and μ designate the density and viscosity with the subscripts l and v representing the liquid and vapor phases with.

$$\rho = \rho_v + (\rho_l - \rho_v)H \quad (2)$$

$$\frac{1}{\mu} = \frac{1}{\mu_v} + \left(\frac{1}{\mu_l} - \frac{1}{\mu_v}\right)H \quad (3)$$

2.2.1 Momentum Equation

$$\rho \frac{d\mathbf{u}}{dt} = -\nabla \mathbf{p} - \sigma \kappa \nabla H + \rho \mathbf{g} + \nabla \cdot \mu \nabla \mathbf{u} \quad (4)$$

With

$$\frac{d}{dt} = \frac{\partial}{\partial t} + \mathbf{u} \cdot \nabla \quad (5)$$

Where \mathbf{u} is the velocity vector, \mathbf{p} is the pressure, κ is the bubble curvature, \mathbf{g} is gravity, t is time and σ is the surface tension [106].

2.2.2 Differential Mass Balance

$$\frac{\partial \mathbf{c}}{\partial t} + \mathbf{u} \cdot \nabla \mathbf{c} = \nabla \cdot D \nabla \mathbf{c} \quad (6)$$

Where \mathbf{c} is concentration of dissolved gas and D is diffusivity [99, 100, 108].

2.2.3 Conservation of Mass at the Interface

$$\nabla \cdot \mathbf{u} = \frac{1}{\rho} D \nabla \mathbf{c} \cdot \nabla \rho \quad (7)$$

Along with these, the interfacial velocity term is of major importance because it determines the bubble growth. It is based on Son's [106] equation of interfacial velocity, \mathbf{u}_{int} is defined as

$$\mathbf{u}_{\text{int}} = \mathbf{u} + \frac{1}{\rho} D \nabla \mathbf{c} \quad (8)$$

2.3 Level Set Function

The level set function Φ as stated earlier is used at the interface, with positive values of Φ designated for the liquid side and negative values for the gas side. At the bubble's interface the Φ value is given a zero value, moving with the interface as it grows. Thus after every step, the Φ values are used in determining the next interfacial location in addition to being shifted there. The thickness of the interface must also be maintained throughout the solution, thus $|\nabla \phi| = 1$ must be reinitialized after every step as described by Sussman et al. [104, 106]. This step involves using an artificial time, $\Delta \tau$, a value which is set to $h/2$ [106].

Calculating the Φ values is a three step iterative approach as mentioned earlier. This allows for the various Φ calculations as well as providing for the conservation of mass. The final form of the equations can be seen in the discretized section.

2.4 Discretized Equations

The following equations are used for the numerical solution and are shown in discretized form. The first three equations deal with the level set method and the conservation of mass [106]. Those are followed by the mass balance and momentum equations.

2.4.1 Level Set Functions

$$\frac{\phi_o - \phi^n}{\Delta t} + (\mathbf{u}_{\text{int}}^n + U\mathbf{g}/g) \cdot \nabla \phi^n = 0 \quad (9)$$

with

$$\mathbf{u}_{\text{int}} = \mathbf{u} + \frac{1}{\rho} D \nabla c \quad (10)$$

$$\frac{\phi^* - \phi_o}{\Delta \tau} = \frac{\phi_o}{\sqrt{\phi_o^2 + h^2}} (1 - |\nabla \phi^*|) \quad (11)$$

$$\frac{\phi^{n+1} - \phi^*}{\Delta \tau} = (V - V_o) |\nabla \phi^{n+1}| \quad (12)$$

Where U is bubble rise velocity, V is bubble volume, and V_o is bubble volume that satisfies conservation of mass.

2.4.2 Mass Balance

$$\frac{c^{n+1} - c^n}{\Delta t} + \mathbf{u} \cdot \nabla c = \nabla \cdot D \nabla c \quad (13)$$

2.4.3 Momentum Equation

$$\rho \left(\frac{\mathbf{u}^* - \mathbf{u}^n}{\Delta t} + \mathbf{u}_{rel}^n \cdot \nabla \mathbf{u}^n \right) = -\nabla p^n - \sigma \kappa \nabla H + \rho \mathbf{g} + \nabla \cdot \mu \nabla \mathbf{u}^* \quad (14)$$

$$\mathbf{u}^{n+1} = \mathbf{u}^* - \Delta t (p^{n+1} - p^n) / \rho \quad (15)$$

with

$$\kappa = \nabla \cdot \frac{\nabla \phi}{|\nabla \phi|} \quad (16)$$

$$\mathbf{u}_{rel} = \mathbf{u} + U \mathbf{g} / g \quad (17)$$

To account for the pressure term in the momentum equation, the following is used as the governing pressure equation. This is made consistent with Henry's law, with K_h being Henry's constant, since the bubble pressure is related to the dissolved gas concentration at the bubble's surface [99, 108].

$$\nabla \cdot \frac{1}{\rho} \nabla p^{n+1} = \nabla \cdot \frac{1}{\rho} \nabla p^n + \frac{1}{\Delta t} \nabla \cdot \mathbf{u}^* - \frac{1}{\Delta t} \frac{1}{\rho} D \nabla c^{n+1} \quad (18)$$

$$c(R, t) = K_h \cdot p_v(t) \quad (19)$$

The velocity term is then calculated using equation (20).

$$\nabla \cdot \mathbf{u}^{n+1} = \frac{1}{\rho} D \nabla c^{n+1} \cdot \nabla \rho \quad (20)$$

2.5 Numerical Solution

A level set approach is used in the determination of the bubble growth and movement. The growth program uses a standard numerical methods technique involving nodes on a pre-set polar grid [107]. For symmetrical considerations, a quarter of the bubble's diameter is considered as in figure 3-2.

For the bubble motion, the z - r plane, figure 3-1, is considered to allow for movement in the vertical direction.

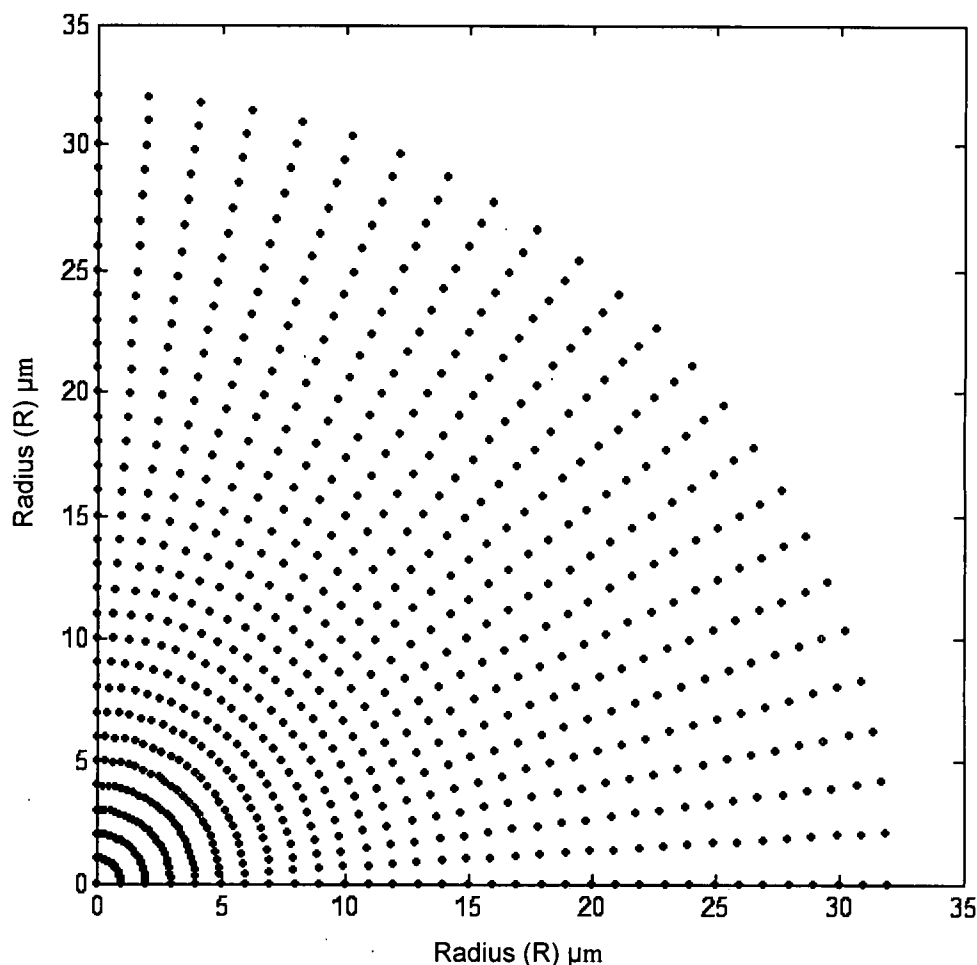


Figure 3-2 Diagram of nodal grid (overhead view)

Growth takes place in the radial direction of the spherical bubble with the center of the growing bubble monitored and used for the movement portion of the solution. The location of the bubble at time t is described as the center of the bubble along the z -axis. Bubble movement is predicted throughout the processing time in conjunction with the viscosity range. Across this range, there is a point at which a significant increase in viscosity occurs, typically around 0.2

seconds after the pressure release. The procedure for solving both growth and movement in a parallel fashion is delineated in figure 3-3 with the initial conditions listed in table 3-1.

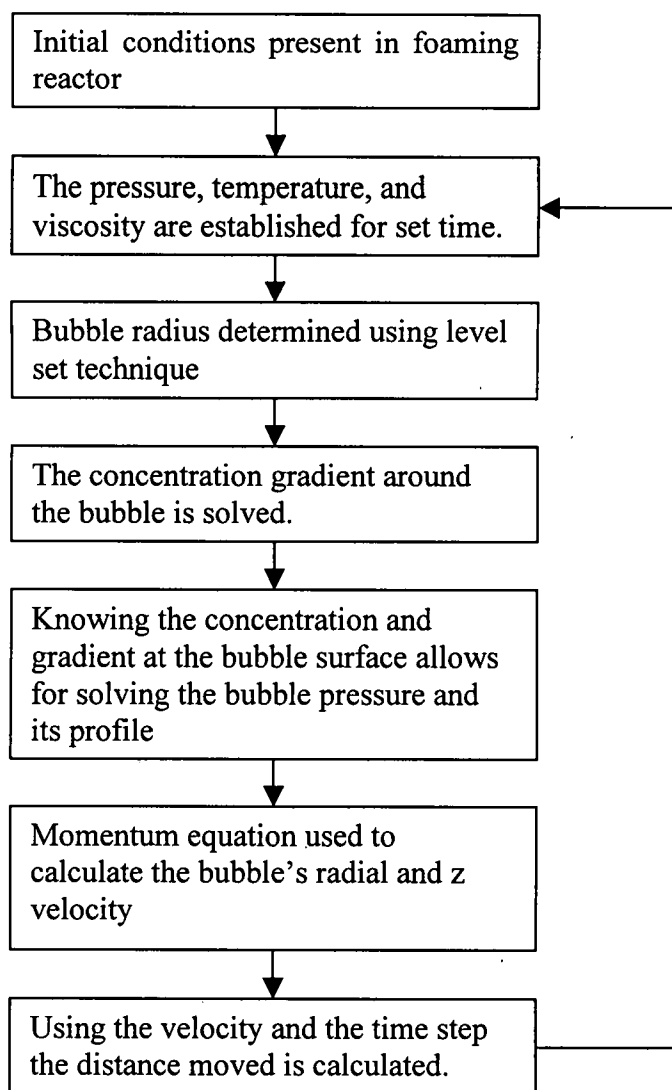


Figure 3-3 Flowchart of numerical procedure

Table 3-1 Definitions of parameters used

Diffusivity	D	$1 \times 10^{-9} \text{ (m}^2\text{/s)}$ [99]
Henry's constant	Kh	$4.73 \times 10^{-5} \text{ (mol/N m)}$ [99, 108]
Initial concentration	ci	$416 \text{ (mol/m}^3\text{)}$ [99, 61]
Initial viscosity	μ_i	$46 \text{ (Pa}\cdot\text{s)}$ [28]
Surface tension	σ	0.035 (N/m) [24]
Density of liquid	ρ_l	$1260 \text{ (kg/m}^3\text{)}$ [24]
Critical bubble radius	Rc	$1 \times 10^{-6} \text{ (m)}$ [57]
Time step	tc	0.001 (s)
Spacing of nodal grid	gsp	$1 \times 10^{-7} \text{ (m)}$

The study's main purpose rests in its ability to predict bubble growth and movement during actual foam processing, thus allowing for better process control and in turn tailorable foams that can meet the needs of a desired application. To maintain the realistic nature of the foaming process, the viscosity profile used is directly obtained from actual foam processing. This is shown in figure 3-4 and is obtained using data acquisition during the foaming process combined with using similar techniques as described in [61]. Though the viscosity may seem high for the trend line, the model assumes that over 1000 Pa·s is towards the solid state and thus quickly preventing other activities from occurring.

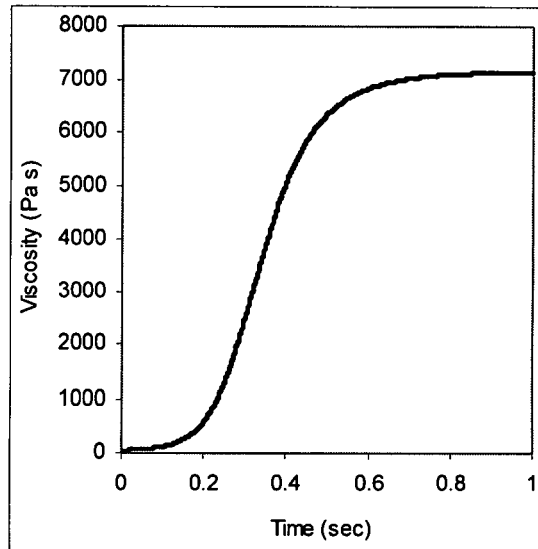


Figure 3-4 Experimental viscosity profile used in simulation

With the experimentally determined parameters, the model is capable of handling the unique dynamic dimension of the problem. This will allow the model to retain its validity throughout the entire range of bubble growth and movement.

3.0 Results

The bubble growth and movement is limited in the simulation by a couple factors. As mentioned previously, the viscosity continues to change during the simulation. With its increase, the liquid pitch transforms to a solid, prohibiting growth and movement along with terminating the simulation accordingly. Secondly, carbon foam bubbles average 100 microns upon foaming completion as is also seen in the model, thus the numerical program is limited to such a condition to reduce in the extensive amount of time needed for these numerical calculations.

Figure 3-5 demonstrates typical bubble growth and location with time using known profiles for the system pressure, liquid viscosity and concentration

of diffused gases. As shown from the figure, the bubble experiences a movement simultaneously with the growth until it reached a radius of 100 microns, the point that corresponds to the sudden viscosity increase. It is notable that the movement of singular bubble does occur, however this motion is orders of magnitude less than the radial bubble growth. Also one can see that the growth profile follows the known $t^{1/2}$ trend [57, 109]. At the beginning, the current model departs slightly as shown in figure 3-6 but small deviations are known to occur for these early times [57]. The growth trend is even more representative in an article by Joshi et al. [109] who modeled diffusional growth in a viscoelastic medium of polyethylene using an influence volume approach.

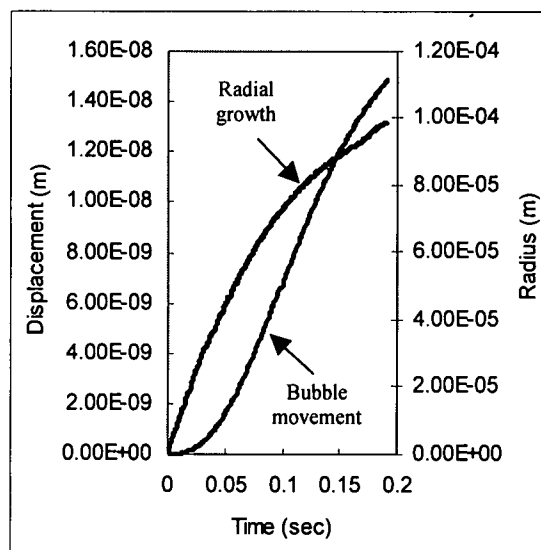


Figure 3-5 Bubble growth and location using original processing conditions

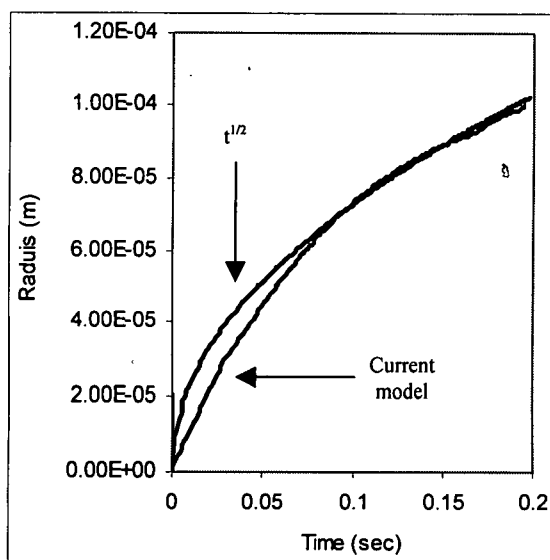


Figure 3-6 Comparison of the current simulation to $t^{1/2}$

The internal bubble pressure is also examined with time as shown in figure 3-7. The pressure takes a sudden drop then levels out. However, the bubble pressure does not reach the external system pressure before the viscous forces restrict growth and movement. The high pressure difference is a driving force in the bubble growth and is counteracted by the high viscous forces. The high bubble pressure is needed otherwise the viscous forces will prevent movement and cause the bubble to collapse.

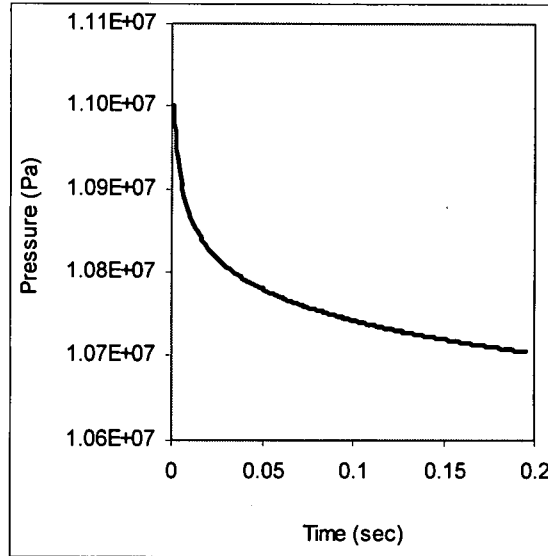


Figure 3-7 Change in bubble pressure using original processing conditions

Along with observing growth and movement, dimensionless parameters are also monitored such as the Reynolds number, Re , the Weber number, We , and the Peclet number, Pe [106].

$$Re = \frac{\rho_l g^{1/2} R^{3/2}}{\mu_l} \quad (21)$$

$$We = \frac{\rho_l g R^2}{\sigma} \quad (22)$$

$$Pe = \frac{\rho_l c_{pl} g^{1/2} R^{3/2}}{k_l} \quad (23)$$

Where c_{pl} is liquid heat capacity and k_l is the liquid thermal conductivity.

Figures 3-8a and b show the trend lines of these parameters during the foaming process. As shown in figure 3-8a, the Reynolds number displays a peak at 0.09 seconds. Since the Reynolds number, equation (21), is a function of bubble radius and the liquid viscosity, conclusions can be inferred. The maximum value demonstrates that the radial growth which represents the inertial force, has the larger effect until a time of 0.09 seconds. The viscous forces at

this point are increasing faster than the growth, thus lowering the Reynolds number. This effect can then be seen in the motion of the bubble in figure 3-5. During the growth process, an increase in buoyancy forces leads to a bubble rising. Once the viscous forces overcome the buoyancy forces, the momentum of the bubble is reduced. This will cause the bubble to slow until it stops at a fixed location, seeing as the liquid pitch is approaching a solid state preventing continued growth or movement. Though the movement appears to slightly lag the peak, it does change from concave up to concave down at 0.11 seconds after the onset of growth. This is reasonable since the bubble's momentum needs to be hindered before the bubbles motion can slow.

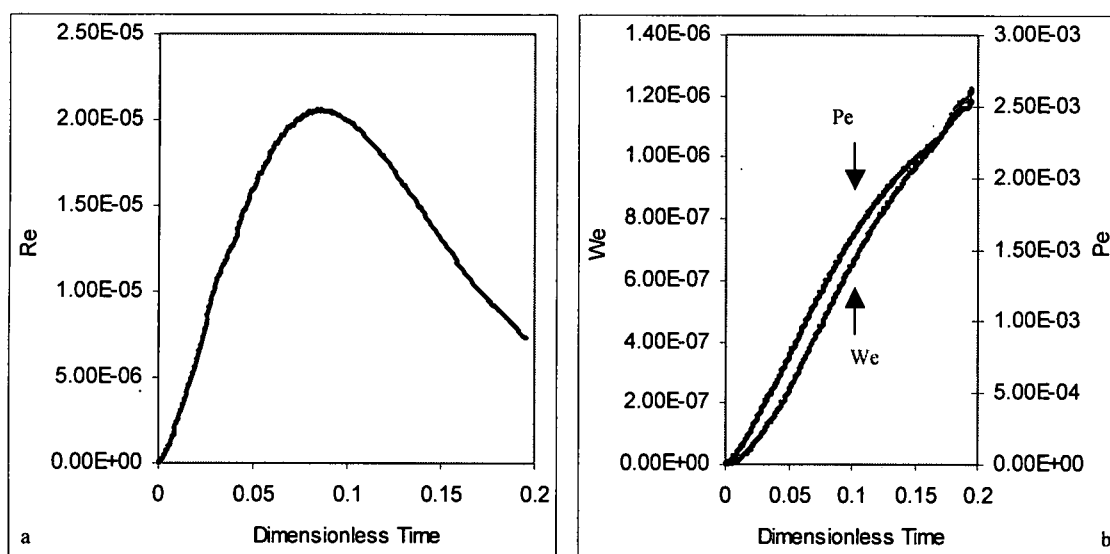


Figure 3-8 (a) Reynolds, (b) Weber, and Peclet numbers during the process

On the other hand, Weber and Peclet numbers increase during the foaming process due to their strong dependence on the bubble radius, as shown in figure 3-8b. For the numerical model, the surface tension, heat capacity and thermal conductivity have been held constant, thus results in these numbers

rests solely in the inertial force's capability to overcome the other forces. As is seen in the definition of the dimensionless parameters, the Weber number has a stronger dependence on radius than does the Peclet number, thus fluctuations in radius are highly evident with such a number. The bubble radius continues to increase with time though the rate of growth decreases due to viscous forces. Slower growth results in a tapering off of the Weber and Peclet numbers as seen in figure 3-8b. Since the trends are relatively similar and the Weber number is more pronounced, the Peclet number will not be implemented in the parametric study. It is notable though that for most foaming processes the Peclet number is relatively small [99] as also seen in figure 3-8b.

4.0 Parametric Study

A parametric study is undertaken on the numerical model to elaborate the effects of initial bubble pressure and radius as well as viscosity on the process. Through the use of Reynolds number and Weber number [106], the model can be compared to others in literature as well as determining the parameters that have the largest effect on growth and movement.

4.1 Initial Bubble Pressure Effect

To investigate the effect of the initial bubble pressure into the growth and movement of the bubble, the model is applied for different initial bubble pressure levels ranging from 0.1 to 10 times the suggested P_{go} [99, 108]. As expected, lowering the initial bubble pressure has a drastic effect on both the bubble growth and movement. Lowering the initial bubble pressure reduces the pressure

difference between the gas and the liquid. This is a major driving force in the bubble growth, thus the growth is slowed and in turn the movement of the bubble is reduced as is seen in figures 3-9a and b.

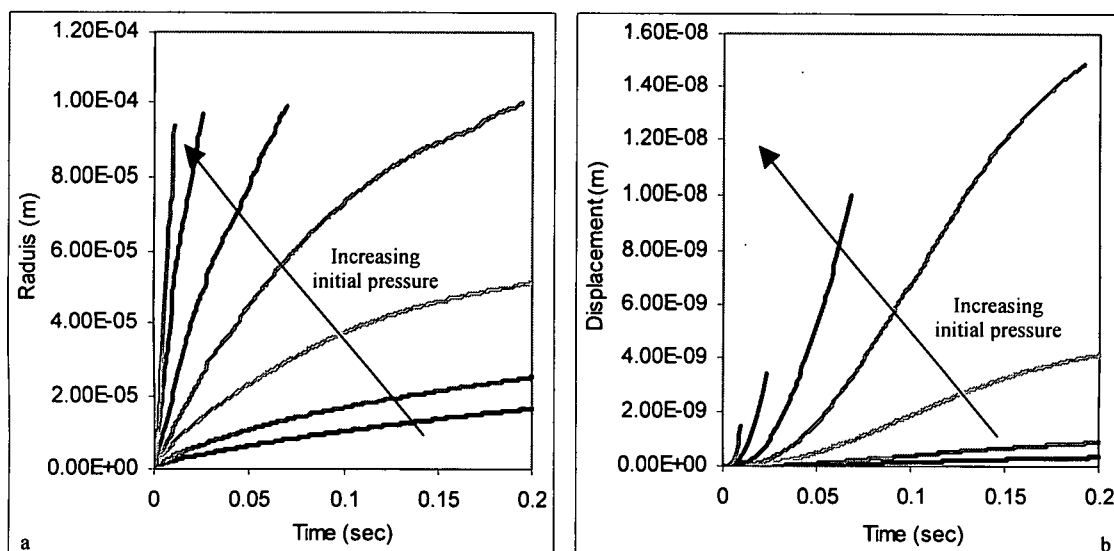


Figure 3-9 (a) Radial growth and (b) bubble location with varying initial gas pressures

The lowering of the initial pressure results in a lowering of the inertial effects. In turn, the viscous forces are more dominant than the force due to bubble velocity, thus the Reynolds number is also lowered. Again smaller movement of the bubble at lower initial pressures corresponds to lower Reynolds numbers. As one can see from figure 3-10a, the Reynolds number continues to increase with elevated initial bubble pressure. At extreme initial bubble pressure no mitigation of the inertial effects occurs and the growth never truly is dominated by viscous extremes as indicated by the lack of a maximum in the Reynolds number and as such movement is maximized as well.

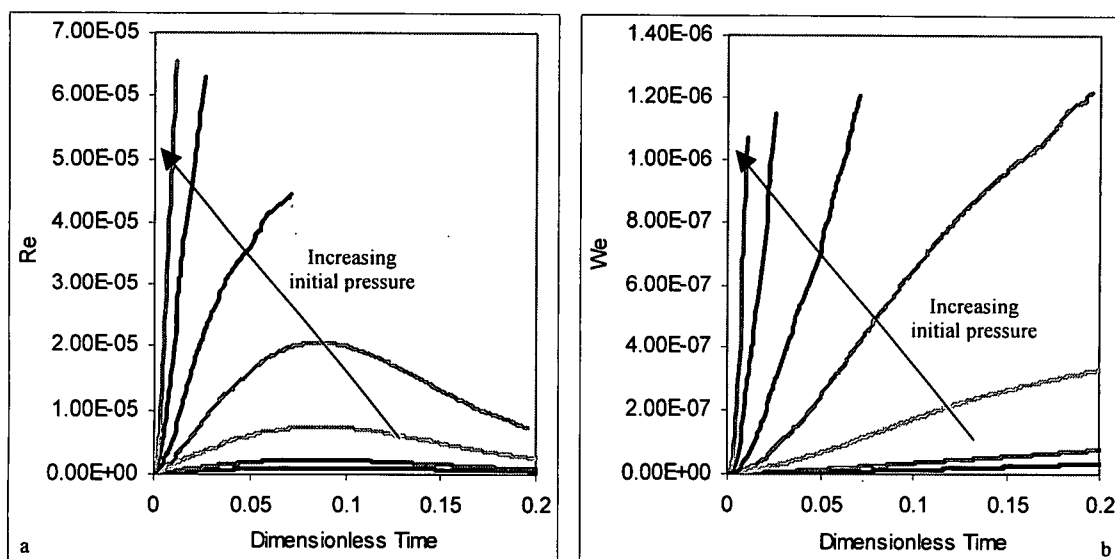


Figure 3-10 (a) Reynolds and (b) Weber numbers changing with time through differing initial bubble pressure

The Weber number, figure 3-10b, gives very similar trend as previously due to the strong radius effect. As the initial pressure is reduced so is the growth as surface tension effects become more significant. Most simply, the slower the growth the more dominant surface tension.

4.2 Initial Bubble Radius Effect

The initial bubble radius is varied from 1 to 20 microns to determine the effect of perturbation on the extent of bubble movement. The initial bubble radius as stated earlier will affect the growth process [99] as is seen in figure 3-11a where the growth rates are increased with larger initial bubble radius. With this increased growth rate the bubble location in time is also affected. With larger bubbles comes greater buoyancy forces and thus greater movement. Though the time necessary to reach 100 microns for larger bubbles is less, the final bubble moves a greater distance as is shown in figure 3-11b. Plainly stated,

increasing the initial bubble radius increases the bubble growth and its movement.

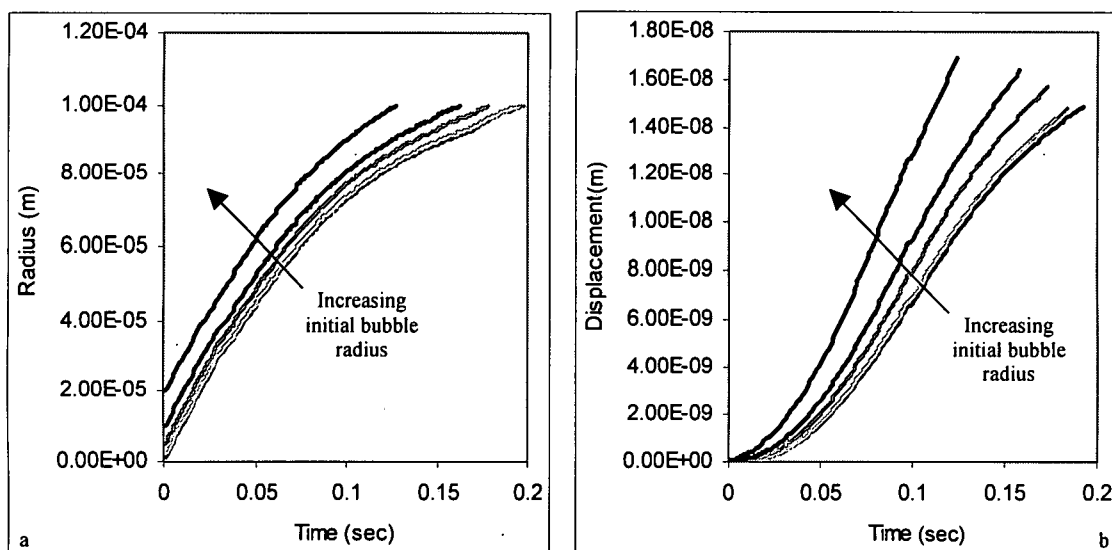


Figure 3-11 (a) Radial growth and (b) bubble location with time through differing initial bubble radius

In figure 3-12a, increasing the initial bubble radius increases the Reynolds number because of the increase in inertial forces coinciding with higher growth rates. Again the Reynolds number experiences a maximum value where the viscous effect overcomes the inertial effect. This result signifies that the viscosity increases at a greater rate than the bubble is capable of growing. Although the larger bubbles have more buoyancy, their movement is limited by this quick increase and dominance of viscosity.

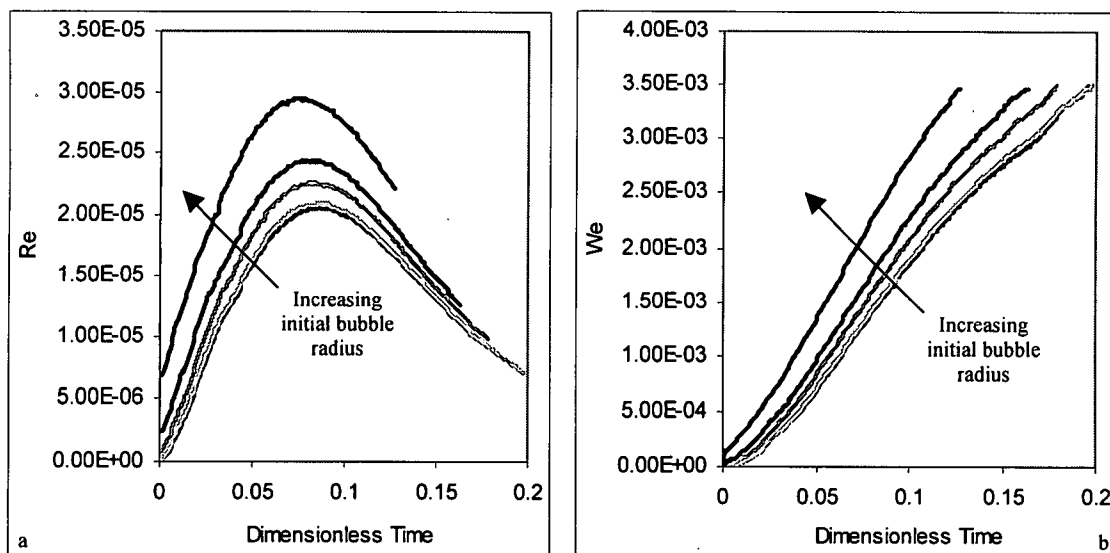


Figure 3-12 (a) Reynolds and (b) Weber numbers changing with time through differing initial bubble radius

The Weber number again has a similar profile where it increases with time because of increasing bubble radius. Note however, by increasing initial bubble radius, the growth rate is increased, consequently providing a slightly different slope for the various trend lines.

4.3 Viscous Effects

Though the effect of viscosity has been fundamentally disregarded in much of the prior modeling of the foaming process, its changing nature has been found to have a prevalent effect [110]. Beechem et al. [61] have included this in their model of non-spherical bubble growth through adjusting the rate at which viscosity increases. The current study goes one step further, modifying the viscosity profiles in two different ways, with respect to both the rate at which viscosity increases and its initial value when growth commences.

4.3.1 Viscosity Rate Effect

Shown in figure 3-13a are the differing rates of viscosity change implemented in this study of which the intermediate line corresponds to the values acquired during processing. The range encompasses from 0.2 to 5 times that of the rate of viscosity change previously determine in figure 3-4. The initial viscosity for all profiles is 46 Pa·s which occurs at a temperature of 300°C [28] but the time necessary to reach the final viscosity varies. In the carbon foam process, the pitch changes from a liquid to a solid in a fraction of a second. Thus, the numerical program ceases when the viscosity exceeds 1000 Pa·s, a point at which bubble growth ceases to continue. By investigating this effect, it was found that as the rate of viscosity change increases both bubble growth and movement decrease as displayed in figures 3-13b and 3-14.

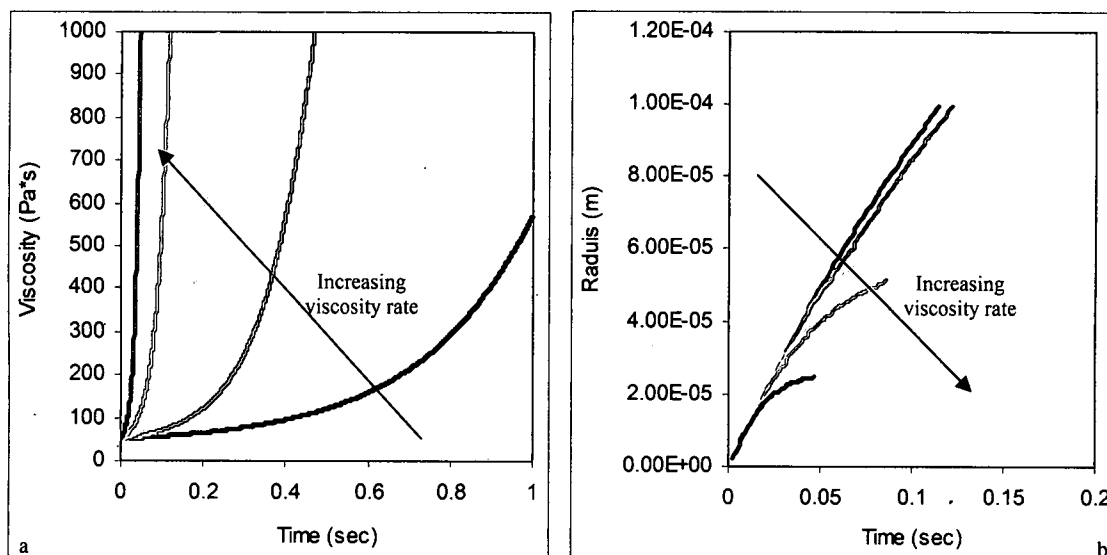


Figure 3-13 (a) Differing viscosity rate of change with time and (b) bubble growth through differing viscosity rate

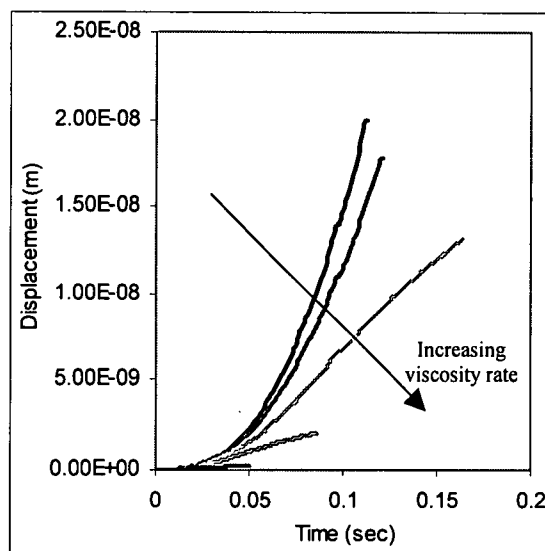


Figure 3-14 Bubble location with differing viscosity rate

The peaks experienced in the Reynolds number are highly dependent upon this rate of viscosity change and give unique perspective at how easily viscous effects can begin to dominate the system, as shown in figure 3-15a. These peaks again correspond to the point at which the viscosity becomes the dominate effect on the system. Therefore, as the viscosity rate is increased, the time to reach the maximum Reynolds number decreases thus indicating a shorter window for growth and movement. It should also be noted that surface tension effects become more predominant as well with increasing rates of viscosity change due to the higher surface effects as is evidenced by the smaller Weber numbers at higher viscosity rates of change, figure 3-15b.

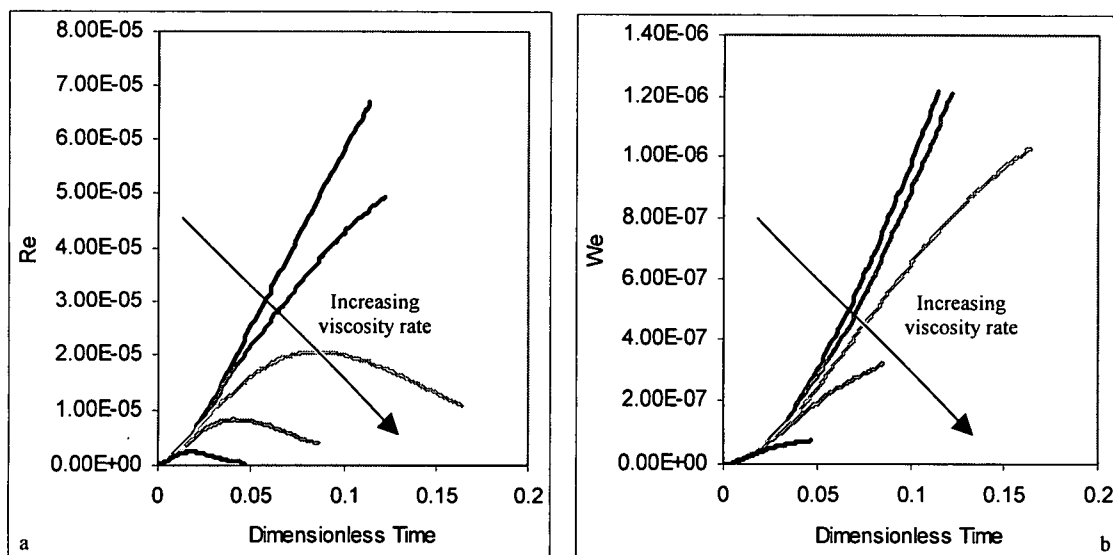


Figure 3-15 (a) Reynolds and (b) Weber numbers through differing viscosity rate

4.3.2 Initial Viscosity Effect

The effect of varying the initial viscosity from 10 to 500 Pa·s is displayed in figure 3-16a. Again the bubble location and growth is monitored as well as the dimensionless parameters. In figure 3-16b, lowering the initial viscosity increases the bubble growth. Setting the initial viscosity to 20 % of the known viscosity causes the bubble to grow to 100 microns four times faster. Increasing the viscosity, however, slowed the bubble growth, preventing it from reaching 100 microns before viscous forces terminated growth.

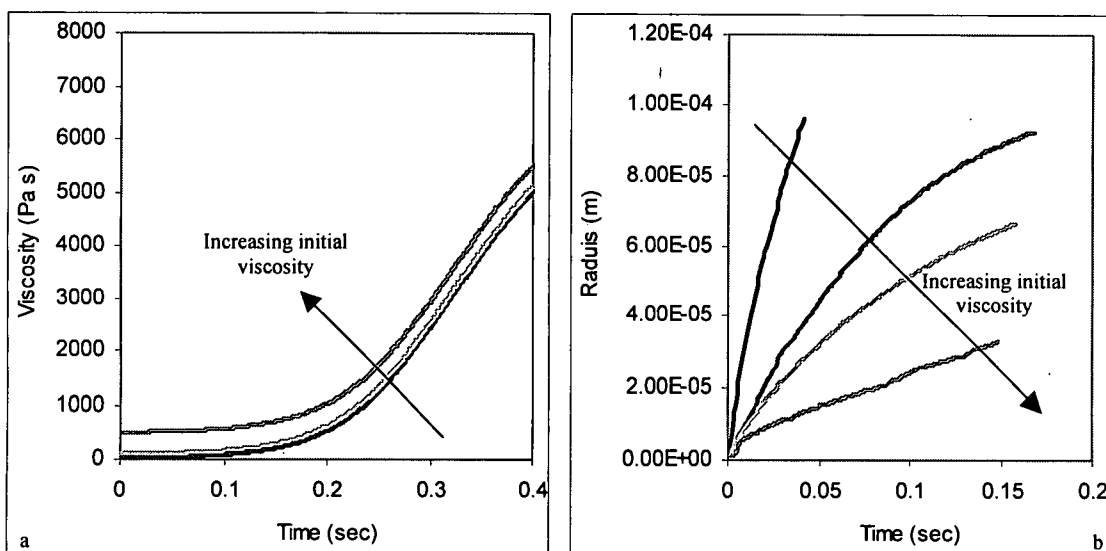


Figure 3-16 (a) Viscosity profiles and (b) bubble growth with differing initial viscosity

Decreasing the initial viscosity also enlarges the movement the bubble experiences as is seen in figure 3-17. The same 20% produces a bubble with a magnitude of movement approximately 1.5 times that of the original. As the initial viscosity continues to increase the bubble becomes stationary although the growth still occurs to a limited extent.

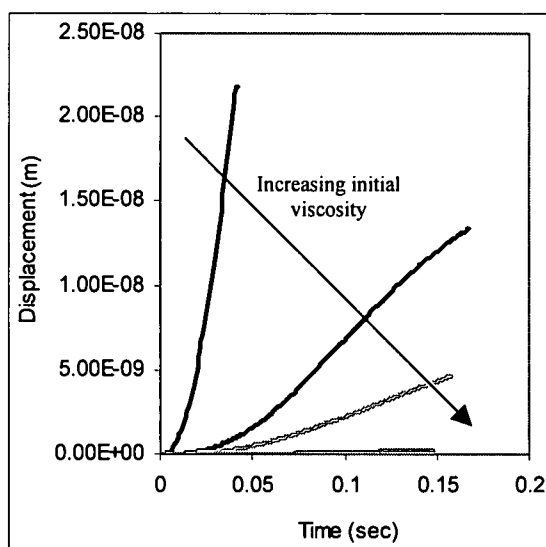


Figure 3-17 Bubble location with time through differing initial viscosity

An examination of Reynolds number once again shows why this occurs. The Reynolds number profiles all have a maximum at approximately the same time yet their magnitudes are different suggesting that as initial viscosity is reduced, inertial effects become a more dominant.

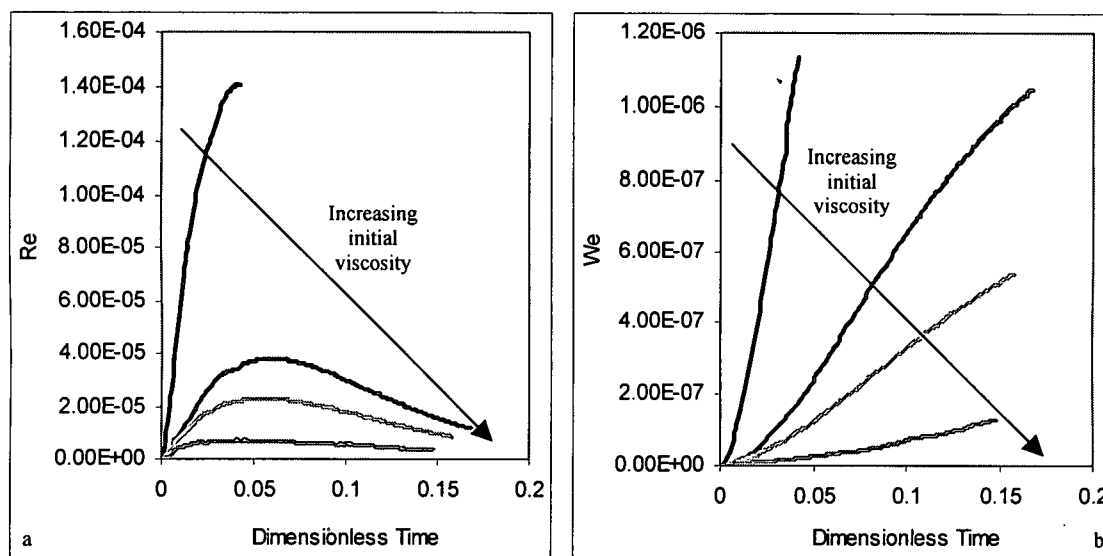


Figure 3-18 (a) Reynolds and (b) Weber numbers through differing initial viscosity

For the Weber numbers, decreasing initial viscosity increases the dimensionless number. Again, lower viscous forces allows for the domination of the inertial forces. When this occurs the growth is more substantial resulting in an increase in the Weber number.

5.0 Conclusions

A numerical model to study foaming mechanism was introduced. The approach was based on understanding the growth and movement of a spherical bubble during foam processing. The numerical model was based on a level set technique for capturing the phase interface. The predicted findings verify that the

bubble experiences a movement simultaneously with the growth until the liquid pitch approaches its solid state. This movement however is magnitudes less than the subsequent growth. Through the contribution of non-dimensional parameters, it was found that the increase of initial bubble radius causes an increase in both the bubble growth rate and movement. Conversely, lowering the initial bubble pressure slows the growth and in turn reduces the bubble movement. It was found also that decreasing the initial viscosity produces an increase in both the bubble growth and movement. The predicted results shed light on carbon foam formation, which will assist the achievement of tailoring carbon foams.

Chapter IV

Fractionation of Mesophase Pitch

The pristine pitch material, Ashland pitch, referred to as A80, contains three fractions; gamma, beta, and alpha fraction. These fractions were extracted using soxhlet fractionation technique and various solvents such as toluene and quinoline. The gamma fraction is soluble in both where as the beta fraction is quinoline soluble and insoluble in toluene. However alpha fraction is insoluble in both quinoline and toluene. The viscosity of pitch increases with increasing of molecular weight. In this case, the alpha fraction is made of the highest molecular weight. Conversely, the beta fraction is composed of medium molecular weight and the gamma fraction contains the lowest molecular weight. Thus the viscosity of the alpha fraction is magnitudes higher than that of the beta and gamma fractions. The gamma fraction behaves like tar with the viscosity being so low.

Each fraction has a different softening temperature, therefore, foaming occurs at different temperatures while keeping a constant pressure. The alpha fraction, with its extremely high viscosity, prevented foaming at elevated temperature, maintaining a solid state. Foaming the gamma fraction was possible but its prolonged stabilization time of nearly a month at 170°C reduced the foam's performance. However, the beta fraction seems to exhibit the proper viscosity range where foaming was possible and where a low stabilization time

occurs. As shown in figure 4-1, the following foam strengths and densities were determined from foaming at 1000 psi and 270 °C. It is inherent that increasing foam density increases the strength. On a specific scale these are all relatively similar. It seems that the strength and stiffness of all commercial foams are relatively low compared to titanium honeycomb which limits their commercial use. Sihh has modeled the mechanics of carbon foam with this data displayed as a curve in the following figure. This matches the foams experimental strength data, designated as circular and trigonal dots in the same figure [111]. Foams made from beta fractions, represented as diamond dots, also exhibit a wide range of strengths as a function of density, however, the overall strength is five times better than commercial foams as is seen in figure 4-1. As found in pitch based carbon fiber processing, increased performance could only be attained through using fractionated pitch, thus similar approach was implemented in carbon foam production.

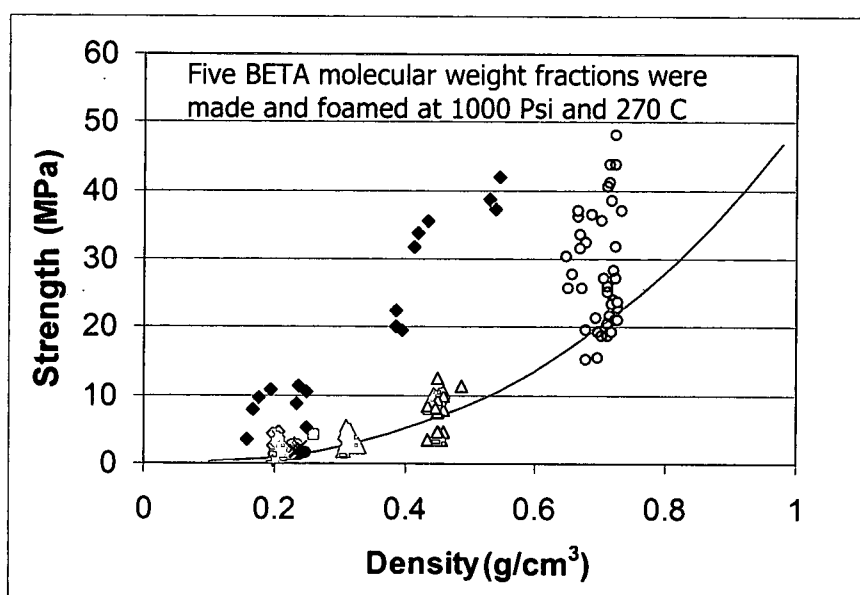


Figure 4-1 Strength of beta fraction foams and carbon foams

Chapter V

Carbon Foam and Additive Properties

1.0 Microstructure of Carbon Foams

The microstructure of carbon foams is composed entirely of carbon, thus, it is anticipated that interconnected ligament networks of aligned graphitic sheets can produce carbon fiber-like properties [44, 112, 113, 114, 115]. This microstructure, coupled with the precursor properties, governs the foam's mechanical and thermal behavior through molecular orientation and crystallinity of ligaments and nodes.

Through heat treatments, the carbon foam's molecular structure changes. The changes that occur through graphitization are well understood [116]. As the heat treatment progresses, the carbon skeletons become very straight and stiff to reach the minimum interlayer spacing of the graphitic structure, figure 5-1. These changes in molecular structure cause predictable changes in the material's crystallinity.

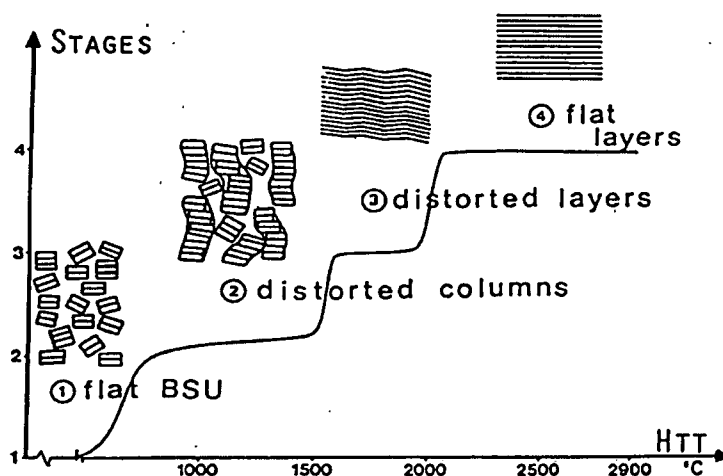


Figure 5-1 Structural changes as function of heat-treatment temperature [116].

Disclinations occur frequently in carbon microstructure. They are produced during the formation of Brook and Taylor mesophase spheres, the liquid crystal pitch precursor material. Subsequent growth and deformation of these mesophase spheres lead to disclinations. Typical disclinations are wedge and twist shaped as shown in figure 5-2. As polymerization continues and the carbonaceous mesophase hardens, the disclinations are retained. Further heat treatments do not anneal out these disclinations, but instead provide order of the layers around them, ultimately leading to a graphitic atomic structure. The final graphitic structure containing fixed disclinations are important to the physical properties of the carbon matrix as shown in the studies of White and Zimmer [117, 118].

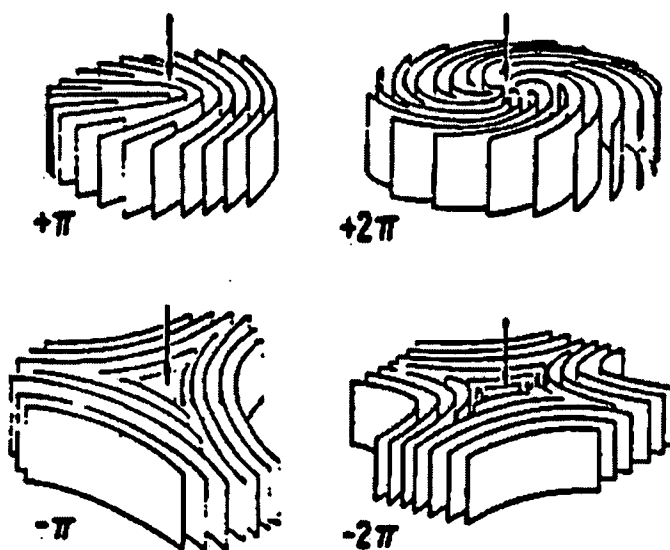


Figure 5-2 Disclinations in carbonaceous mesophase. In this figure, the layers represent the general preferred orientation of the platelike molecules of the discotic nematic liquid crystal.

Figure 5-3 shows the crystalline structure of typical carbon foam as well as the wide range of bubble sizes that occur during processing. The thickness and the elongation of both nodes and ligaments may vary from one location to another, as seen in figure 5-3. In general the ligaments are homogeneous with a preferential orientation. They might contain some disclinations, figure 5-4a, but as the ligament diameter decreases, so do the disclinations, figure 5-4b.

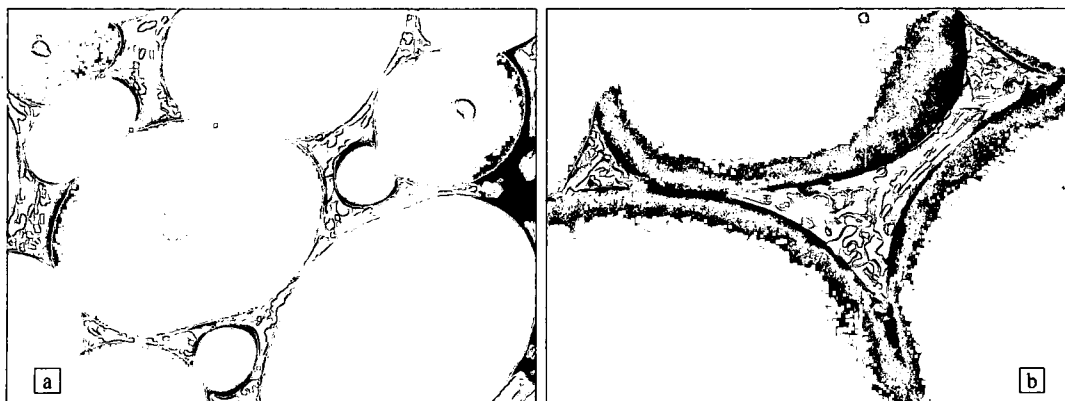


Figure 5-3 (a) low magnification optical micrograph of stabilized carbon foam and (b) optical micrograph of stabilized carbon foam showing both ligament and node

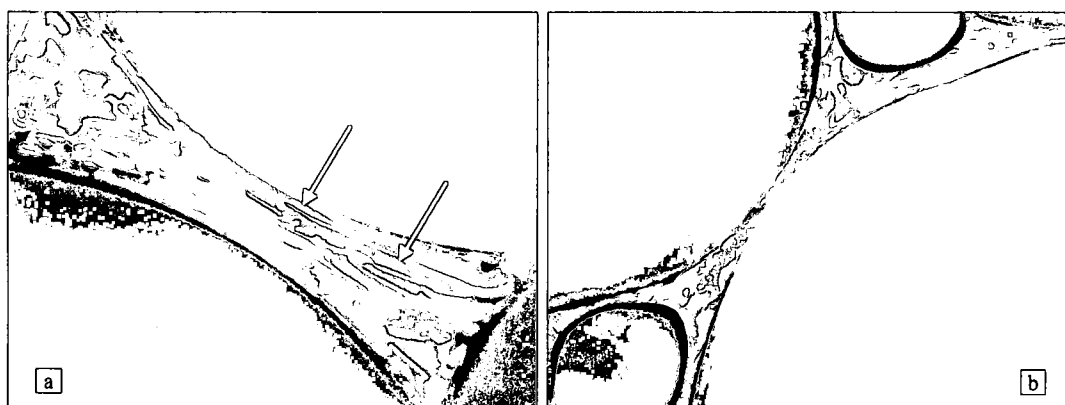
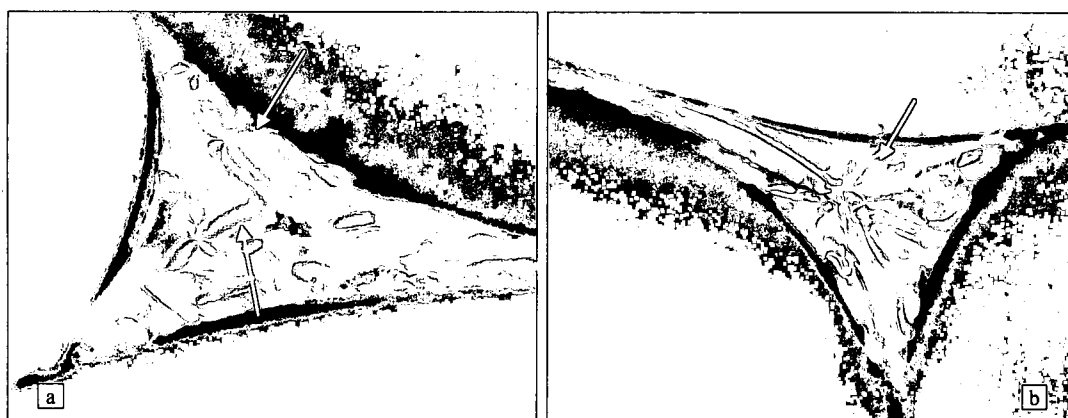


Figure 5-4 Ligaments with disclination



Figures 5-5 Nodes with disclination

After carbonization and graphitization, the bubble size increased while the thickness of ligaments decreased. This results in two types of ligaments, those

with and those without disclinations. Ligaments free of disclinations are highly oriented whereas those with include some cracking. It is also noted that the nodes are mostly full of disclinations with large random orientation of the graphene layers.

Figure 5-6 shows a bright field image of graphitized carbon foam. This general view shows both ligaments, single arrows, and nodes, double arrows. Most of these ligaments and nodes are thin enough for TEM investigations. Figures 5-7a and 5-7b show highly magnified dark field and bright field images of the circled area in figure 5-6. These images illustrate highly aligned planes parallel to the axis of the ligament free of disclinations. This is the same scenario as is seen in carbon fibers. This high alignment is also observed in the diffraction image, figure 5-7c, where all 00l reflections from 002 to 0014 are visually apparent.



Figure 5-6 Bright field image of graphitized foam. TEM sample preparation was performed using an atomic milling technique.

Figure 5-8 displays the second type of ligaments in which the concentration of wedge and twist disclinations is considerable. There is fairly good orientation of graphene sheets parallel to the ligament axis, but this preferred orientation is interrupted by various disclinations. In this case, the $-\pi$ disclination is observed. However within a given grain, the alignment of the graphene layer is perfect.

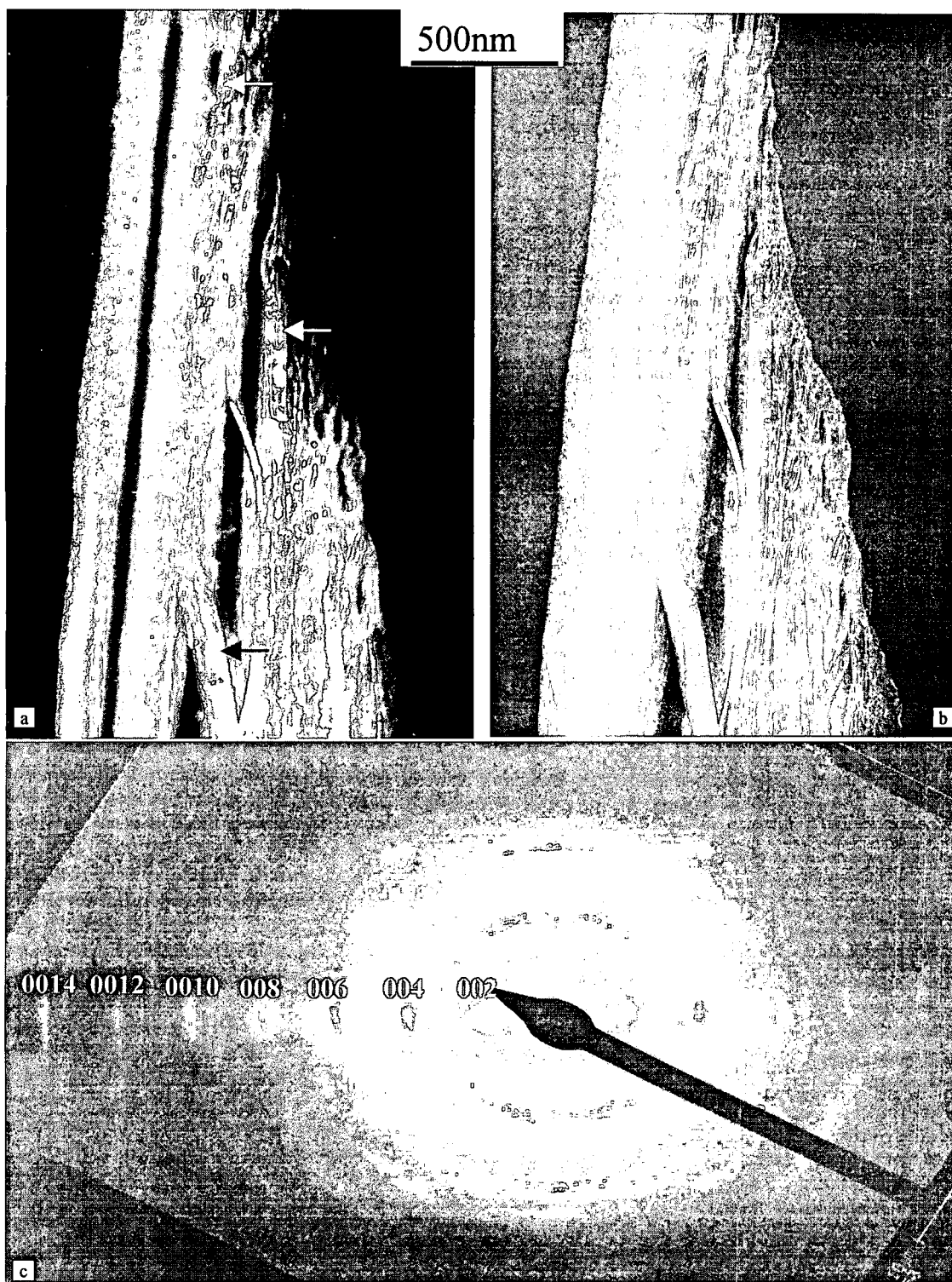


Figure 5-7 (a) and (b) 002 Dark field and bright field images of ligament relatively free of disclinations; (c) selected area diffraction of centered area of ligament free.



Figure 5-8 High resolution image of areas on the ligament showing preferential orientation and $-\pi$ wedge disclination.

Graphitic materials are the only materials in which disclinations exist and play a key role in material properties. Disclinations are prominent in the microstructure of graphitic foam. The type and distribution of these disclinations could play a crucial role in the physical performance of graphitic foam such as fracture toughness and thermal properties. The concentration of these disclinations and their orientation is dependent on material precursors and foaming conditions.

Carbon foams lack of mechanical performance is due primarily to the presence of defects or high graphitic order of ligaments. To enhance foam mechanical properties, one should have similar thoughts and processes applied to improve carbon fiber performance. Most carbon fibers exhibit a Young's modulus ranging between 500 and 900 GPa and tensile strength of 5 GPa. The high value of modulus is related to its graphitizability however the strength is due to its folding and zigzag structure seen in figure 5-9. The zigzag texture plays a key role in preventing the shear planes in graphitic materials and enhances the tensile strength properties of carbons through an interlocking mechanism of the graphene layers. The same mechanism explains the high mechanical properties of carbon whiskers and high-modulus carbon fibers. Thus, the idea of additives was proposed. Upon foaming, additives placed into the carbon foam precursor provide a possibility of creating a similar zigzag structure.

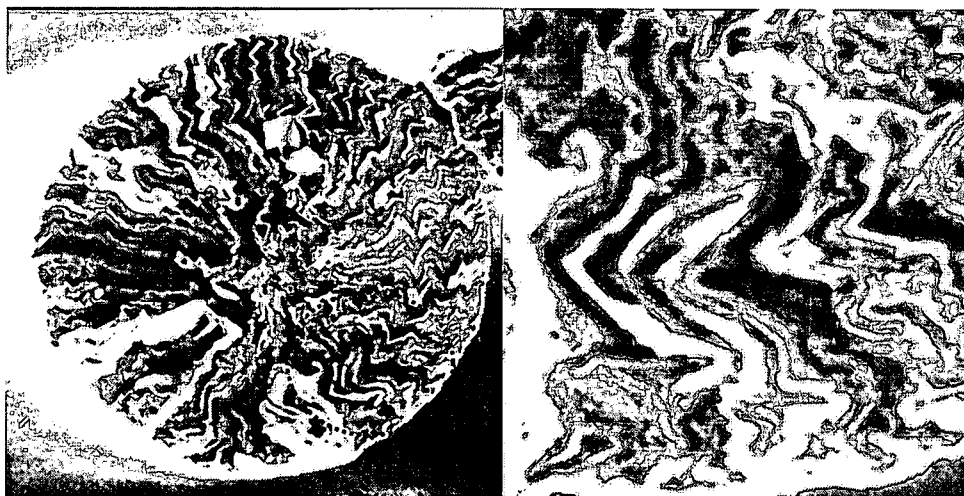


Figure 5-9 (a) Cross section of pitch based carbon fibers. (b) High resolution imaging of areas of folding and zigzag textures (circled area in Fig. 5-9a).

The additives, along with enhancing the zigzag structure, have inherent properties that can improve the overall properties and performance of the new filled foam. Additives are used to increase the strength and stiffness of the foam by focusing on the basic structure of the ligament itself as stated above. If the alignment of the graphene layers can be controlled and improved, so shall the bulk properties. As stated by Donnet, the ligament strength is directly related to crystalline alignment [1]. Some alignment inherently occurs by the strain that is applied on the material from simultaneous bubble growth, but with the use of additives this can be amplified through a change in the chemistry of the precursor. Additives used in this study are of small size and high surface energy which allows for interactions to occur with the host material. These chemical interactions alter the viscosity as well as molecular structure of the host precursor. Additives can also act as a band aid to ligament failure. In the weaker pitch material, cracks may propagate during loading. Without these additives to terminate the cracking and hold ligaments steadfast, a minuscule crack inside the

ligament may become detrimental, ultimately leading to inadequate carbon foams with low performance.

Additives used in this study will be explained in further detail in the sections that follow.

2.0 Carbon Fibers

Carbon fibers are typically made through the PAN process, through the use of a linear polymer with a C-H backbone. The polymer is spun, stretched and dried. This is followed by a stabilization, carbonization, and graphitization step. A pitch process is also used where mesophase pitch is spun into fibers and heat treated in a similar manner as the PAN process.

Ultimately, the resulting fibers have a final diameter of 7 to 10 microns with strengths of 55 to 120 msi and stiffnesses around 250 to 325 ksi.

3.0 HHT PS Nanofibers and Silver Coated Nanofibers

Carbon nanofibers can be vapor grown in a variety of ways including arc-discharge [119, 120], laser ablation [121, 122, 123], chemical vapor deposition (CVD) [124, 125, 126], gas phase-catalytic chemical vapor deposition [127], and plasma-enhanced chemical vapor deposition [128, 129, 130, 131]. Typical processing involves the pyrolysis of hydrocarbon in the presence of a metal catalyst. Unfortunately, this catalyst remains on the end of the fiber as an impurity. This can be removed under certain heat treatments.

Nanofibers are processed in several grades based on their heat treatment. Non-heat-treated nanofibers are referred to as PS nanofibers. When a low heat

treatment is used the nanofibers are listed as LHT nanofibers and to follow suit, the high-heat-treated are referred to as HHT nanofibers [132]. There is only a slight difference in surface energy between the various fibers, however the lack of iron impurities in HHT nanofibers, as seen in table 5-1, makes it most desirable.

Table 5-1 Properties of Nanofibers [132]

		<i>Surface Energy</i>	<i>Iron Content</i>
PR-19-PS	Pyrolytically stripped	36 mJ/m ²	3.8%
PR-19-LHT	Graphitized fiber	40 mJ/m ²	3.6%
PR-19-HHT	Iron seed free graphitized fiber	36 mJ/m ²	10 ppm

The additive used in this study is the highest grade, the HHT nanofiber. The nanofibers were also used in a silver coated state. Through the use of silver sputtering, the nanofibers were completely coated with silver, rendering them electrically conductive in the hope that their implication would yield an electrically conductive foam.

4.0 Single Wall Nanotubes

As with nanofibers, single wall nanotubes can be vapor-grown in the same way. Some include arc-discharge [119, 120], limited laser ablation [121, 122, 123] in small amounts, chemical vapor deposition (CVD) [124, 125, 126], gas phase-catalytic chemical vapor deposition [127], and plasma-enhanced chemical vapor deposition [128, 129, 130, 131]. These tubes are capable of having small

diameters of 0.7 nm as is observed by Nikoleav et al. Typically these nanotubes have internal diameters of 5 nm with an outside diameter of 10 nm. It is important to note that the proportion of graphitic structures can vary resulting in a wide range of surface energies for nanofibers including nanotubes. Nanotubes however tend to be of high purity and have low out gassing during processing which is beneficial in foaming.

5.0 Carbon Black

Carbon black is produced by two basic processes, the channel process and the thermal process. These processes involve partial combustion or thermal cracking of natural gas oil and other hydrocarbons. The channel process produces carbon black with the smallest particle size of 10 nm with the highest surface area by weight, whereas the thermal process produces particles up to 500 nm with lower weight related surface area. Other carbon blacks include Lampblack and Acetylene black. In general the surface area for carbon black is around 25-150 m²/g with particle sizes ranging from 10 to 500 nm.

Carbon black is most commonly used as a filler and stabilizer in products like rubber. It is also used in pigments and for its UV absorption, electrical and rheological properties. Its most important characteristics include particle size, surface activity and porosity.

Chapter VI

Experimental Preparation and Mechanical Testing Procedure

1.0 Initial Processing and Foaming Procedure

Mesophase pitch is received in pellet form from the supplier. The first step in carbon foam processing is transforming the pellet form to that of a fine powder of around 5 μm . Through the use of a jet mill, the pellets of mesophase pitch were placed into a hopper and jet milled filling the trapping sleeve as is elaborated in Kearns' patent [39]. Once removed, the base mesophase pitch is ready for use. If the carbon foam is to be doped with an additive, the additive and the mesophase pitch are shear mixed together for 40 minutes at 18,000 rpm in a one-to-one methanol-distilled water mixture. Upon completion, the solvents are driven off in a vacuum oven to ensure that moisture will not affect the foaming conditions. It is then coffee ground to break up any remaining solid portions that occurred during drying. This extensive mixing is to ensure a homogeneous mixture with no localized additive areas.

Ten grams of the initial powder or doped powder, figure 6-1a, is next poured into a one-inch cylindrical mold and placed under 24,000 psi of pressure using a hydraulic press. This transforms the powder pitch to a dense solid that is referred to as the preform, as seen in figure 6-1b. The preform is placed in the small Parr foaming reactor. The computerized controller and program monitors

the pressure and temperature inside the foaming reactor. Programs can be constructed to reach a range of conditions in terms of pressure and temperature. The processing conditions can include varying the gas present in the reactor as well as the reactor's final temperature and pressure. The challenge in the experimentation is achieving the desired final pressure and temperature in the reactor with these different gas types. The reactor is initially set to a pressure at room temperature and as the temperature is increased so does the pressure. The pressure-temperature relationship may vary slightly with the gas, thus, obtaining the final conditions can be difficult. To eliminate some of the difficulties, the well known inert nitrogen gas is used throughout the work.

With the reactor sealed and the preform inside, the reactor is purged removing all the oxygen, which can be hazardous in the foam creation. The initial pressure is then set and the heating of the reactor is commenced at $4^{\circ}\text{C}/\text{min}$. From experience and use of the ideal gas law, the final foaming conditions of 1000 psi at a temperature of 275°C were reached on a consistent basis. The reactor is then held at this condition for 20 minutes. By this time, the preform has been transformed into a viscoelastic fluid and is saturated with dissolved nitrogen gas. Next the release valve on the reactor is set to the open position completely releasing the pressure to that of atmospheric pressure in fractions of a second, disrupting the equilibrium inside. The dissolved nitrogen gas coalesces, creating bubbles throughout the fluid, resulting in the final structure of a carbon foam, figure 6-1c. This thermodynamic flash technique was

used with all foams created in this work and is described in further detail in Chapter I Section 2.2.1.

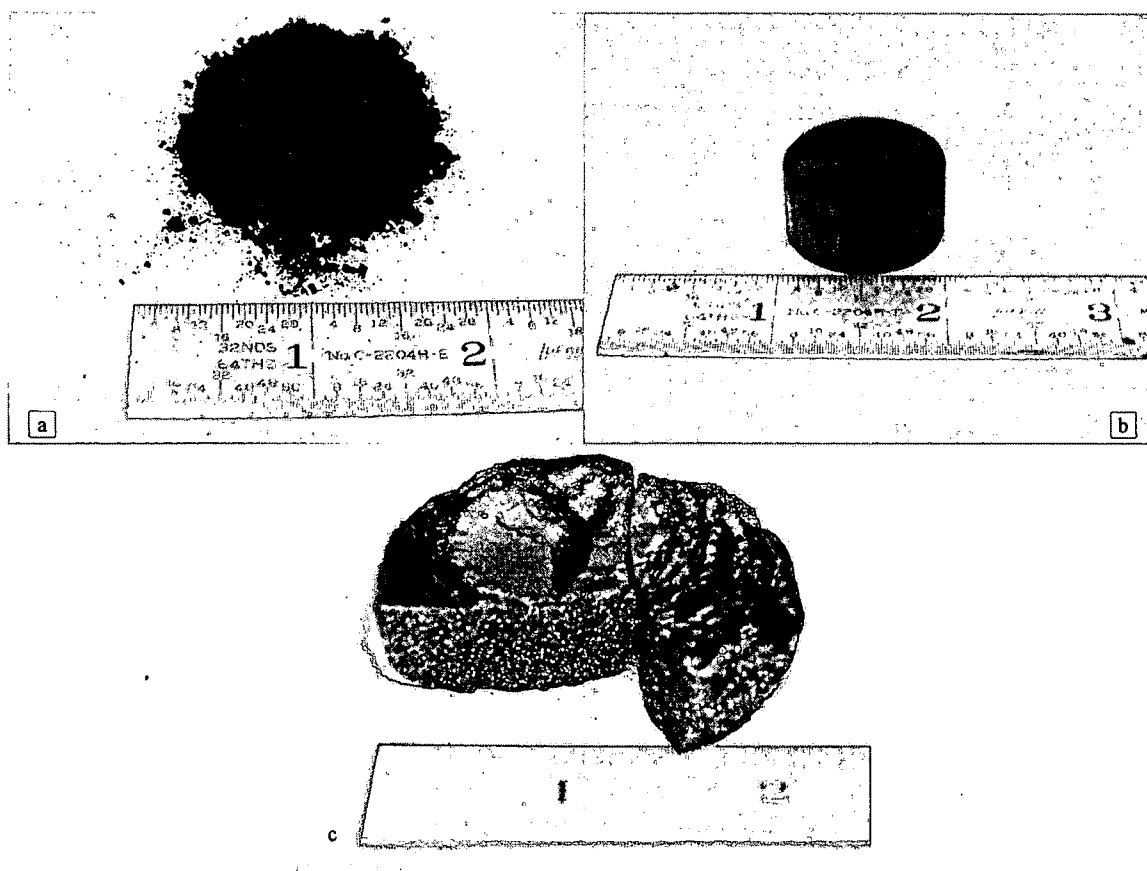


Figure 6-1 (a) Mesophase pitch in powder form, (b) as a preform and (c) as a carbon foam with similar masses.

The foam is then heat treated in coincidence with the stabilization and carbonization steps also mentioned in Chapter I. All foams were stabilized to 7% weight gain to prevent melting, softening, or re-foaming upon carbonization. The carbonization step is then implemented at a heating rate of $4^{\circ}\text{C}/\text{min}$ with a holding period of 1 hour at 1000°C before cooling at the same rate. A graphitization step is sometimes used, but for this study carbonization is the highest heat treatment. At this point the foam is ready for testing. The typical foaming procedure is described as a flow chart in figure 6-2.

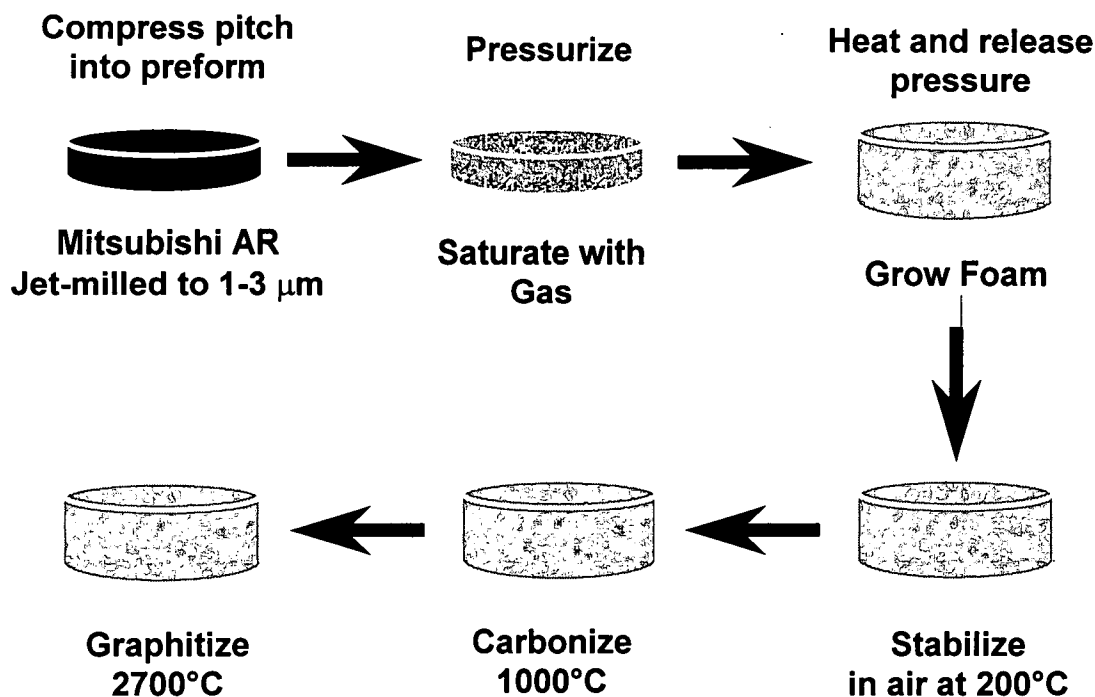


Figure 6-2 Typical processing of mesophase pitch

2.0 Optical Testing Procedures

From each of the carbon foam samples, a representative portion was cut for optical microscope analysis. The cut sample is placed into a mold that was first coated with a Buehler release agent. The carbon foam sample is secured to the mold by a five minute epoxy, Hardman Double/Bubble Epoxy[®]. This is performed so the foam sample will not float upon the addition of the surrounding epoxy. A 3:1 mixture of Miller-Stephenson Epon 828[®] and Jeffamine D-230[®] is stirred by hand until a consistent fluid is formed. The mixture is slightly viscous and light florescent green in color due to the addition of Flouro-Met[®] dye. The active dye, when viewed in the optical microscope with Xenon light, gives an increased contrast which helps in the porosity analysis.

The molds are filled up approximately three fourths full with the mixture

containing D-230 and Epon828. The molds were placed under vacuum at a pressure of 100 mbar then released. This was repeated 3 times to ensure complete impregnation of the foam. By impregnating the entire foam, the foam will not experience deformation or fracture when polishing.

Once the epoxy is hardened, the samples are removed from the molds and placed in the first of two automatic polishing machines. The first machine uses 400 and 600 grit metallographic grinding pads to sand down the samples until a clear cross-sectional view of the carbon foam was available. At this time the plugs are placed on the second automatic polishing machine. A microcloth pad is used, along with polishing alumina. The machine is set to 20 percent and let run over night.

Upon completion, the samples are cleaned and analyzed via the light microscope. A series of images or micrographs are captured of the foam providing a map of the cross section. These images are stitched together and all bubbles are counted with their sizes calculated. This information provides insight into the bubble distribution. Florescent pictures can also be taken to analyze the crystalline structure of the foams.

3.0 Mechanical Testing Procedures

3.1 Bulk Compression Tests

The ASTM standard, ASTM-C1424-99, was used in testing the bulk compressive strength and modulus. The carbonized foams were machined to 0.5 in³ cubes using a diamond saw, providing multiple samples for each doped

foam. A 6000 lb load cell is then used to measure the deformation with a crosshead speed of 0.02 in/min until foam failure occurred in accordance to Gibson and Ashby [43]. The typical set up of the compression testing equipment is shown in figure 6-3a with the sample stage, figure 6-3b. The sample stage was constructed to allow for consistent loading in the z direction during localized failure.

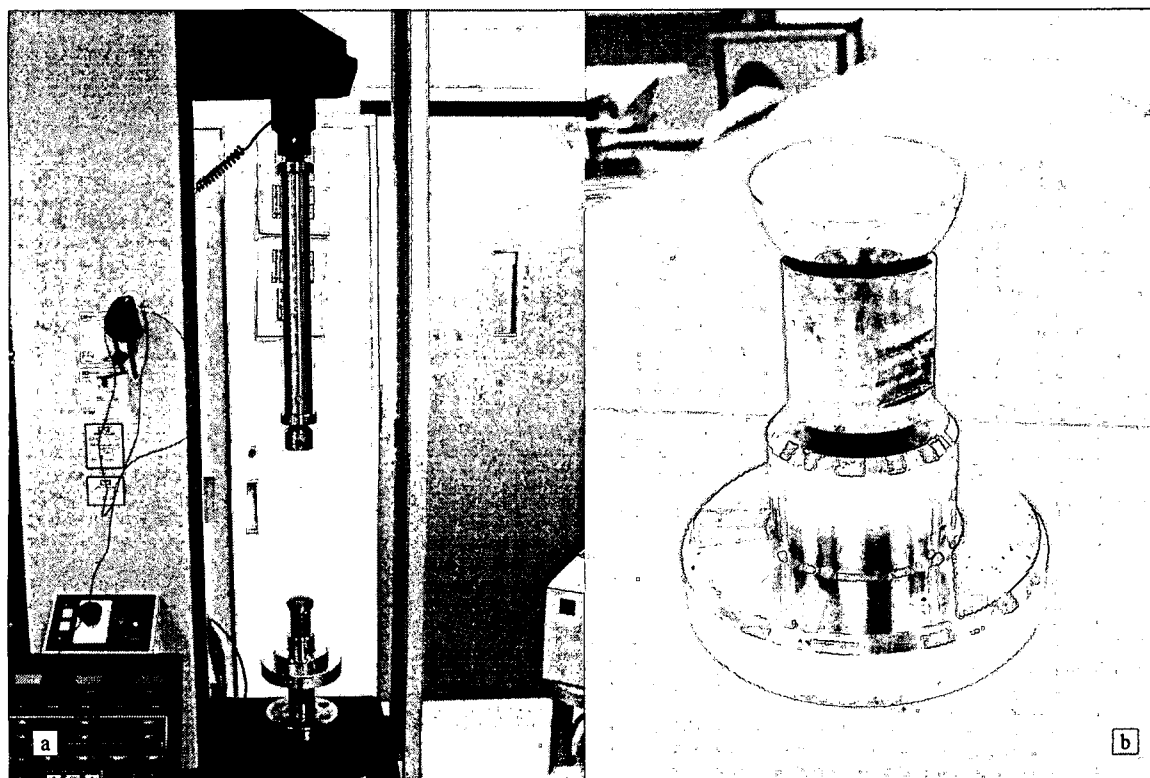


Figure 6-3 Instron and adjustable compression stage

3.2 Ligament Tensile Tests

Testing the ligaments is vital in carbon foam analysis. Ligament information can be scaled up revealing information for carbon foam bulk properties. The effect of additive on foam properties is one purpose of this study,

thus samples containing 5% additive by weight are used in ligament recovery to ensure that the additive is present in said ligament.

A tensile stage was constructed using a 50 gram load cell as seen in the figure below. The ligament is rigidly fixed to the two mounting plates using a soldering iron and sealing wax and is then placed under Olympus BX-41 light microscope with 5X magnification before beginning testing. A Diagnostic Instruments 11.2 Color Mosaic Digital Camera connected to the microscope records each test.

Once the test is set in motion, the NEMA 15 stepper motor, which is attached to one of the mounting plates by a loading arm, strains the test specimen at a rate of 0.75 microns per step. The overall loading rate can be varied through the computer interface by adjusting the number of steps per second. Upon ligament failure, visual and computer recorded data are used to determine a successful test. For each doped sample, 20 successful tests are required to ensure valid results.

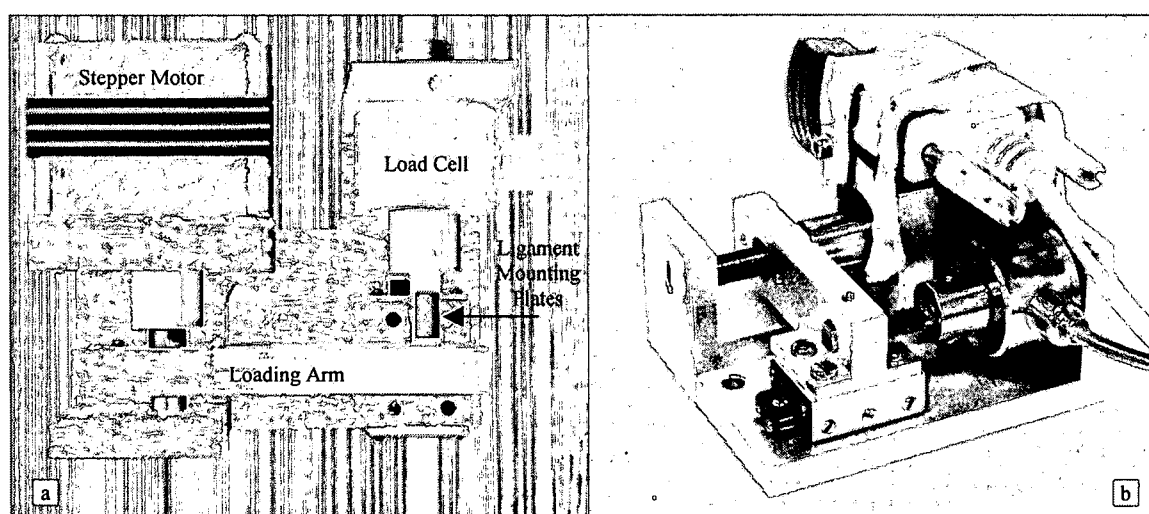


Figure 6-4 (a) Computerized and (b) actual image of ligament tester

Chapter VII

Results and Discussion

1.0 Areas of Study

In this study, the effect of additives in pitch based foams is being analyzed. The study was divided into several major sections. First involves the size of additive and second involves the additive shape. Another area of exploration involves the addition of silver coated nanofibers in the pursuit of creating an electrically conductive carbon foam. In compilation of all doped foam mechanical data, trends on percent additive by weight were also conducted. Through the use of techniques described in Chapter VI these areas will be shown in more detail.

2.0 Effect of Additive Size on Foam Properties

Cylindrical additives are available in many sizes. In this study, carbon fibers were chopped as well as milled providing two different types of large fibers. High-heat-treated nanofibers, HHT, were the medium range fibers with single wall nanotubes, SWNT, as the smallest of the group. The SWNT were used sparingly because of the high cost, thus were not included in the bulk compression analysis.

2.1 Size Effects on Bulk Compression Tests

The size of the particulate has a drastic effect in both the ligament and bulk testing. The same trends are expected since both are interrelated. The final foam is composed solely of ligaments connected by junctions called nodes. Bulk compression data is clearly displayed in figure 7-1 with pitch referring to the carbon foam without any additives, the control. Chopped fibers, carbon fibers cut by hand and coffee ground before the extensive mixing, were seen to lower the compressive strength and stiffness of the foam. Milling these fibers into an almost powder form is seen to increase the strength and stiffness slightly whereas nanofibers are seen to almost double the strength as well as increase the stiffness. To normalize the compression data and allow for such comparisons, the strengths and stiffnesses are put on a specific scale by dividing them by their respective densities. This is necessary because each foam has a different density due to the additive and the processing conditions. The denser the material the stronger it may be. Therefore, specific properties relate all materials on a similar scale and are useful in comparing foams to other structural materials.

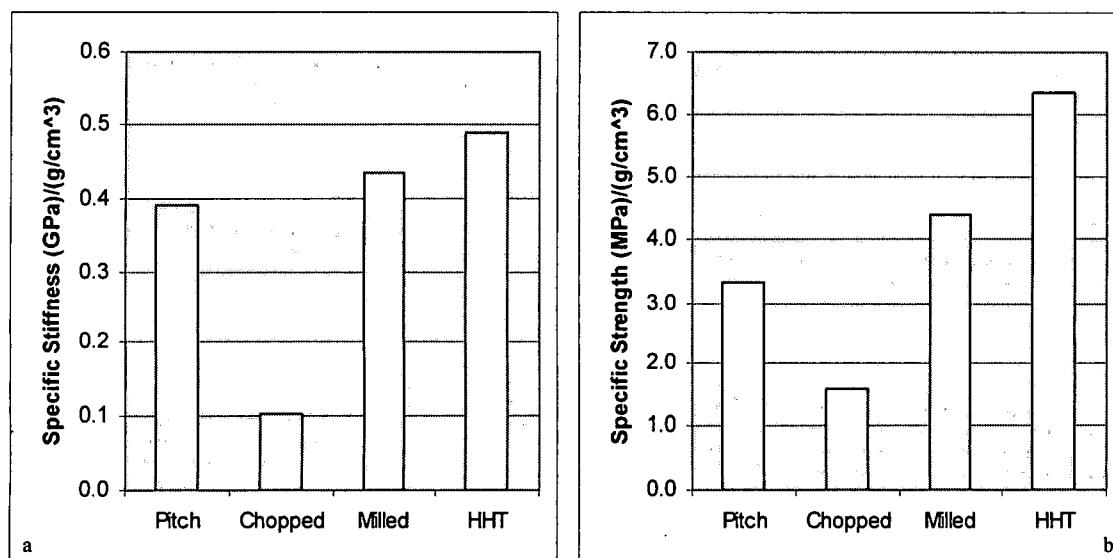


Figure 7-1 (a) Specific stiffness and (b) specific strength of foams with various size additives

Through microscopy, the answer to these varying results was revealed. Through florescent images, the crystalline structure is seen to change drastically between foams. The smaller the particulate, the smaller and more uniform the individual crystals. Figure 7-2 shows the increased zigzag structure corresponding to color change brought on by the additive. Figure 7-2a shows the pitch based foam. The monochromatic ligament indicates a uniform crystalline structure with all the basal planes in the same direction. The milled fiber foam, figure 7-2b, shows a slight increase in zigzag structure evident by the waviness in color. This is followed by the speckled ligament of the HHT nanofiber foam, figure 7-2c. This increased color indicates that the HHT nanofibers produced the greatest amount of zigzag structure of the three.



Figure 7-2 Micrographs of (a) pitch, (b) milled and (c) HHT nanofiber foams

Along with this, there is also seen to be an interface issue with the larger fibers not seen with HHT. At the fiber foam interface, there is a noticeable dissociation. This can be seen by the dark areas located between the fiber and the pitch material in figure 7-3a. Upon the addition of stress, the fibers have a tendency to pull out of the foam because of the weak bond. This is even more evident in the SEM figure, figure 7-3b. The figure also shows extreme cracking caused by the addition of these large fibers. This cracking leads to the foam's lower performance. Decreasing the particulate size increases the surface energy

and thus, provides better bonding or adhesion between the base pitch material and the constituent. This ultimately prevents the cracking from occurring with smaller additives. This beneficial effect is also seen in single ligaments.

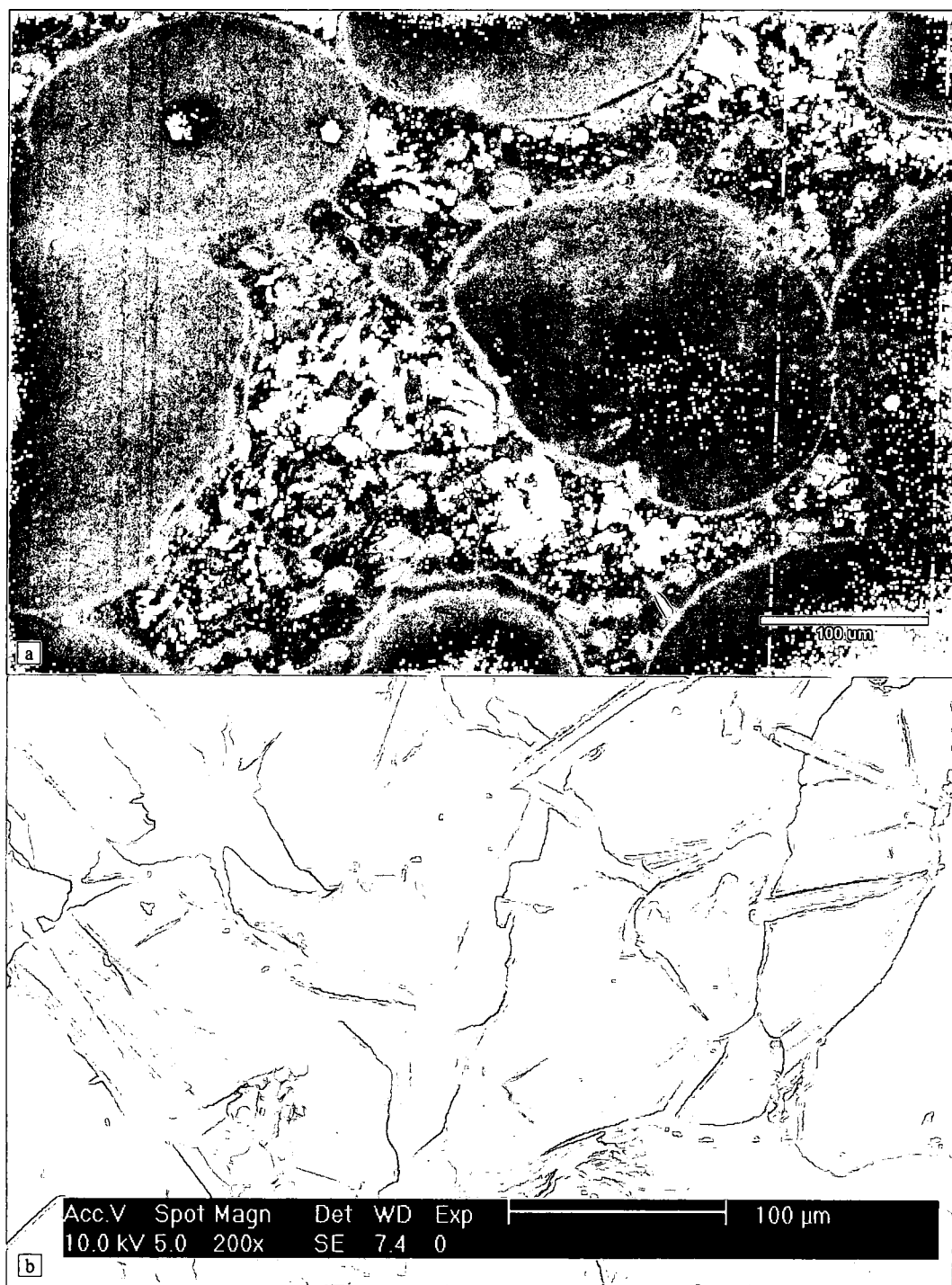


Figure 7-3 (a) Micrograph and (b) SEM of carbon foam containing carbon fibers

2.2 Size Effect on Ligament Tests

The ligaments are a nonporous material, different from the final foam and are all assumed to have relatively similar densities. Therefore, they can be compared directly. The size-dependent ligament testing involves the use of the milled fiber, the HHT nanofiber and the SWNT foams. The chopped fiber samples were not used in this instance. From the compression data the chopped fibers were seen to degrade the foam instead of improve it. Again, due to the expensive nature of the single wall nanotubes, they are used sparingly. As mentioned in Chapter VI Section 3.2, foams containing 5.0% by weight are being used except the sample containing the single wall nanotubes (SWNT). This sample contains only 1.0 % by weight and is linearly scaled up to that of the others via a trend in weight percentages.

For the stiffness measurements, the SWNT sample is comparable to that of the HHT sample even before scaling. Again as seen in the compression data, the HHT stiffness is slightly higher than the milled fiber foam. As displayed in figure 7-4a, all doped foams in the ligament study display properties higher than the standard pitch ligaments. Thus increasing size decreases tensile stiffness.

The tensile strengths of doped ligaments in figure 7-4b are many times higher than the control pitch ligaments. Strength is seen to increase more rapidly with decreasing size, very similar to that of the compression data. In this instance the SWNT appears to have a lower strength but again when scaled, it too follows the size dependent trend. This can be attributed to the increased zigzag structure apparent in figure 7-5 of SWNT foams.

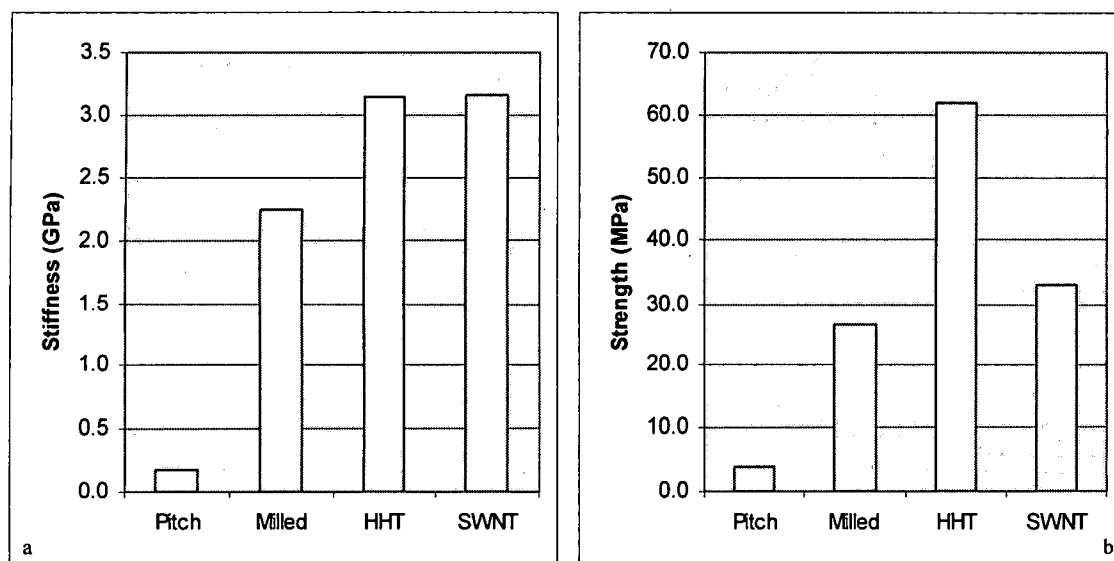


Figure 7-4 (a) Stiffness and (b) strength of ligaments with various size additives

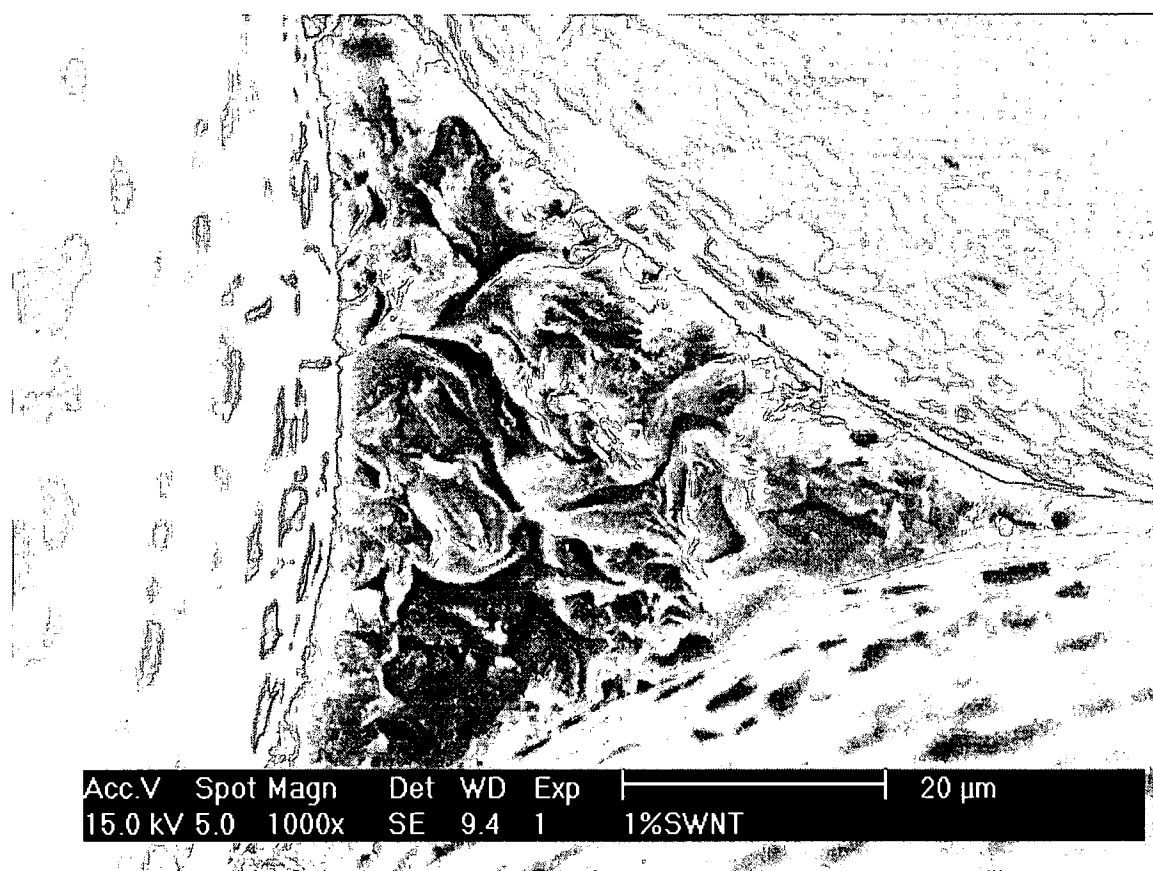


Figure 7-5 SEM picture of a SWNT foam

Note that the ligament data is based on the average of successful tests. Therefore, the top three values of each were displayed to see the consistency in high breaking ligaments. The milled and the standard pitch were found to have the most consistent results. From the data, it appears that the consistency decreases with decreasing size. This could be due to localized areas of particulates in the ligaments. The smaller additive material may not separate as easily, preventing even dispersion. The smaller additives in the pitch-additive solution pass through the shear mixer unscathed and do not fully break apart.

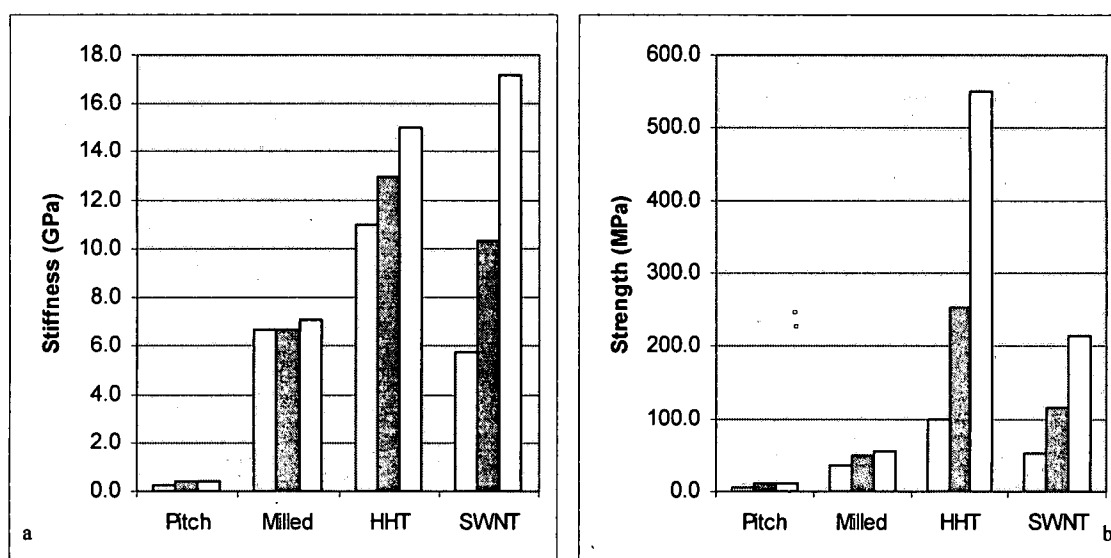


Figure 7-6 The maximum (a) stiffnesses and (b) strengths of ligaments with various size additives

3.0 Effect of Additive Shape on Foam Properties

The additives selected are all on relatively the same size scale. The shapes include; two spherical carbon black samples, Black Pearls (PRL) and Vulcan XC 72 (VUL), the cylindrical tube structure of the nanofiber HHT and the

flat plane structure of exfoliated graphite (EXG). Due to time constraints the EXG additive was not implemented in the bulk compression data.

3.1 Shape Effect on Bulk Compression Tests

The bulk compression tests reveal that spherical additives maintain a similar specific stiffness as pure pitch based foam while slightly increasing the strength. Again the HHT nanofibers, cylindrical in nature show an increase in specific stiffness and an increase the strength by double that of pure carbon foam. According to the bulk data, cylindrical additives are more beneficial than spherical ones.

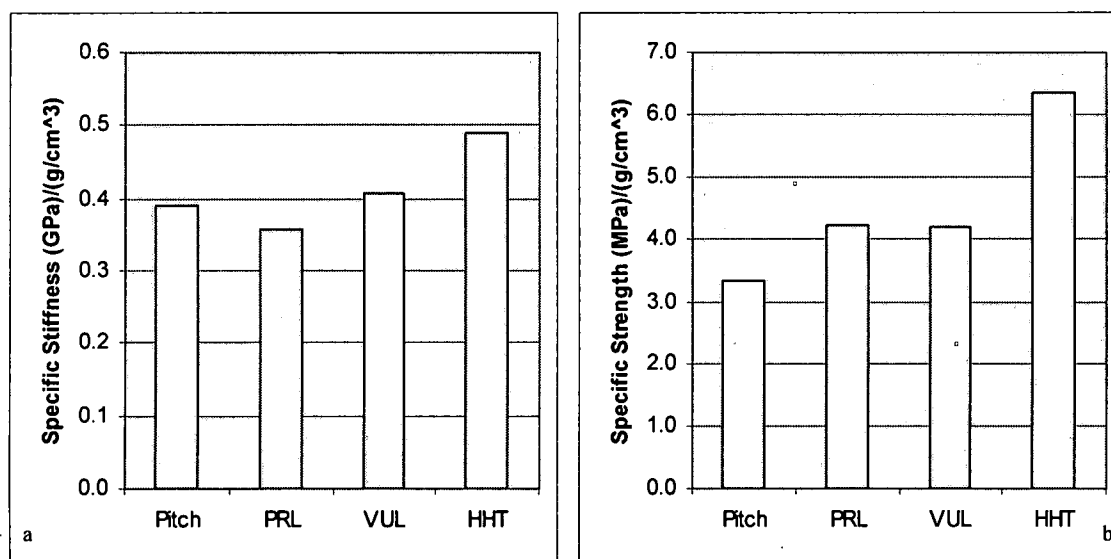


Figure 7-7 (a) Specific stiffness and (b) specific strength of foams with various shaped additives

3.2 Shape Effect on Ligament Tests

Inspecting ligament data gives similar trends in that the HHT fibers have higher stiffness than the carbon black sample and the carbon black samples are greater than the control pitch based foam. The thin sheet exfoliated graphite

sample was seen to perform the best, with a higher stiffness and strength than was even experienced by the HHT ligaments. It can then be expected that the bulk properties of this foam will too excel.

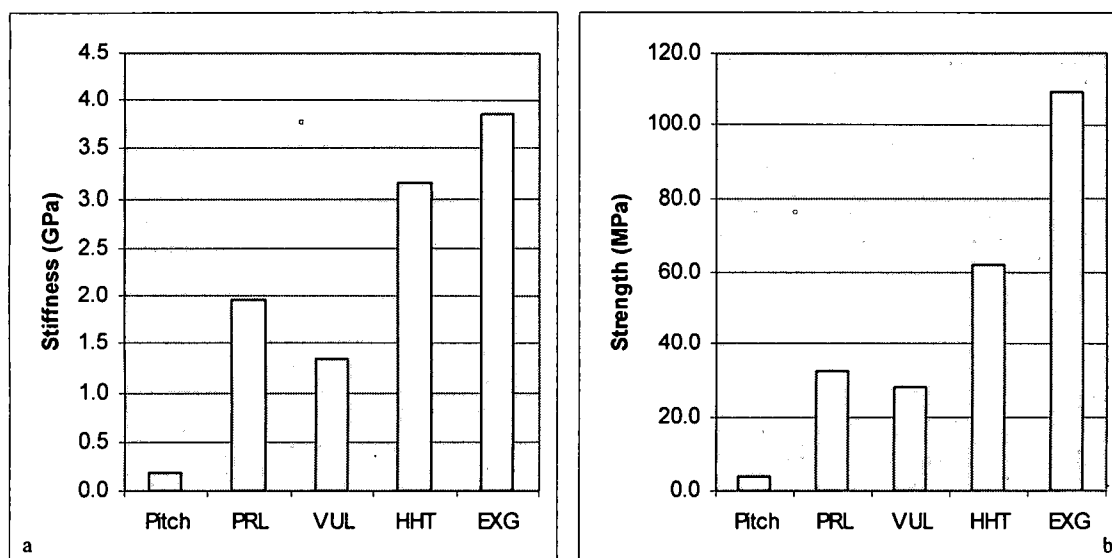


Figure 7-8 (a) Stiffness and (b) strength of ligaments with various shaped additives

The increase in foam properties can be linked to the surface energy that each particulate has as well as the lack of impurities. Increasing surface energy and decreasing the surface impurities will increase the additive and the pitch to join flawlessly, allowing applied stresses to be absorbed by both the pitch and the additive. When this occurs, the foam is then capable of exploiting the additives properties along with producing the desired zigzag structure. If adhesion does not occur, the additives act as stress risers, or flaws in the foam and lead to propagation areas for cracks which ultimately lead to foam failure. Exfoliated graphite with its thin sheets has extremely high surface area and surface energy. This is followed by HHT and the carbon black samples. The mechanical testing follows the same trends.

As before there is some inconsistency in the top 3 ligament data as can be seen in figure 7-9. This again may be due to localized particulate areas. Though the foam is at 5 % additive, the individual ligaments of the foam may vary from that value.

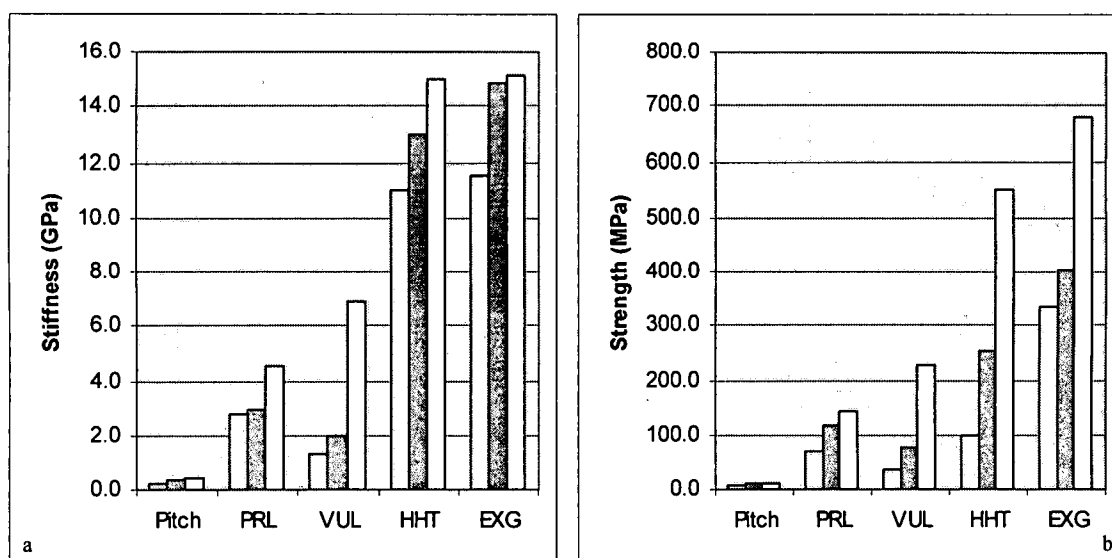


Figure 7-9 The maximum (a) stiffnesses and (b) strengths of ligaments with various shaped additives

4.0 The Effect of Silver Coated Nanofibers on Foam Properties

As mentioned previously, nanofibers were silver coated using a sputtering technique and placed in foam. The proposed idea involves implementing silver into foam to help in electrical conductivity while maintaining the foam's strength and stiffness. Figures 7-10 and 7-11 shows the bulk compression and tensile ligament data for pure pitch, HHT and silver coated nanofibers.

Silver coating the nanofibers ultimately lowers the foam properties relative to non-coated HHT fiber foams. This is seen in both ligament and bulk data. The silver coated nanofibers still remain specifically stronger than the pure pitch

based foam, but the bulk specific stiffness is seen to be slightly lower. When looking at the ligament data both the tensile strength and the stiffness, though lower than pure HHT, are improvements over the pure pitch ligaments.

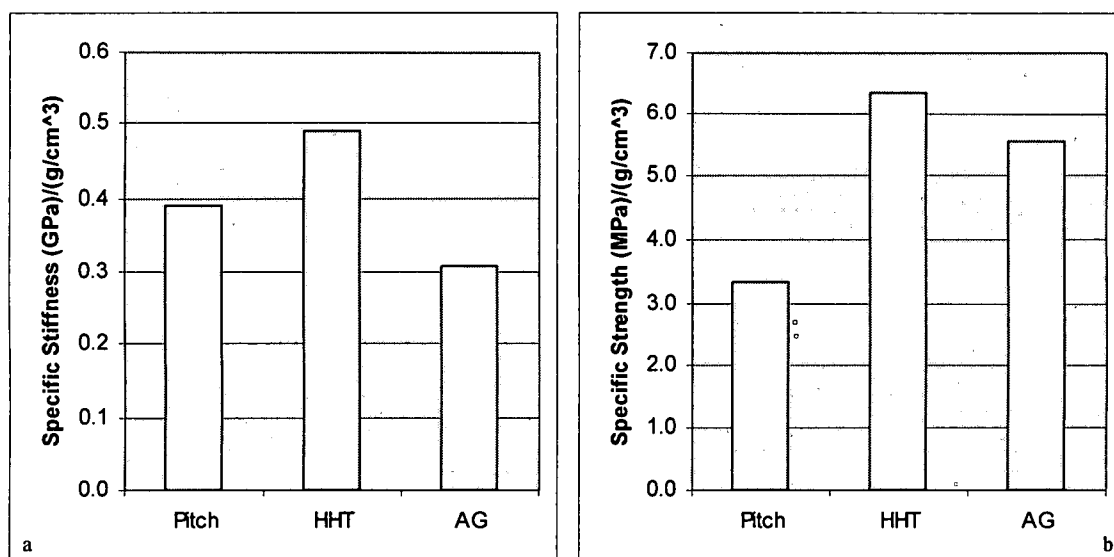


Figure 7-10 (a) Specific stiffness and (b) specific strength

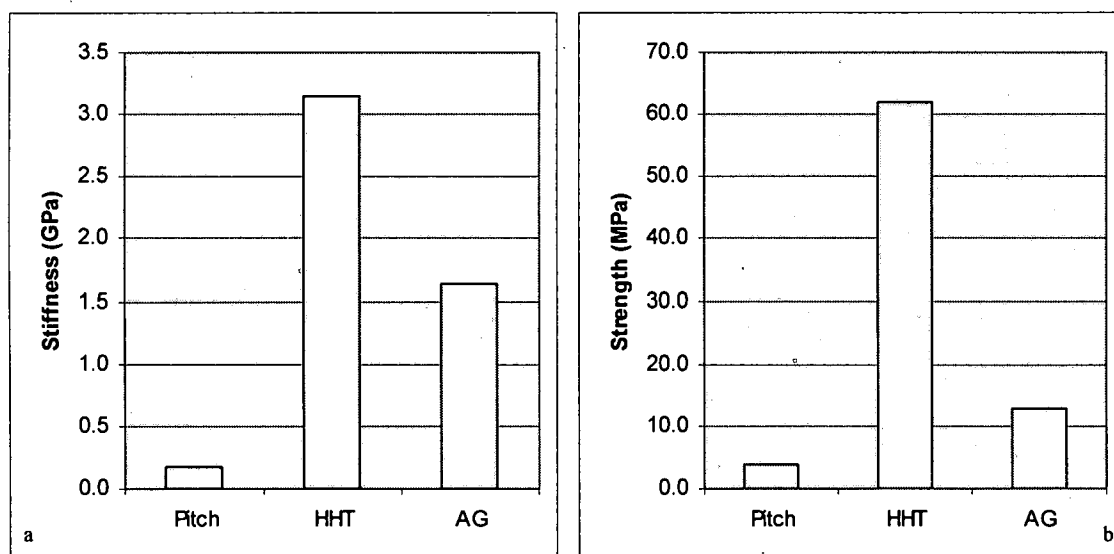


Figure 7-11 (a) Stiffness and (b) strength of ligaments

This decrease in properties relative to the HHT could be due to the increased size with silver application. Applying silver lowers the surface energy

and may hinder the bonding to the base pitch material. Nevertheless, the silver coated nanofiber foam is comparable to pure pitch based foam if not slightly better. With the slight increase in size it is also notable that the variability of high ligament values in the test results is also lowered as seen in the size dependent section, Section 2.0.

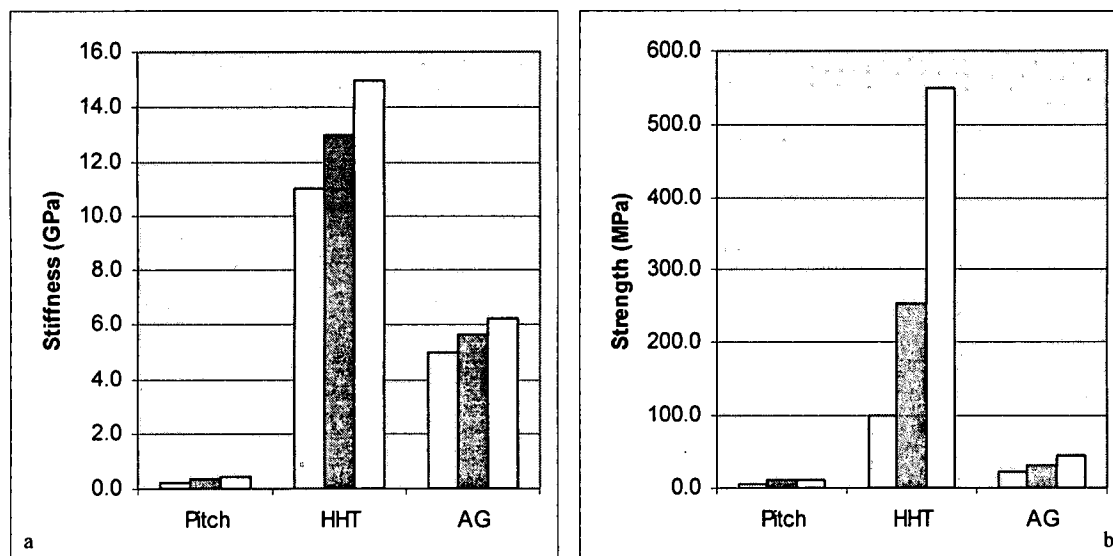


Figure 7-12 The maximum (a) stiffnesses and (b) strengths of ligaments with various additives

Foams were successfully created up to 20% loading of silver coated HHT. The specific strength stayed relatively constant increasing moderately while stiffness decreased. This shows some promise in its use for increasing electrical conductivity especially if the stiffness can be increased by another manner. However, until electrical conductivity measurements can be completed, the success of this material will not be known.

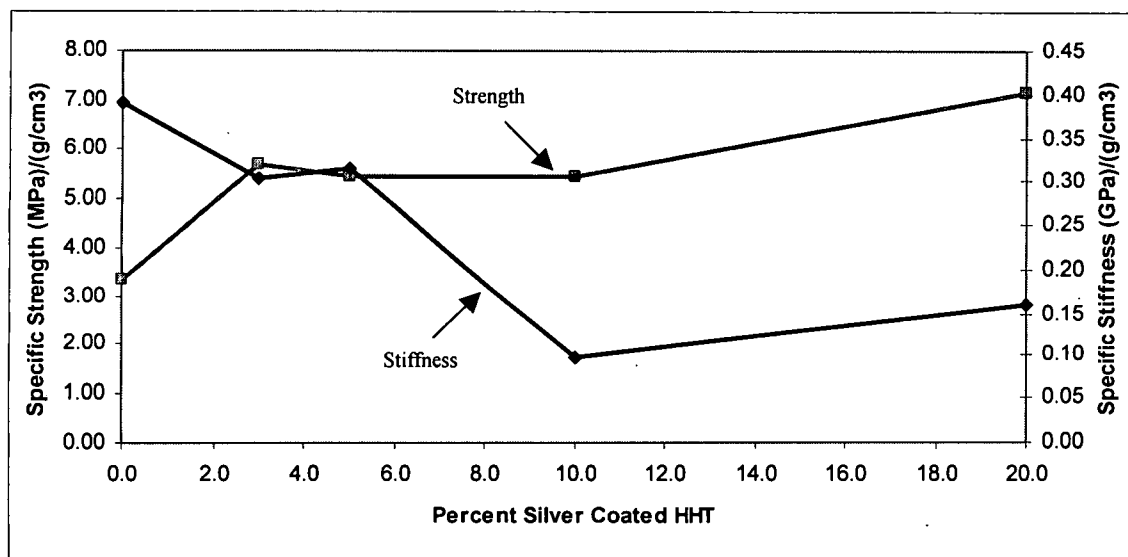


Figure 7-13 Specific stiffness and strength for silver coated HHT nanofibers

The bubble distribution of carbon foams containing silver coated nanofibers was also investigated to determine if it too had an effect on bulk properties. Figure 7-14 shows that increasing the percent additive increases the bubble size and distribution. The disjointed sections of the pie graph indicate the largest amount of a particular size bubble, and as the percent additive is increased, so is the disjointed section. Increased additive moves the mean bubble size from less than 100 microns to a range between 100 and 200 microns.

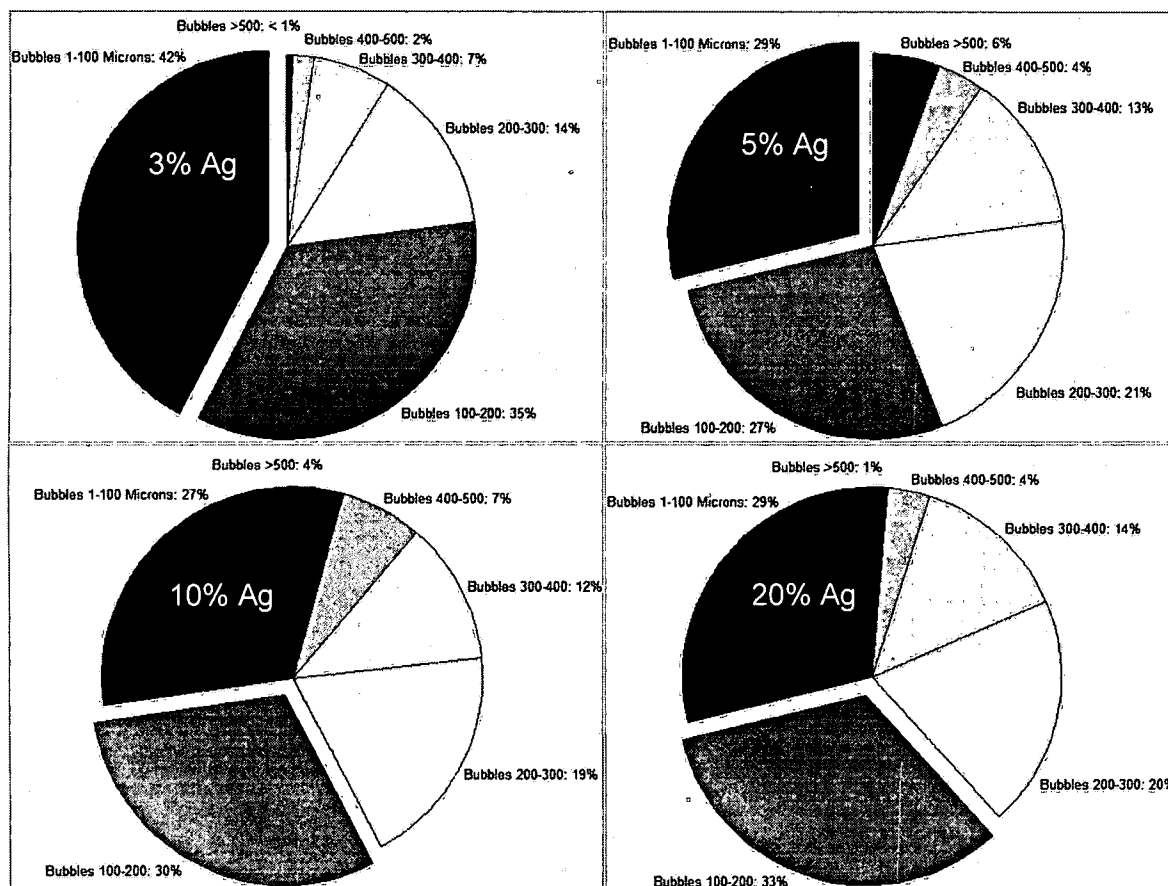


Figure 7-14 Bubble distribution in terms of size percents of various foams containing silver coated nanofibers

Increasing the percent additive is known to increase the zigzag structure as mentioned earlier. This is very clearly displayed in the micrographs in figure 7-15. Various loading percentages by weight are shown relative to pure mesophase pitch based carbon foam. The pure pitch carbon foam contains ligaments where individual crystalline structures encompass the entire ligament. For this case, failure along one grain boundary will ultimately lead to complete failure of that ligament. However, as the percentage increases, the crystalline structures, indicated by the various colors, continue to become smaller as does the individual grain boundaries. The silver coated nanofibers are seen to cap the

ends of these crystalline structures leading to a smaller and more homogeneous structure, figure 7-16. Even if failure occurs along one grain boundary, the entire structure does not and is still capable of sustaining the load demonstrating the benefit of the zigzag structure.



Figure 7-15 Carbon foam with (a) no additives, (b) 5% Silver nanofiber, (c) 10% silver nanofiber and (d) 20 % silver nanofiber



Figure 7-16 A magnified micrograph of a ligament containing silver coated nanofibers (single arrows on silver particles)

SEM images were also taken to view the effects of this additive. Figure 7-17 shows that the increased additive size did not produce cracking in the foam like the larger chopped fibers. However, the zigzag structure in the ligaments, seen in figure 7-18, is not as pronounced as with smaller fibers. Again, this leads to a lower performance compared to that of the HHT nanofiber foams.

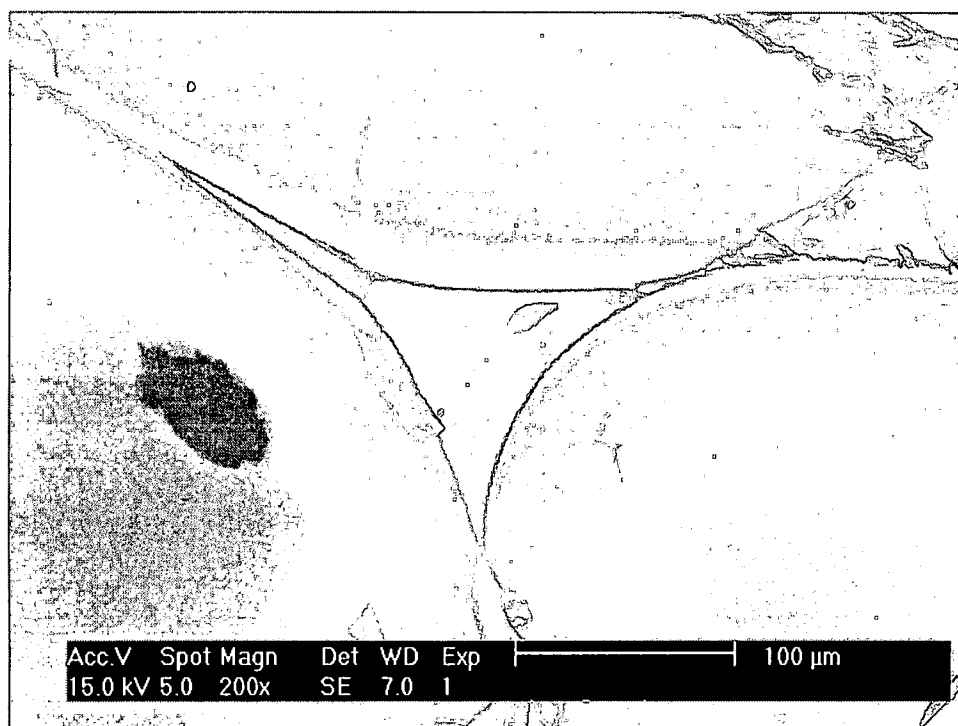


Figure 7-17 SEM image of silver coated nanofiber foam

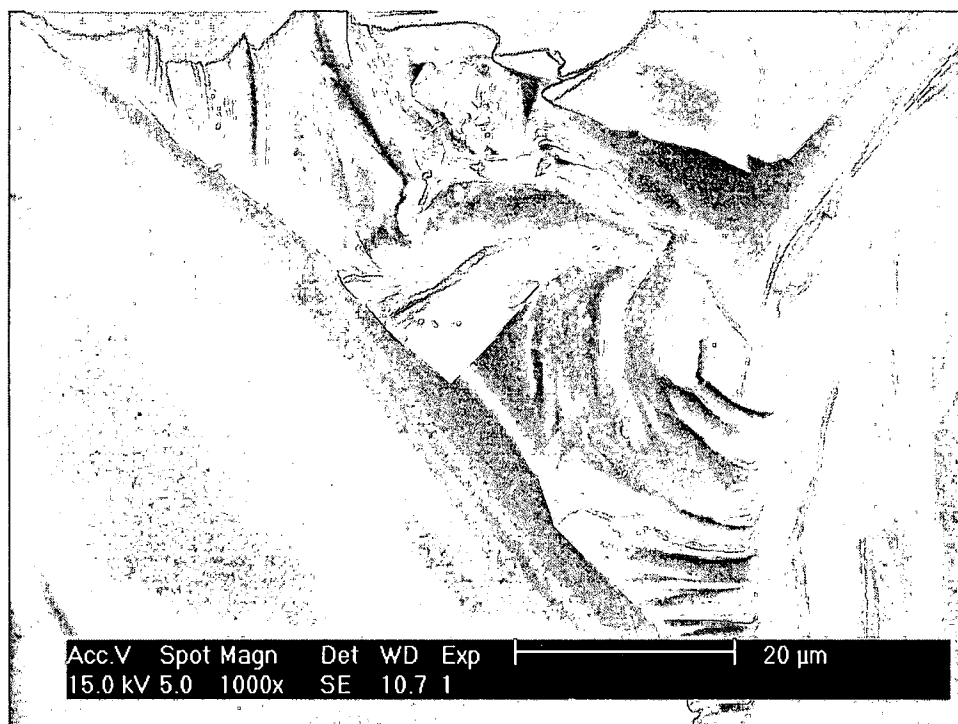


Figure 7-18 SEM image of a silver coated nanofiber foam displaying the zigzag structure

5.0 Effect of Additive Weight Percent in Foam

For the bulk compression tests, each fiber was added to the pitch precursor in a range of weight percentages. These include a 0.5, 1.0, 2.0, 3.0, 4.0, and 5.0 weight percent and with this adjustment the percent additive effect was also determined. This too seemed to have a dependence on size. Larger additives decrease specific strength and stiffness with increasing weight percentages. However, additives on the size order of HHT seem to increase the specific strengths and stiffnesses with percent additive as is seen in figure 7-19. This will reach a maximum loading value but more data is needed to achieve that value and to eliminate inconsistencies seen in individual compression tests.

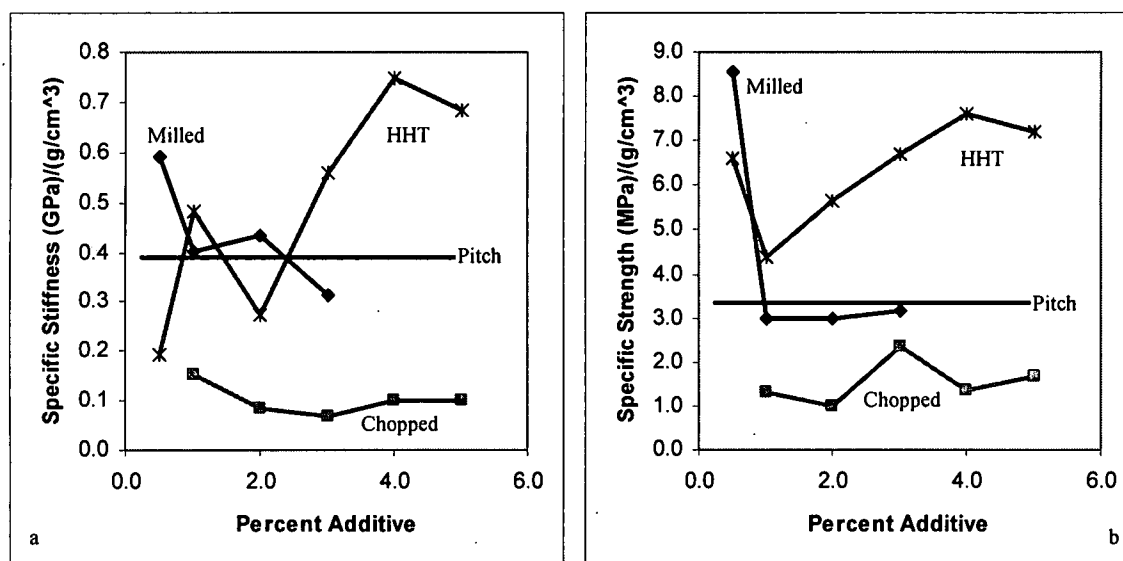


Figure 7-19 (a) Specific stiffness and (b) strength with weight percent additive

6.0 Additional Ligaments Analysis

There are a couple of findings that are notable during the testing of ligaments which include the ligament aspect ratio and the ligament failure mechanism. The aspect ratio is the ligament length divided by its diameter. On

average as the aspect ratio is increased so is the ligament performance, in both strength and stiffness. The variability is also seen to increase by the fanning out of the data. Though this has an effect on individual ligaments, the overall data and trends shown previously still hold true because of the large sampling and aspect ratio range experienced during testing. This is displayed in the following figures, figures 7-20 and 7-21.

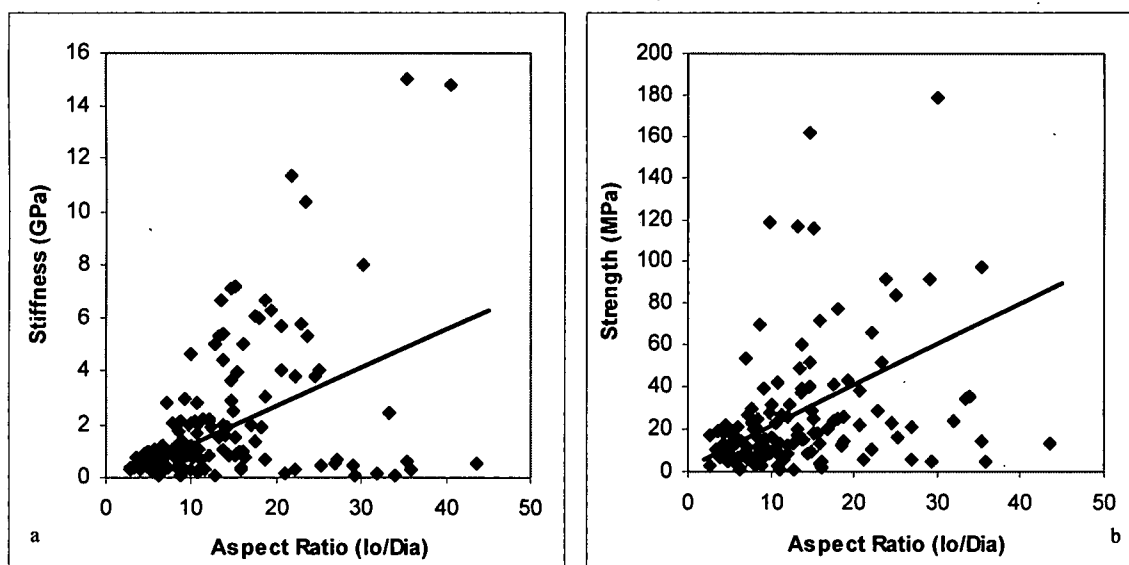


Figure 7-20 (a) Stiffness and (b) strength on ligaments relative to aspect ratio

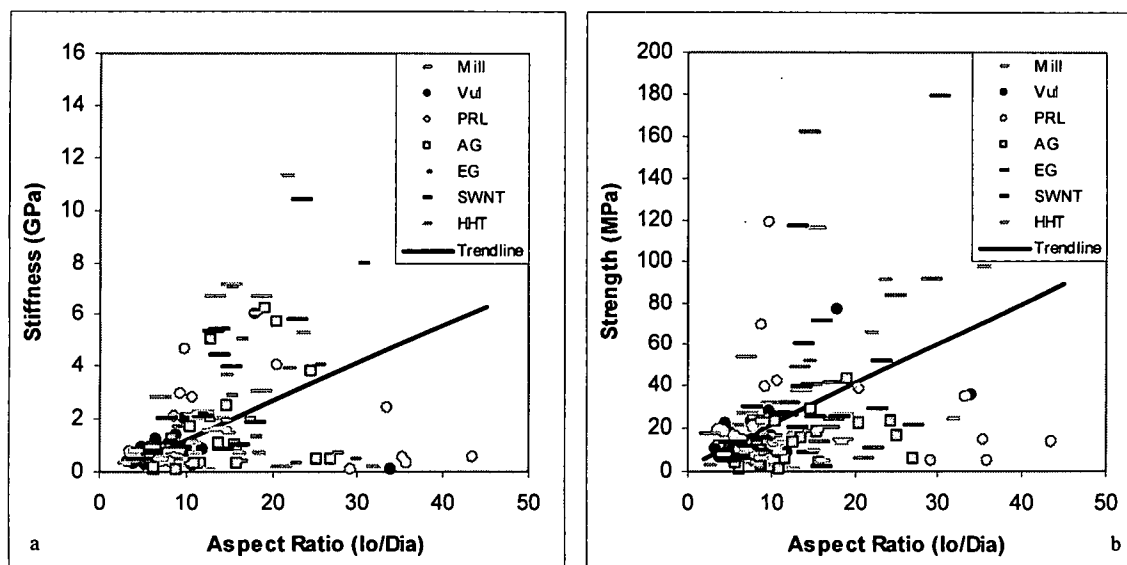


Figure 7-21 Figure 7-20 broken down into individual additive types

The second noticeable observance is the ligament failure mechanism. The ligaments fail as that of a thin film and not the pure carbon fiber as is often used in the numerical modeling of carbon foam structure. This is clearly seen in the videos of breaking pitch base foam ligaments. Snapshots of a video are shown in figure 7-22. The failure mechanism of carbon fibers is a purely brittle break. Upon its failure, carbon fibers are broken directly across and with an extreme force. However, in the ligament tests, the failure occurs across the basal planes and grain boundaries. Load can continually be applied until the failure works its way across the various basal planes. Nevertheless, using additives to increase the zigzag structure has mimicked carbon fibers slightly, as seen by the more brittle fracture in figure 7-23.

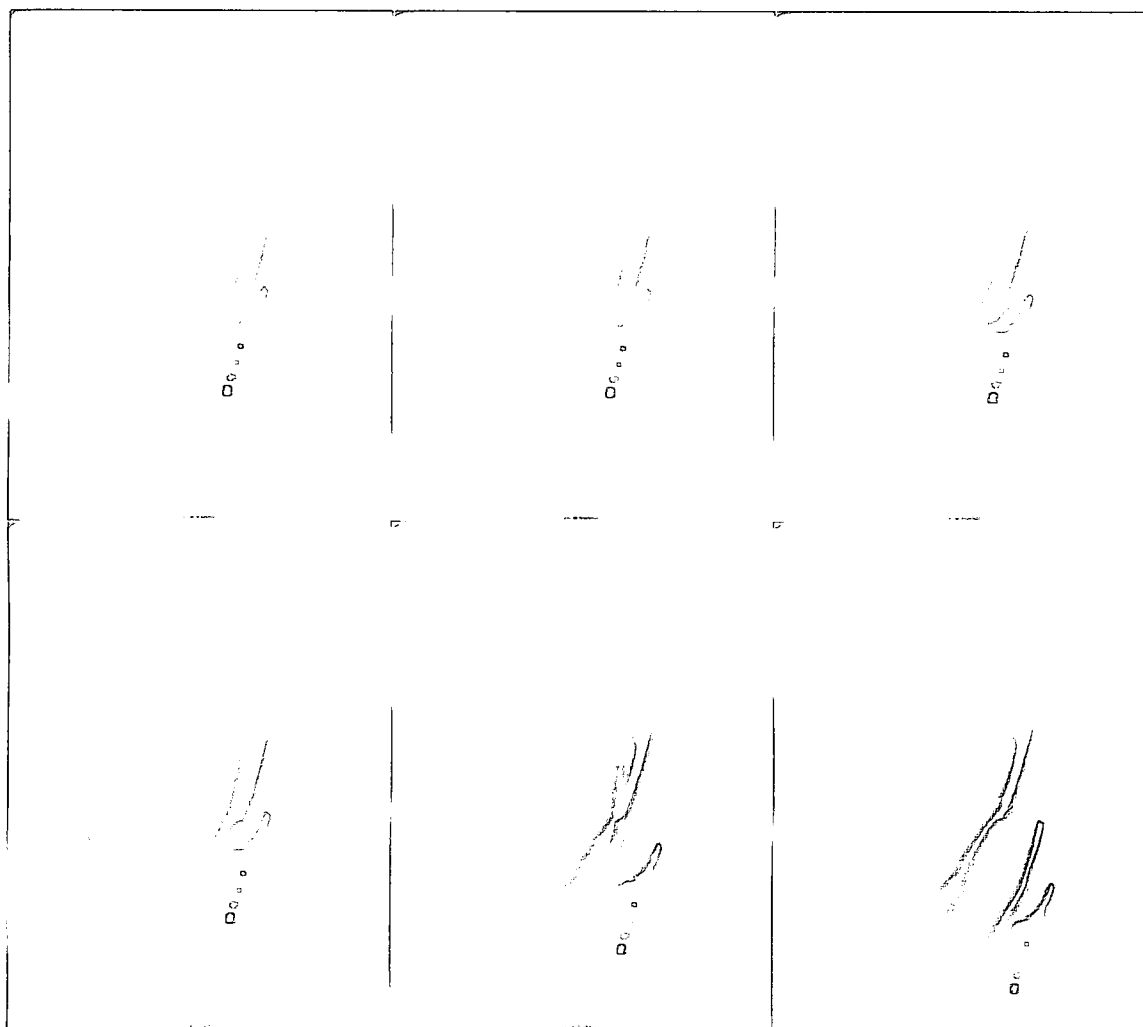


Figure 7-22 Sequential images of ligament failure

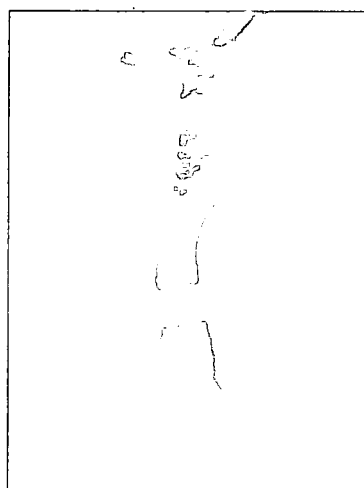


Figure 7-23 Image of a brittle ligament failure

7.0 Bubble Distribution of Doped Carbon Foam

In processing carbon foams, some variability occurred in final temperature and pressures. This coupled with additive effects produces a range of bubble distributions. The stitched micrographs described in Chapter VI Section 2.0, accompanied by image analysis software, allows for a range of calculations, including, bubble size and number. For normal types of distribution and number average or volume average may be sufficient but for foams like carbon foam where there is a wide range of bubble sizes and an abnormal distribution within one cross section it is suggested to use the dimensionless Skewness number, S_k . This number can incorporate both the number and volume averages as is shown in equation (1) and allows bubble size comparison to be performed between foams [133].

$$S_k = \frac{\left(\frac{1}{n} \sum_{i=1}^n (r_i - r_{avg})^3 \right)}{\left(\frac{1}{(n-1)} \sum_{i=1}^n (r_i - r_{avg})^2 \right)^{3/2}} \quad (1)$$

As found in previous studies, it too was confirmed that increasing temperature increases bubble size. As is seen in figure 7-24a, increasing temperature increases the Skewness number and with this the bubble distribution is shifted toward the larger bubble size. Higher temperatures relate to lower viscosities as well as increased time for bubble growth. The soften temperature of the material does not change but when the pressure is released at a higher temperature, more growth can occur before the viscosity reaches its solid state. When allowable growth time is increased, nucleation sites will not all

correspond to a single instant. Instead they may continue to initiate growth throughout the pressure release and cooling, in turn creating a wider range of bubble sizes.

Increasing the pressure is also seen to have a slight effect in the final growth and distribution of the bubble as is seen in figure 7-24b. As pressure is increased, so does the bubbles size as in seen by the higher Skewness number. At higher release pressures, the pressure difference inside versus the surroundings is larger. Consequently, the initial bubble pressure at the nucleation sites is elevated. Upon release the initial growth of the bubble is greater resulting in larger final bubble sizes. This effect is small compared to that of temperature. Though the trendlines appear to be the similar in slope, the temperature variance is less than 10°C whereas the pressure is over a range of nearly 150 psi.

Increasing the percent additive appeared to have very little or no effect relative to the bubble distribution in these foams. The additives should increase the melt viscosity, resulting in smaller bubbles and bubble distribution. In this case, the viscosity change must be minuscule with the low percentage of additives or the bubble data is similar as a resultant of localized areas of non-uniformity commonly found in carbon foam.

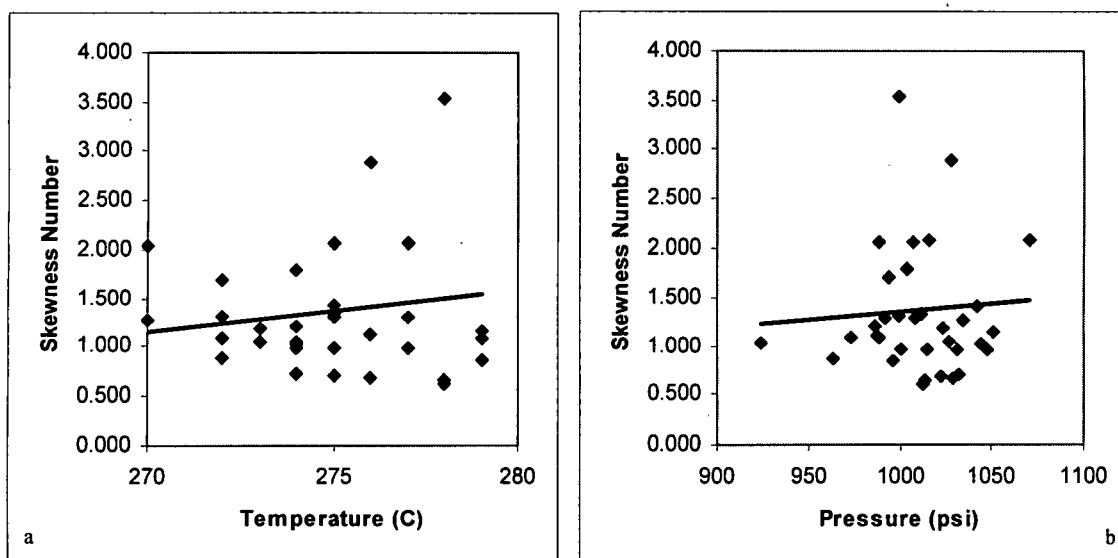


Figure 7-24 Skewness number with (a) temperature and (b) pressure

From the bulk bubble distribution data, the temperature effects are the dominate source of variance in bubble size and distribution because of its effect on viscosity. This is followed by pressure effects. If these two effects can be rigidly controlled the resulting foams should maintain a consistent foam structure. To produce smaller uniform bubbles in carbon foam processing, the final temperature and pressure during foaming should be held toward the lower value.

Chapter VIII

Conclusions

Various areas of carbon foam have been explored in this study, all being interconnected. The performance of carbon foam is not only related to the microstructure but also the matrix material and that material's molecular orientation. Therefore factors which alter any of these entities, factors such as bubble size, bubble size distribution, and additives to the pitch matrix, will have a distinct effect on carbon foam performance. Improvements in the building blocks of carbon foam, the material itself and the microstructure, will lead to improvements in the total foam's performance.

First, the microstructure was examined. It is inherent that non-uniformity of bubble size and distribution produced localized stresses, ultimately leading to localized failure which propagates across the foam reducing its performance. If both bubble size and distribution are uniform throughout the foam, the applied load will be distributed more efficiently through the ligaments and nodes. Consequently, controlling bubble growth is one key to improving performance. This was studied in the numerical model through varying initial bubble size, initial pressure and changes in viscosity. From the numerical level set model, it was also verified that the bubble experiences a slight movement simultaneously with the growth leading to more alignment in the microstructure. However, the

movement is relatively negligible compared to the bubble growth. It was found that an increase of initial bubble radius causes an increase in both the bubble growth rate and movement. Increasing the foaming temperature also increases the bubble growth and the variability in bubble size by decreasing the melt viscosity. Furthermore, lowering the initial bubble pressure slows the growth and in turn reduces the bubble movement. Ultimately, it was the foaming temperature and not pressure that had the largest effect on bubble growth and microstructure. Consequently, the temperature needs to be rigidly controlled during processing to ensure predictable results.

Once the microstructure is controlled, the material itself, in the form of ligaments, must be optimized. To achieve this, the ligaments are tailored to increase performance based both on mechanical and molecular alterations. During processing, the ligaments' performance improves with increasing aspect ratio. This is due to the increased alignment from higher strain rates. Therefore, increasing the number of bubbles in the foam as well as their size causes the ligament to become thinner and longer with better molecular orientation resulting in higher material properties.

Another way of enhancing the material itself is through enrichment of the zigzag structure of the graphene planes in the ligaments. This is accomplished by using specialized fractions of pitch, such as the beta fraction, or through the use of additives mixed in with the base mesophase pitch material prior to processing. The beta fraction inherently produces this desired zigzag structure whereas additives interact with the host material directly affecting the molecular

structure of the ligament. This effect was seen to be cumulative as increased additives directly related to a higher presence of the zigzag structure leading to improved mechanical properties.

Additives are available in a variety of shapes and sizes and directly affect the strength and stiffness of the doped ligament and in turn the carbon foam. All additives in this study affect the crystalline structure differently but generalizations can be constructed. For example, decreasing the particulate size causes an increase in both strength and stiffness through a higher concentration of zigzag structure. If the particulate is too large, as is seen with chopped fibers, it can actually reduce the properties to below that of standard pitch based foams. This reduction occurs due to the inadequate interfacial bonding and the natural stress concentrations occurring as a result of the dopant's size. Therefore, smaller additives directly result in higher foam properties as seen with the exceptional performance of SWNT doped foams.

In the additive shape analysis, it was also found that increasing the surface energy and decreasing surface impurities of the additive is beneficial to strength and stiffness. The flat structure of exfoliated graphite produced the most beneficial properties in terms of shape due to its high surface area with few surface impurities. Therefore chemical alterations of the host material occur readily, providing complete adhesion between the additive and the precursor.

Throughout these studies, it was found that processing had a distinct effect on carbon foam's final performance. This effect on performance was due both to alterations which occur to the microstructure as well as the material itself.

Therefore present and future studies of carbon foam should seek to simultaneously improve both the microstructure and the foam matrix material.

Bibliography

- [1] Donnet JB. Carbon Fibers, New York: Dekker, 1998.
- [2] Googin J, Napier J. US Patent 3345440. 1967.
- [3] Schmitt CR, Coffey AL, Schreyer JM. Atomic Energy Commission RD report. Union Carbide Corp. 1969.
- [4] Knippenberg WF, Lersmacher B. Phillips Tech. Review 1976; 36: 93-103.
- [5] Sands AE, Scrivner ME, Paluzelle R. Atomic energy commission RD
- [6] Lever WE, Gerwels JM, Holland CW. Atomic energy commission RD report. Union Carbide Corp. 1969.
- [7] Klett J, Hardy R, Romine E, Walls C, Burchell T. Carbon 2000; 38: 953-973.
- [8] Sandhu SS, Hager JW. Mat. Res. Soc. Sym. 1992; 270: 35-40. report. Union Carbide Corp. 1970.
- [9] Krock RP, Boyer C, Kiser MD. 32nd SAMPE Symposium 1987; 32: 1447-1460.
- [10] Hager JW, Lake ML. Mat. Res. Soc. Sym. 1992; 270: 29-33.
- [11] Hager JW. Mat. Res. Soc. Sym. 1992; 270: 41-46.
- [12] Rogers D, Plucinski J, Stansberry P, Stiller A, Zondlo J. Proceedings, International SAMPE Symposium and Exhibition. Society of Materials and Process Engineers. , 2000; 45 (I): 293-305
- [13] Touchstone Research Laboratory. Cfoam Homepage. www.cfoam.com. 2003.
- [14] Hager JW, Anderson DP. 21st Biennial Conference on Carbon, Buffalo NY USA; 1993: 102-103.
- [15] Klett JW, Mcmillan AD, Gallego NC, Walls CA. Journal of Materials Science 2004; 39: 3659-3676.
- [16] Stiller AH, Stansberry PG, Zondlo JW. US Patent 5,888,469. 1999.
- [17] Stiller AH, Stansberry PG, Zondlo JW. US Patent 6,346,226. 2002.
- [18] Stiller AH, Yocum A, Plucinski J. US Patent 6,183,854. 2001.
- [19] Stiller AH, Stansberry PG, Zondlo JW. US Patent 6,241,957. 2001.
- [20] Spralding DM, Guth RA. Adv. Mat. & Proc. 2003: 29-31.
- [21] Klett JW, Walls C, Burchell T. Int'l Conf. on Carbon 1999. Charleston SC USA: 132.
- [22] Gallego NC, Klett JW, Mcmillan AD. Intl. Conf. on Carbon Beijing, China; 2002.
- [23] Klett JW. J. of Comp. in Man. 1998; 15: 1-7.
- [24] Anderson DP, Wapner PG, Curliss DB. Mat. Res. Soc. Sym. 1992; 270: 59-64.

- [25] Mehta R, Anderson DP, Hager JW, Thorp K. 21st Biennial Conf. on Carbon. Buffalo, NY; 1993: 102-103.
- [26] Dutta D, Hill CS. Cellular and microcellular materials. ASME 1994; 53: 63-70.
- [27] Kearns KM, Anderson DP, Anderson HJ. Mat. Res. Soc. Symp. 1998; 521: 185-190.
- [28] Kearns KM. US Patent 5,868,974. 1999.
- [29] Klett, JW. US Patent 6,344,159. 2002.
- [30] Mehta R, Anderson DP, Hager JW. Carbon 2003; 41: 2159-2179.
- [31] Gallego NC, Armstrong B, Mcmillan AD, Klett JW. Oak Ridge National Labs 2003 Progress Report. 23-28.
- [32] Klett JW. US Patent 6,033,506. 2000.
- [33] MER Corporation. Product literature, 2004.
- [34] Withers JC, Patel JP. International SAMPE Symposium and Exhibition 2000; 45: 659-663.
- [35] Hall R, Hager JW. 21st Biennial Conference on Carbon. Buffalo, NY; 1993: 100-101.
- [36] Hall RB, Hager JW. Mat. Res. Soc. Symp. 1994; 349: 67-71.
- [37] Anderson DP, Kearns KM, Klett JW, Roy AK. Aerospace Conference Proceedings IEEE, Big Sky MT USA 2000; 4: 193-200.
- [38] Dutta D, Hill CS, Anderson DP. Mat. Res. Soc. Symp. 1994; 349: 61-66.
- [39] Kearns KM. US Patent 5,961,814. 1999.
- [40] Klett JW, McMillan AD, Gallego NC, Burchell TD, Walls CA. Carbon 2004; 42: 1849-1852.
- [41] Christensen RM. Mech. Phys. Solids 1986; 34: 563-578.
- [42] Warren WE, Kraynik AM. J. of App. Mech. 1988; 55: 341-345.
- [43] Gibson LJ, Ashby MF. Cellular Solids: Structure and Properties, 2nd Edition. Cambridge University Press. UK.
- [44] Anderson DP, Gunnison KE, Hager JW. Mat. Res. Soc. Sym. 1992; 270: 37-52.
- [45] Sihn S, Roy AK. J. of Mech. And Phy. Of Solids 2004; 52: 167-191.
- [46] Kweeder JA, Ramesh NS, Campbell GA, Rasmussen DH. ANTEC 1991; 1398-1400.
- [47] Colton JS, Suh NP. Polymer Engineering and Science 1987; 27: 485-492.
- [48] Colton JS, Suh NP. Polymer Engineering and Science 1987; 27: 500-503.
- [49] Plesset MS, Zwick SA. Journal of Applied Physics 1954; 29: 493-500.
- [50] Rayleigh. Philosophical Magazine 1917; 34: 94-98.
- [51] Scriven LE. Chemical Engineering Science. 1959; 10: 1-13.
- [52] Barlow EJ, Langlois WE. IBM Research Journal 1962; 6: 329-337.
- [53] Rosner DE, Epstein M. Chemical Engineering Science 1972; 27: 69-87.
- [54] Han CD, Yoo HJ. A.I.Ch.E Journal 1982; 28: 1002-1009.
- [55] Upadhyay RK. Advances in Polymer Technology 1985; 5: 55-64.
- [56] Street J, Fricke A, Reiss L. Ind. Eng. Chem.. Fundam. 1971; 10: 54-64.
- [57] Arefmanesh A, Advani S, Michaelides E. Inter. J. Ht. and Ms. Trans. 1992; 35: 1711-1722.

- [58] Amon M, Denson C. Polymer Engineering and Science 1984; 24:1026-1034.
- [59] Venerus D. Polymer Engineering and Science 2001; 41: 1390-1398.
- [60] Ye T. Shyy W, Chung J. J. Comp. Physics 2001; 174: 781-815.
- [61] Beechem T, Elgafy A, Lafdi K. Carbon 2005; In Press .
- [62] Lo WL. Journal of Cellular Plastics 1965; January: 45-50.
- [63] Warren WE, Kraynik AM. J. of App. Mech. 1997; 64: 787-794.
- [64] Gaies D, Faber KT. Carbon 2002; 40: 1131-1150.
- [65] Morgan DR. Dallas TX USA, University of North Texas, Masters Thesis, 2001.
- [66] Oak Ridge National Labs. Carbon Foam Page. <http://www.ms.ornl.gov/researchgroups/CMT/FOAM/foams.htm>. 2004.
- [67] Klett J, Jones S, Klett L, Walls C. SAMPE Sym. Long Beach California USA, 2003.
- [68] Klett J, Klett L, Strizak J, Williams M, Mcmillan A, Valencia J, Creeden T. 24th Annual Conference on Ceramic, Metal, and Carbon Composites, Materials and Structures. Cocoa Beach FL USA, January 2000.
- [69] Klett JW, US Patent 6,398,994. 2002.
- [70] Klett J, Lowden R, McMillan A. Proceedings of the 2nd World Conference on Carbon, Lexington KY USA, 2001.
- [71] Klett JW, Klett L, Burchell T, Walls C. SAE 2000.
- [72] Pocofoam. Product literature, 2004.
- [73] Sanchez-Coronado J, Chung DDL. Carbon 2003; 41: 1175-1180.
- [74] Klett JW, Burchell TD. Eurocarbon 98: Science and Technology of Carbon, Published French Carbon Group, Strasbourg, France, July 5-9, 1998.
- [75] Gallego NC, Klett JW. Carbon 2003; 41: 1441-1446.
- [76] Garman RW, Elwell RJ. PCIM Conference, Chicago IL USA. 2001.
- [77] Klett J, Mcmillan A, Ott R. Proc. Of Automotive Engineering Government/Industry Meeting, Washington DC, June 19-21, 2000.
- [78] Bunning TJ, Jeon HG, Roy AK, Kearns KM, Farmer BL, et. al. Journal of Applied Polymer Science 2003; 87: 2348-2355.
- [79] Morgan DR, Biggers SB, Grujicic M. Engineering, Construction, and Operations in Challenging Environments. ASCE. Houston TX USA; 2004: 960-967.
- [80] Wright Materials Research Company. Product Data Sheet. 2004.
- [81] Kearns K. Air Force Research Lab Technical Brief; ML-00-13. 2000.
- [82] Klett J, Conway, B. International SAMPE Symposium and Exhibition 2000; 45 1933-1.
- [83] Klett, JW. Proceedings of the 43rd International SAMPE Symposium, May 31-June 4, Anaheim, California, SAMPE, 1998.
- [84] Klett JW, Mcmillan A, Ott R. Society of Automotive Engineering Government/Industry Meeting. Washington DC USA 2000.
- [85] Coursey JS, Kim J, Roh H, Boudreaux PJ. IMECE 2002. New Orleans LA USA. 2002.

- [86] Klett JW, Tee C, Stinton DP, Yu NA. Proceedings of the 1st World Conf. on Carbon, Berlin Germany 2000: 244.
- [87] Klett L, Klett JW. Proceedings of the 24th Bienial Conference on Carbon, July 11-16, Charleston, SC, 1999: 310.
- [88] Gou Z, Wu KH, Klett J. 6th International Conf. on Composites Engineering. Orlando FL USA, July 1998.
- [89] Electronic Design. April 3, 2000. 36.
- [90] Klett JW, Gallego N, Burchell T, Bailey J. Proceedings of the 2nd World Conf. on Carbon, Lexington KY USA, 2001.
- [91] Yang J, Shen Z, Hao Z. Carbon 2004; 42: 1882-1885.
- [92] Klett JW. US Patent 6,261,485, 2002.
- [93] Klett JW. US Patent 6,387,343, 2002.
- [94] Klett JW. US Patent 6,287,375. 2001.
- [95] Weaire D, Coughlan S, Fortes AM. Journal of Materials Processing Tech. 1995; 55: 178-185.
- [96] Klett JW, Burchell TD. US Patent 6,037,032. 2000.
- [97] Hall RB and Hager JW. J. Composite Materials 1996; 30(17): 1922-1937.
- [98] Wapner PG and Hager JW. 20th biennial conf. on carbon. Santa Barbara-USA, 1991; 188-195.
- [99] Shafi M and Flumerfelt R. Chemical Engineering Science 1997; 52(4): 627-633.
- [100] Patel RD. Chemical Engineering Science 1980; 35: 2352-2356.
- [101] Welch SWJ. Intern. Journal of Heat and Mass Transfer 1998; 41(12): 1655-1666.
- [102] Liger-Belair G, Vignes-Adler M, Voisin C, Robillard B and Jeandet P. Langmuir 2002; 18(4): 1294-1301.
- [103] Snabre P and Magnifotcham F. Eur. Phys. J. B 1998; 4(3): 369-377.
- [104] Sussman M, Smereka P and Osher S. Journal of Computational Physics 1994; 114: 146-159.
- [105] Sussman M, Fatemi E, Smereka P and Osher S. Computational Fluids 1999; 27: 663-680.
- [106] Son, G. Numerical Heat Transfer 2001; 39: 509-523.
- [107] Patankar SV. Numerical Heat Transfer and Fluid Flow. Hemisphere Washington DC: Taylor & Francis, 1980: 44-47, 68-111.
- [108] Shafi MA, Joshi K and Flumerfelt RW. Chemical Engineering Science 1997; 52(4): 635-644.
- [109] Joshi K, Lee JG, Shafi MA and Flumerfelt RW. J. Applied Polymer Science 1998; 67: 1353-1368.
- [110] Hara SK, Schowalter WR. J. of Non-Newtonian Fluid Mech. 1984; 14: 249-256.
- [111] Sangwok Sih, Personal Communication. 2005
- [112] Oberlin A, Rouzaud JN, and Goma J. Journal de Chimie Physique 1984; 81: 701-710.
- [113] White JL. Petroleum-Derived Carbons, ACS Symposium No. 21, Washington D.C., 1976; 282.
- [114] Zimmer JE, White JL. Advances in Liquid Crystals 1982; 5: 157.

- [115] Zimmer JE, White JL. Carbon 21, 323 (1983).
- [116] Lafdi K, Bonnamy S, Oberlin A. Carbon 1992; 30: 533.
- [117] Lafdi K, Bonnamy S, Oberlin A. Carbon 1994; 32: 11.
- [118] Fitzgerald DD, Taylor GH, Peennock GM. Carbon 1994; 32: 1389.
- [119] Strong, A. Brent, Society of Manufacturing Engineers, Michigan 1989.
- [120] Shi Z, Lian Y, Liao F, Zhou X, Gu Z, Zhang Y, Iijima S, Li H, Yue KT, Zhang S. Journal of Physics and Chemistry of Solids 2000; 61: 1031-36.
- [121] Zhang Y, Iijima S. Applied Physics Letters 1999; 75 (20): 3087-89.
- [122] Rinzler AG, Liu J, Dai H, Nikolaev P, Huffman CB, Rodríguez-Macías FJ, Boul PJ, Lu AH, Heymann D, Colbert DT, Lee RS, Fischer JE, Rao AM, Eklund PC, Smalley RE. Applied Physics A 1998; 67: 29-37.
- [123] Guo, T, Nikolaev P, Thess A, Colbert DT, R. E. Smalley RE. Chemical Physics Letters 1995; 243: 49-54.
- [124] Toebes ML, Bitter JH, Van Dillen AJ, De Jong KP. Catalysis Today 2002; 76: 33-42.
- [125] Hafner J, Bronikowski M, Azamian B, Nikolaev P, Rinzler AG, Colbert DT, K. Smith K, Smalley RE. Chemical Physics Letters 1998; 296: 195-202.
- [126] Shyu Y-M, Chau-Nan Hong F. Diamond and Related Materials 2001; 10: 1241-45.
- [127] Nikolaev P, Bronikowski MJ, Bradley RK, Rohmund F, Colbert DT, Smith KA, Smalley RE. Chemical Physics Letters 1999; 313: 91-97.
- [128] Bower C, Zhou O, Zhu W, Werder DJ, Jin S. Applied Physics Letters 2000; 77 (17): 2767-69.
- [129] Huang ZP, Xu JW, Ren ZF, Wang JH, Siegal MP, Provencio PN. Applied Physics Letters 1998; 73 (26): 3845-47.
- [130] Cui H, Zhou O, B. Stoner B. Journal of Applied Physics 2000; 88 (10): 6072-74.
- [131] Okai M, Muneyoshi T, Yaguchi T, Sasaki S. Applied Physics Letters 2000; 77 (21): 3468-70.
- [132] Pyrograf-III. Product Literature. Applied Sciences Incorporated. 2001.
- [133] Engelsens CW, Isarin JC, Gooijer H, Warmoeskerken MMCG, Wassink JG. Autex Research Journal 2002; 2: 14-27.

R002592053